Mathematical Models of Alzheimer's Disease

Dissertation

zur

Erlangung des akademischen Grades

Doktor-Ingenieur (Dr.-Ing.)

Promotionsgebiet Systembiologie

Fakultät für Informatik und Elektrotechnik

Universität Rostock

Universität Rostock Traditio et Innovatio

vorgelegt von

Felix Winter

Rostock, 31.05.2017

urn:nbn:de:gbv:28-diss2017-0147-9

Erstgutachter:	Prof. Olaf Wolkenhauer	Universität Rostock
Gutachter:	Dr Catrin Bludszuweit-Philipp	ASD Advanced Simulation and Design GmbH Rostock
	Prof. Lars Kaderali	Ernst-Moritz-Arndt-Universität Greifswald
Tag der Verteidigung: 20. Oktober 2017		

Und wenn ich prophetisch reden könnte und alle Geheimnisse wüsste und alle Erkenntnis hätte; wenn ich alle Glaubenskraft besäße und Berge damit versetzen könnte, hätte aber die Liebe nicht, wäre ich nichts.

1.Korinther 13:2

Errata

The following changes have been applied to the document with respect to the original submission.

Page	original	corrected
xvii	6-phosphate dehydrogenase	glucose-6-phosphate dehydrogenase
2	estimated in a study be	estimated in a study by
3	blood-oxygen dependent	blood-oxygen-level dependent
3	more background the	more background on the
12	to aggregate the	to aggregate, the
15	ABCA2	ABCA1
17	Aβ	APP
17	The data, [...] shows	The data, [...] show
19	ABC-Transporter	ABC transporter
22	if we apply and additive model	if we apply an additive model
34	pressure, detailed information	pressure, and detailed information
35	in the following denoted	is in the following denoted
40	The high-level description	The high-level descriptions
42	s	s^*
48	Still, these small differences	These small differences
50	of the aggregation mechanism	of the transport mechanism
50	is really a result the	is really a result of the
75	to a control group was reported 1996.	to a control group.
79	and describe stable steady sates	and describes stable steady state
90	the established model	the established models
93	array of dynamics	array of dynamics,
94	for each equations	for each equation
94	all reactions is depicted	all reactions depicted
105	$S(x) = \frac{\partial f(x)}{\partial x} \frac{(f(x+\Delta x)-f(x))}{\Delta x} \cdot \frac{x}{f(x)}$	$S(x) = \frac{\partial f(x)}{\partial x} \approx \frac{(f(x+\Delta x)-f(x))}{\Delta x} \cdot \frac{x}{f(x)}$
118	he reported changes	The reported changes

Abstract

Alzheimer's disease is a major neurodegenerative disease that affects more than 40 million people worldwide. Despite being in the focus of research for more than one hundred years, the aetiology for the majority of Alzheimer's cases remains unknown. In this work I describe the development, analysis and application of two mathematical models to improve the understanding of different aspects of the disease.

The first model deals with the process of production, aggregation, and removal of Aβ from the brain. Aβ is at the heart of the *amyloid hypothesis* which postulates that an imbalance between its production and removal is the key to understand Alzheimer's disease. To examine the role the two transport proteins ABCC1 and ABCB1 play in the removal of Aβ from the brain, I have constructed a phenomenological model that captures the dynamics of its aggregation *in vivo* in mice. The model assumes protein aggregation by initial nucleation and subsequent monomer addition, removal of monomeric Aβ by ABC transporters and a negative influence of larger aggregates on this removal. Using these assumptions I am able to show that the difference in the time course of Aβ aggregation dynamics can be explained by the different transport capacity of the transporter alone. This result is an important step forward regarding the development of interventions that keep the production and degradation of Aβ in balance.

The goal of the second model is to understand the effect of metabolic alterations typical for Alzheimer's disease on functional magnetic imaging that uses the BOLD signal. BOLD fMRI relies on local changes in the level of oxygen in the brain to infer neuronal activation. Changes in the oxygen level result from both an altered blood flow and the metabolic response to an increased demand for energy following stimulation. To study these processes I have build a new model that covers the main pathways of brain energy metabolism and the hemodynamic response. One important new feature is the inclusion of a detailed description of the pentose phosphate pathway. I have used the model to analyse three different scenarios that describe changes in enzyme concentration and tissue composition typical for Alzheimer's disease. The results highlight the sensitivity of the hemodynamic response to the underlying metabolic network. The inclusion of the model into a workflow for the generation of personalized models of the hemodynamic response exemplifies a possible route towards the application of mathematical models in the clinical practice.

Zusammenfassung

Auch mehr als einhundert Jahre nach ihrer ersten Beschreibung sind die genauen Ursachen der Mehrzahl aller Alzheimer-Fälle unbekannt. In dieser Arbeit beschreibe ich die Entwicklung, Analyse und Verwendung zweier mathematische Modell die sich mit unterschiedlichen Aspekten dieser Krankheit beschäftigen.

Die Produktion, Aggregation und der Abtransport des Peptids Aβ stehen im Fokus des ersten Modells. Aβ steht im Zentrum der sogenannten *Amyloid-Hypothese*, welcher zufolge ein Ungleichgewicht zwischen Produktion und Abbau und ein damit einhergehender Aβ Überschuss ursächlich für das Entstehen der Alzheimer-Krankheit ist. Um den Einfluss der zwei Transporter ABCC1 und ABCB1 auf den Abtransport von Aβ aus dem Gehirn zu untersuchen habe ich ein phenomenologisches Modell entwickelt, welches die Dynamik der *in vivo* Aggregation von Aβ in Mäusen erfasst. Grundannahmen des Modells sind Aggregation durch Kernbildung mit anschliessender Monomer-Anlagerung, Entfernung von Aβ durch ABC-Transporter und ein negativer Einfluss größerer Aggregate auf diesen Transport. Mithilfe dieser Annahmen kann ich zeigen dass der Unterschied in den Zeitreihen der Aβ-Ablagerungen zwischen verschiedenen Mausmodellen allein durch die Transportkapazität erklärt werden kann. Dieses Ergebnis ist ein wichtiger Schritt hin zur Entwicklung von Interventionen, um Produktion und Abbau von Aβ in der Waage zu halten.

Ziel des zweiten Modelles ist es, den Einfluss Alzheimer-typischer Veränderungen im Energiestoffwechsel auf das bei funktioneller Magnetresonanztomographie verwendete BOLD-Signal zu verstehen. BOLD fMRT verwendet Änderungen in der Sauerstoffsättigung des Blutes um Areale neuronaler Aktivität zu identifizieren. Änderungen im Sauerstoffgehalt resultieren sowohl aus einem veränderten Blutstrom als auch aus erhöhtem Verbrauch von Sauerstoff infolge neuronaler Aktivität. Zur Untersuchung dieser Prozesse habe ich ein neues Modell entwickelt welches die wichtigsten Komponenten des Energiemetabolismus im Hirn beschreibt. Mithilfe dieses Modells habe ich verschiedene Alzheimer-typische Veränderungen in Enzymkonzentration und Gewebezusammensetzung analysiert. Die Ergebnisse belegen die Sensitivität des BOLD-Signals auf Änderungen in den zugrunde liegenden metabolischen Netzwerken. Anhand der Verwendung des Modells zur Generierung personalisierter Modelle für die hemodynamische Reaktion wird eine exemplarische Anwendung mathematischer Modelle in der klinischen Praxis aufgezeigt.

Contents

List of Figures

List of Tables

1. Understanding the mechanisms and impact of Alzheimer's disease

Alzheimer's disease (AD) is the prevalent type of dementia, responsible for about 60% to 80% of the estimated 44.4 million people affected by dementia worldwide today (Alzheimer's Association, 2014). The disease was first described by Alois Alzheimer in 1906 (Alzheimer, 1907) and is characterized by the ICD-10[1] code G30 with the following words: "Alzheimer's disease is a primary degenerative cerebral disease of unknown etiology with characteristic neuropathological and neurochemical features. The disorder is usually insidious in onset and develops slowly but steadily over a period of several years" (World Health Organization, 1992). Althought this description is several years old, its main propositions are still true[2]. Today, more than one hundred years after the first description of the disease, the "unknown etiology" and the "insidious onset" are the two main problems faced by researchers trying to understand and ultimately cure the disease.

However, it would be wrong to assume that there has been no progress in the last 100 years. Alzheimer's disease has been studied intensively and many different hypotheses about the underlying causes have been developed. The most prominent of these hyptheses is termed "amyloid hypothesis" and states, briefly, that the aggregation of the protein amyloid beta (Aβ) is the reason, and not only a consequence of the disease (Finder and Glockshuber, 2007). Aβ, is a peptide consisting of 36 to 44 amino acids and is produced by the cleavage of the Amyloid-Precursor protein (APP). The extracellular plaques built by aggregated Aβ fibrils have been the prime suspect for the cognitive decline associated with AD for many years. Drugs have been developed to break up these plaques, and clinical studies have been undertaken to assess the effectiveness of this therapeutic approach. Unfortunately, these studies were mostly failures (Cummings et al., 2014).

Compared to the unknowns associated with Alzheimer's disease, the pure numbers of the prevalence of dementia are quite clear. Figures from the World Alzheimer Report 2009 which had a special focus on the prevalence of dementia worldwide, estimated the prevalence in developed countries for males in the age group 60 to 64 to be 0.4% (Females

[1] International Statistical Classification of Diseases and Related Health Problems (ICD)
[2] The draft of 11th revision of the ICD scheduled for 2018 contains the same wording.

0.4%), a number nearly doubling every five years and reaching values of 22.1% for males in the age group of 90+ (Females 30.8%) (Prince and Jackson, 2009). For Germany these numbers are even higher, as estimated in a study by the "Rostocker Zentrum zur Erforschung des Demografischen Wandels" from 2009. Here, the authors predicted a rise from 0.8% for males in the age group 60 to 64 (Females 0.6%) towards 29.7 % for males aged 95+ (Females 38%) (Ziegler and Doblhammer, 2009). While these predictions may have been a bit too pessimistic, with newer estimates being slightly lower, the projected increase in the absolute number of AD cases following a demographic shift towards an elderly population have been confirmed (Bickel, 2016). With today about 1.6 million people diagnosed with AD in Germany, this number is expected to rise to 3.0 million people in 2050, if no progress is made in either prevention or cure (Bickel, 2016).

Given these numbers and the still unknown etiology it becomes clear, that there is still a lot of work to do towards the understanding of the mechanisms that govern Alzheimer's disease. In this work, which consists of two main parts, I will describe my contributions to two projects that deal with different aspects of AD.

Part I – Modelling the aggregation of amyloid beta in mice

Part I of this thesis describes a joint project between the Systems Biology and Bioinformatics group at the University of Rostock[3] and the Neurodegeneration Research Laboratory (NRL) at the University of Rostock[4]. Experimental data from mice lacking different transport proteins obtained at the NRL showed differences in the measured Aβ burden over time. The goal of this project was to understand the mechanisms that govern Aβ aggregation and removal from the brain with a special focus on ATP binding cassette transporters. This goal was achieved with the help of a newly constructed phenomenological mathematical model that describes *in vivo* Aβ aggregation and removal. Chapter 2 introduces the biological background and gives a detailed explanation of the motivation and research questions of this project. Chapter 3 describes the measurement and statistical analysis of the experimental data used, and Chapter 4 discusses earlier mathematical models of protein aggregation. The model I have developed to describe *in vivo* protein aggregation and removal is described Chapter 5. Chapter 6 highlights the results of the project and discusses their implications. The work has been published in the *Journal of Clinical Investigation* as (Krohn et al., 2011) and has received considerable attention with more than 80 citations to date[5].

[3] www.sbi.uni-rostock.de
[4] www.pahnkelab.eu
[5] Google scholar lists 86 citations, looked up on 17.05.2017

Part II – Modelling the brain energy metabolism in humans

Part II of this thesis describes my contribution to the "VPH DARE@IT" project. This EU-funded VPH project promised to improve the early differential diagnosis of dementia with the help of information technology. My part in this project was the development of a new mechanistic model of brain energy metabolism and the hemodynamic response to neuronal stimulation. This model can be used to analyse the impact of changes in enzyme concentration and tissue composition on blood-oxygen-level dependent functional magnetic resonance imaging (BOLD fMRI), an important imaging modality in clinical diagnosis of AD.

Chapter 7 gives more background on the importance of brain energy metabolism in Alzheimer's disease and it's relation to BOLD fMRI. It also presents the research objectives of the second part of this thesis and gives some more information about the "VPH DARE@IT" project. Chapter 8 describes the relevant pathways of brain energy metabolism and lists several alterations that have been observed in AD patients. Chapter 9 discusses earlier models of (brain) energy metabolism that can be considered the ancestors of my model. The construction and implementation of this new model of brain energy metabolism and the hemodynamic response makes up Chapter 10. Analysis of the model and several literature-derived scenarios as well as a discussion of its relevance and clinical application is described in Chapter 11. The model and its analysis have been published in the *Journal of Cerebral Blood Flow and Metabolism* (Winter et al., 2017).

Part III - Conclusions

Part III of this thesis contains conclusions that discuss the main aspects of both Part I and Part II.

Some of the references, especially for the first part of this thesis are already several years old. I have decided to include these articles as they have been my source of reference at the time I was working on the project.

Part I.

Modelling the aggregation of amyloid beta in mice

Protein aggregation, Alzheimer's disease and the blood brain barrier

Protein aggregation, i.e. the misfolding and progressive polymerization of otherwise soluble proteins has been implicated in many diseases, including Parkinson's disease, Huntington's disease, amytrophic lateral sclerosis, prion diseases and most notably Alzheimer's disease (Selkoe, 2004; Ross and Poirier, 2004). For AD, it is *the* decisive hallmark. The extracellular plaques formed by the accumulation of the protein amyloid beta (Aβ) have not only been the first physiological abnormality described by Alois Alzheimer in 1906 (Alzheimer, 1907), but they are still today the only feature that allows the diagnosis of "pathophysiologically proved AD dementia" (McKhann et al., 2011). In other words, aggregation of Aβ is the only feature which allows to unambiguously differentiate AD from other types of dementia. Due to the importance of protein aggregation for different diseases, much research has focused on the two questions: (1) Why do proteins aggregate? (2) How do proteins aggregate?

The first of these two questions: *Why do proteins aggregate?*, can be rephrased to ask: *Which specific circumstances allow proteins to aggregate?* And the answer to this question is seemingly quite simple. According to Roberts (2007) "[...] essentially any protein or polypeptide can form non-native aggregates in solution if incubated for sufficient time without intervention of other processes such as chemical or proteolytic degradation". Consequently, for many years the main question for research on Aβ was not so much why Aβ tends to aggregate, but how it is produced in the first place. The first paragraphs of Chapter 2 provide a concise overview about what is known about this process.

The main focus of this work is, however, not the production of Aβ, but instead two possible routes it can take in the brain. The first route, its aggregation via several intermediate steps into plaques is described in Section 2.1. The second route, the removal of Aβ from the brain via the blood brain barrier is discussed in Section 2.2. In this work, especially the transport of Aβ by a specific class of transport proteins, the so-called ABC transporters, will be considered. By doing so, I concentrate on the second question mentioned above: *How does Aβ aggregate?*

Following the postulation of two guiding research questions in Section 2.3, I describe the experimental data used for this project in Chapter 3. Chapter 4 gives a review of the history of computational models of protein aggregation, both in AD an beyond. My own model, encompassing *in vivo* production, aggregation and removal of Aβ in mice is described in Chapter 5. This model, as well as most of the results discussed in Chapter 6 have been published in (Krohn et al., 2011) and parts of Chapter 5 and Chapter 6 are close to the description in this publication.

2. Biological background and motivation

Aβ is produced by cleavage of the amyloid precursor protein (APP). APP itself is an ubiquitous membrane-bound protein and is cleaved first by either an α-secretase or a β-secretase and subsequently by a γ-secretase. Initial cleavage by an α-secretase leads to the non-amyloidogenic pathway while initial cleavage by a β-secretase is the first step in the amyloidogenic pathway (See Figure 2.1, p10). The non-amyloidogenic pathway produces sAPPα as a result of α-secretase cleavage, the fragment P3, and the APP intracellular domain (AICD) as a result of γ-secretase cleavage. The amyloidogenic pathway produces sAPPβ as a result of β-secretase cleavage but more importantly it also produces the crucial Aβ and AICD as a result of γ-secretase cleavage (Claeysen et al., 2012).

It has been shown that for all three secretases more than one protein complex or proenzyme can fulfil their role. For α-secretase this includes members of the A disintegrin and metalloproteinase (ADAM) family. For the β-secretase both BACE1 and BACE2 have been identified. The γ-secretase complex is composed of nicastrin (Nct), anterior pharynx defective one (APH1), presenilin enhancer 2 (PEN2) and either presenilin 1 (PSEN1) or presenilin 2 (PSEN2) (Claeysen et al., 2012). All three secretases are regulated by a plethora of modulators, which influence their synthesis, their assembly, their trafficking and their activity (Claeysen et al., 2012). While a more detailed description of these processes is outside the scope of this work, the mechanisms of Aβ production are important for the distinction between different types of AD commonly made.

Each occurrence of AD can be classified either as early onset Alzheimer's disease (EOAD) or as late onset Alzheimer's disease (LOAD). The typical age of onset for EOAD is less than sixty years, compared to an onset in people older than sixty years which characterizes LOAD. While the neuropathologic and clinical features of both kinds of AD are generally indistinguishable (Selkoe (2002) quoted by LaFerla and Green (2012)) there is an important difference in the understanding of their respective etiology. This difference is most apparent in the alternative naming of both types of AD, with EOAD being referred to as "familial AD", while LOAD being called "sporadic AD". The latter distinction, familial versus sporadic, is due to the differences in the understanding of the main disease cause for each group of AD cases.

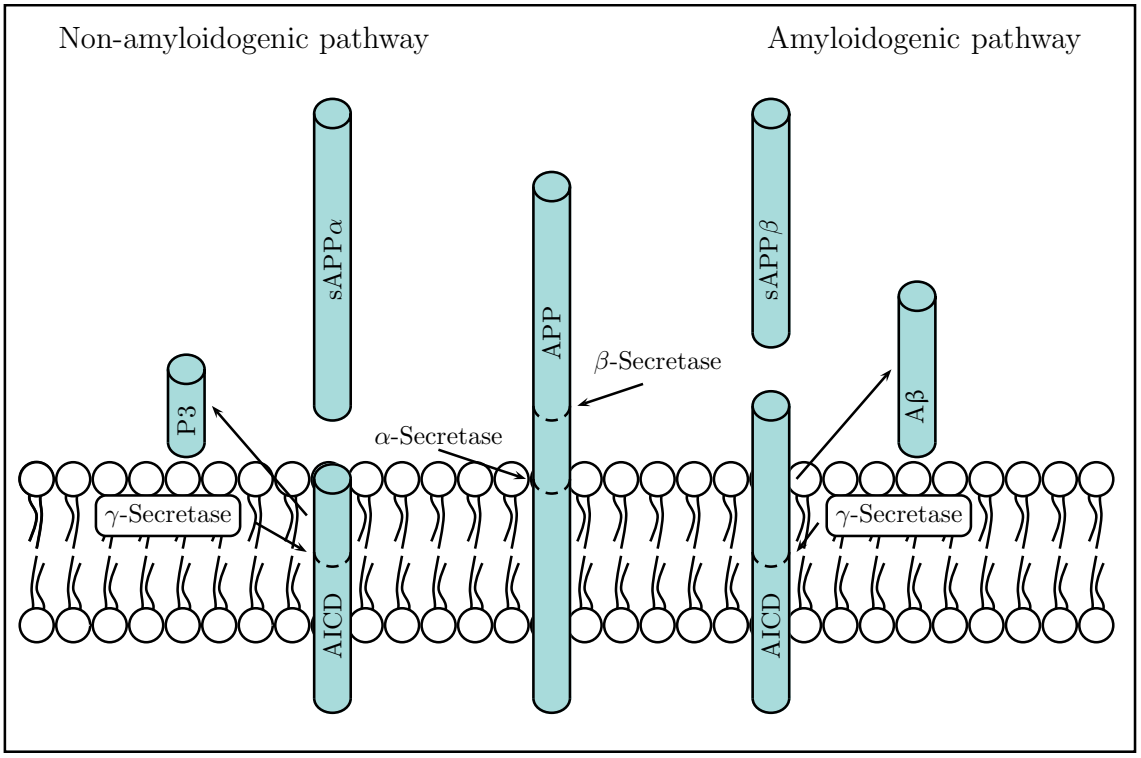

Figure 2.1.: APP cleavage by α, β, and γ-secretase decides between amyloidogenic and non-amyloidogenic pathway.

For EOAD, mutations in the genetic loci of three genes, namely APP, PSEN1 and PSEN2, have been identified. Specifically, more than "200 distinct disease-causing mutations are known across these genes [...]" (Bertram et al., 2010). These mutations are sufficient to contract EOAD and are passed on to successive generations by Mendelian inheritance, hence the name "familial AD". In contrast, the etiology of LOAD is still unknown and only sporadic hints towards the cause for disease initiation exist. Among these hints are again genetic variations, the most prominent being the $\epsilon 4$ allele of the apolipoprotein E gene. But unlike in EOAD, these alterations are only *risk factors* and do not inevitably lead to AD (Tanzi, 2012).

Unfortunately the patients diagnosed with LOAD, i.e. the cases with unknown etiology, make up the majority of all AD cases. Different sources claim numbers ranging from only 1% to 5% of all AD cases for being familial AD, while the remaining 99% to 95% are sporadic (Alzheimer's Association, 2014; Claeysen et al., 2012). Combining these two facts it becomes clear that currently only for a very small minority of all AD cases the etiology is understood.

But while EOAD is only a very tiny part of the big problem AD poses, the underlying genetic mutations have been used to great effect to increase the understanding of late

onset Alzheimer's disease. The main reason for this is that animal models for AD can be established based on these mutations (LaFerla and Green, 2012). The database of animal models of Alzheimer's disease and related neurodegenerative diseases lists currently 103 mouse models, 102 of them for AD (http://www.alzforum.org/res/com/tra). Two of these mouse models (APPPS1 (Radde et al., 2006) and APPDutch (Herzig et al., 2004)) were used in the work presented here (cf. Section 3.2). Both animal models have in common that they contain a genetic modification (or mutation) which is also found in EOAD. These mutations lead to an increased production of Aβ in both mouse models compared to the wild-type, and thereby guarantee that the typical signs of AD, extracellular plaques of Aβ, develop during the life time of a mouse. This setting can consequently be exploited to analyse the pathways for Aβ aggregation in the mouse brain and to assess the influence of the different mechanisms for Aβ clearance. Each of the following two sections deals with one of these two aspects.

2.1. Mechanisms and regulation of protein aggregation in AD

The work at hand is concerned with the subject of protein aggregation in Alzheimer's disease. Still, the realm where the process of proteins agglomerating and clumping is of importance is much bigger, and much of the work in this field has been done with proteins other than Aβ. While there are significant differences in the structures of the proteins for which aggregation has been observed, there exist a series of common steps which can be used to delineate a typical pathway of aggregation. To avoid the fate of a too general view on the topic, I will restrict the overview to protein aggregation in neurodegenerative diseases.

In neurodegenerative diseases, protein aggregation is usually initiated by a conformational change in the protein structure. For this change to occur, there needs to be an ensemble of interconvertible conformations between which the protein structure can switch (Roberts, 2007). For Aβ at least three different conformations have been discussed: α-helical conformation, random coil conformation and β-sheet conformation (Finder and Glockshuber, 2007). These types of secondary structures differ in the location of the hydrogen bonds which connect the amino and carboxyl groups of the protein. The β-sheet conformation has been reported in the aggregates of Aβ (in AD), α-synuclein (in Parkinson's disease (Der-Sarkissian et al., 2003)) and polyglutamine (in Huntington's disease (Poirier et al., 2005)). A pathway leading to these aggregates has been described for these diseases that consists of several steps. The following characterization is mainly based on the review by Finder and Glockshuber (2007).

- For the aggregation to begin, *the intrinsically folded proteins need to unfold.* Among the various reasons for this unfolding are proteolytic cleavage (e.g. in AD), oxidative modification (e.g. in PD) or phosphorylation (e.g. in spinocerebellar ataxia (SCA) and PD) (Poirier et al., 2005). In Alzheimer's disease, proteolytic cleavage seems to be the most important reason for aggregation. While intact APP has very little tendency to aggregate, the different types of Aβ tend to aggregate quite fast (Poirier et al., 2005).

- After unfolding, the next common step described in the literature is the *formation of so-called* seeds*, which constitute the smallest stable protein aggregates.* These seeds, sometimes called *nuclei* or *paranuclei* consist of five to six monomers (Roychaudhuri et al., 2009). While aggregation may begin even without the occurrence of seeds, they increase the rate of aggregation and mark one of the first irreversible steps. The importance of these first small aggregates is reflected in the term *seeded growth*, a common term for the process of protein aggregation.

- The initial formation of seeds is followed by the *formation of Aβ oligomers*, small, soluble aggregates of varying size. Prominent representatives which have been reported in several studies include Aβ-derived diffusible ligands (ADDLs), globular assemblies about 4.8 to 5.7 nm in size (Broersen et al., 2010) and Aβ56*, an apparent dodecameric assembly with a molecular weight of 56kDa (Haass and Selkoe, 2007). While there exist several different hypotheses about the importance of the different-sized Aβ oligomers, one common attribute of all these small soluble aggregates is their neurotoxicity. The hypotheses about the mechanisms by which neurotoxicity is exerted include oxidative stress, the formation of ion channels, membrane disruption and initiation of mitochondrial dysfunction, to name just a few. A detailed description of the different mechanisms would fill a book on its own and is not part of the work at hand.

- The next step in protein aggregation is the *formation of protofibrils* which have a flexible, rod-like structure and have a size of < 200 nm. Protofibrils are soluble and have also been reported to be neurotoxic.

- These protofibrils mature into Aβ *fibrils* which can be described as "thermodynamically stable, structurally organized, highly insoluble, filamentous protein aggregates being composed of repeating units of β-sheets".

- *Plaques*: The largest amyloid beta aggregates which have been observed in post-mortem analysis of AD-patients are called plaques. These plaques are the final stage of protein aggregation in AD. Plaques are insoluble and do not correlate with disease progression.

Although the aggregates of different size can each be characterized, the exact pathway for aggregation is still unclear. One important open question is whether all of the intermediates will finally aggregate into plaques or whether some of the smaller aggregates which haven been observed are the product of alternate aggregation routes and are not integrated into protofibrils, fibrils or plaques. The main categories of the aggregates which are important for this work are *soluble* versus *insoluble* and *neurotoxic* versus *non neurotoxic*, as will be discussed in Chapter 3. Other questions regarding the regulation of protein aggregation in neurodegenerative diseases which have been analysed and are ignored here are for example the influence of aggregation conditions *in vitro* (Lee et al., 2007).

The last two sections dealt with production and aggregation of Aβ in the brain. The next section will describe the clearance of Aβ from the brain with a special focus on its removal by ATP binding cassette transporters.

2.2. Clearance of Aβ from the brain

Clearance of Aβ from the brain parenchyma can be achieved by two means. The first way of clearance is the peptidolytic removal of Aβ inside the brain, i.e. the degradation by proteolytic enzymes. The second way of removal is the transport of Aβ through the blood-brain barrier (BBB) and its subsequent degradation in the blood (Figure 2.2, p14).

Enzymatic degradation of Aβ in the brain has received considerable attention and several enzymes have been reported with the ability to cleave Aβ (Tanzi et al., 2004; Wang et al., 2006; Rogeberg et al., 2014). The four most prominent enzymes associated with the degradation of Aβ are the insulin degrading enzyme (IDE) and neprilysin (NEP) which are involved in extracellular degradation, and endothelin converting enzyme (ECE)-1 and cathepsin D (Cat D), which are involved in intracellular degradation (Rogeberg et al., 2014). Other enzymes have been suggested as well. (Rogeberg et al., 2014; Wang et al., 2006). All of these enzymes are not specific for a single substrate but hydrolyse several different peptides, including Aβ. This multi-substrate nature is common for proteases and needs to be considered in the development of drugs that influence their activity.

The second means of Aβ clearance is its removal from the brain by transport through the BBB and its subsequent degradation in the blood. The crossing of the blood-brain barrier is worth special attention as this barrier consists of a set of mechanisms which aim to prevent unsupervised traversing.

Tight junctions are formed between neighbouring brain endothelial cells to prevent diffusion. These junctions are composed of different proteins, including occludin, claudin-3,

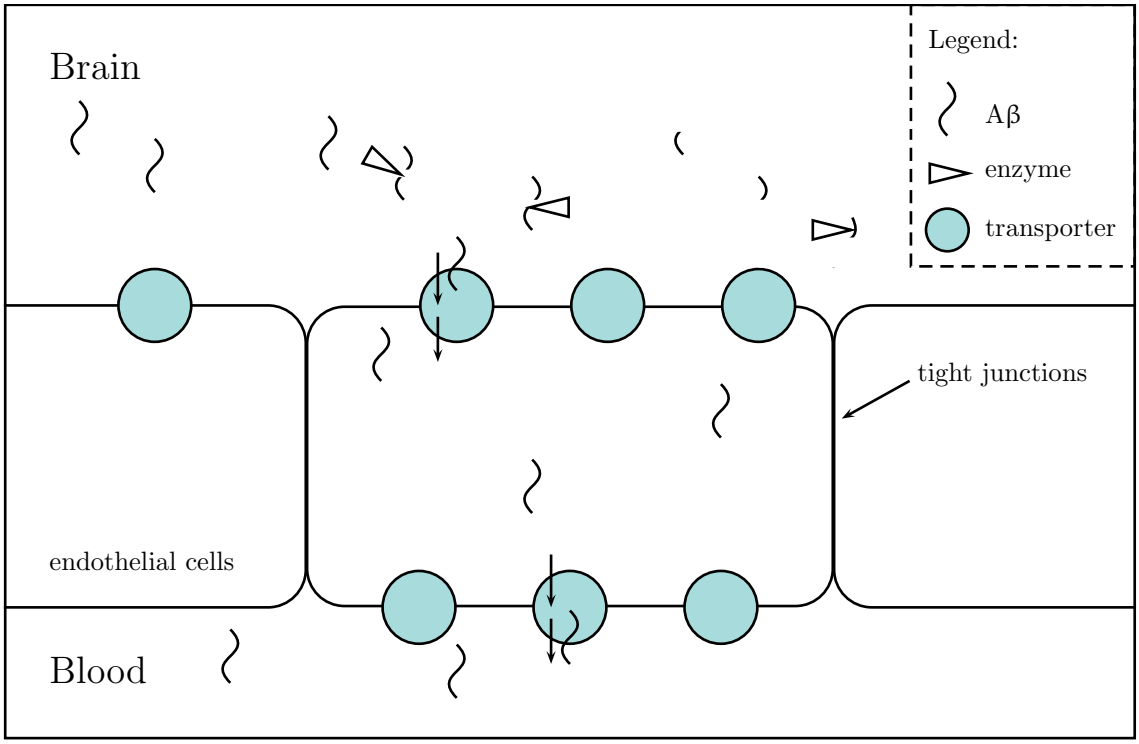

Figure 2.2.: One feature of the blood brain barrier are tight junctions between the endothelial cells that prevent diffusion. Two main mechanisms of removal of Aβ exist: Enzymatic degradation inside the brain and the removal of Aβ from the brain by different transport mechanisms.

5 and -12, and several zonula occludens proteins, to name just a few (Zlokovic, 2008). As tight junctions effectively prevent diffusion from blood to the brain and vice versa, a complex transport machinery is necessary to support the brain with fuel and dispose of waste and other unwanted molecules. This transport machinery is composed of carrier mediated transporters, ion transporters, active efflux transporters and receptor mediated transport. Carrier mediated transporters are responsible for the transport of nutrients such as glucose, amino acids, monocarboxylic acids, vitamins and many other substrates (Zlokovic, 2008). Ion transporters mainly regulate the influx and efflux of sodium, potassium and chloride ions to establish a concentration gradient for sodium and regulate the intracellular pH. The remaining two transport mechanisms, active efflux transporters and receptor mediated transport are responsible for the exchange of a multitude of substrates whose description is out of the scope of this work. Both mechanisms have been, however, implicated in the transport of Aβ.

Receptor-mediated clearance includes several processes that transport Aβ through the blood-brain barrier. The first two receptors historically implicated in the trafficking of Aβ were the lipo-protein receptor-related protein (LRP) and the receptor for advanced glycation end products (RAGE) (Tanzi et al., 2004). The main difference with respect

to their importance in AD is that LRP is expressed at the abluminal side of the BBB and mediates the efflux of Aβ from the brain while RAGE, which is expressed luminally, can transport Aβ from the periphery back into the central nervous system. Binding of Aβ to LRP can either be realized via the preceding formation of a complex consisting of Aβ and one of the other LRP ligands such as apoE or α2M, or via a direct interaction of Aβ and LRP (Tanzi et al., 2004). For RAGE no preceding complex formation has been observed. For both receptors the resulting receptor-substrate complex can either be delivered to the lysosomes for subsequent degradation or transported across the BBB via transcytosis (Pflanzner et al., 2010).

Transporter-mediated clearance is the second group of processes which remove Aβ from the brain. The transporters involved in the transport of Aβ belong to the ATP-binding cassette (ABC) transporter superfamily and are the main mechanism of interest for Aβ removal in this work.

The ABC transporter superfamily

The ATP-binding cassette transporter superfamily presents the largest family of transmembrane proteins (Dean et al., 2001) and has been found in all species (Higgins, 2001). Seven mammalian ABC gene subfamilies are discriminated, ABCA to ABCG (Dean et al., 2001). Transporters are classified as belonging to the ABC transporter superfamily according to their ATP-binding sites (nucleotide binding folds, NBF). In addition to two NBFs, full ABC transporters have two transmembrane domains (TM). There exist also half transporters which are composed of only one NBF and a single TM. These half transporters can form homodimers or heterodimers to work as transporters. Most ABC transporters act as unidirectional transporters for a wide array of substrates (Dean et al., 2001). The subfamilies ABCE and ABCF are an exception inside the ABC transporter superfamily, as members of these families do not have a transmembrane domain and are not known to be involved in transport (Dean et al., 2001).

Of special interest for this work are those ABC transporters, which are expressed at the blood-brain barrier. These are ABCA1, ABCB1, ABCC1 and ABCG2 (Dean et al., 2001). The latter three transporters have also been implicated in multidrug resistance. ABCB1 in particular can affect drug transport, and has been shown to confer multidrug resistance in cancer cells. In the context of Alzheimer's disease three ABC transporters have previously received particular attention, as they have been implicated in the removal of Aβ from the brain: ABCA1, ABCG2 and ABCB1.

- ABCA1 is highly expressed in astrocytes, neurons and the brain capillary (Pflanzner et al., 2010). While ABCA1 does not bind Aβ directly, studies with mice over-expressing ABCA1 showed reduced Aβ deposits in brain parenchyma (ElAli and Rivest, 2013). As a functional link the transport of phospholipids has been suggested, which influences ApoE lipidation state. Highly lipidated ApoE binds more effectively to Aβ and thereby prevents its accumulation and allowing its removal from the brain (ElAli and Rivest, 2013). Accordingly, studies with ABCA1$^{(-/-)}$ mice showed a significant increase in soluble Aβ 40 in the brain (Pflanzner et al., 2010).

- ABCG2 is highly expressed in many organs, including liver, kidney, prostate, testis, ovary, placenta, the CNS and the endothelium of the nervous system (Pflanzner et al., 2010). In contrast to ABCA1, ABCG2 is able to bind Aβ directly and has been suggested to prevent the uptake of blood-borne Aβ into the brain (Pflanzner et al., 2010). ABCG2 is also known as breast cancer resistance protein (BCRP).

- ABCB1 is highly expressed in the gastrointestinal tract, the kidneys, liver and at the blood brain barrier (Pflanzner et al., 2010). Several studies have tried to illuminate the role of ABCB1 in the transport of Aβ and it has been shown that Aβ can bind to ABCB1 and is subsequently removed from the brain (ElAli and Rivest, 2013). Other names for ABCB1 include p-glycoprotein (P-gp) and multidrug-resistance protein 1 (MDR1).

In this work, I specifically focus on the effect of ABCC1 on Aβ aggregation. ABCC1, while being expressed at the blood brain barrier, has been out of the focus of Alzheimer's research until very recently. Instead, it has received attention for its broad substrate specificity and ubiquitous expression (Bakos and Homolya, 2007).

ABCC1 has been discovered in 1992 in a multidrug resistant human lung cancer cell line and presented the first member of the ABCC family. It has later been described to transport a wide array of substrates, including several anticancer drugs and HIV protease inhibitors. ABCC1 is ubiquitously expressed throughout the human body. In the brain, high values of ABCC1 have been reported in the capillary cells and glia cells, amongst other cell types. For a detailed review of the expression, the regulation, the proposed mechanism of transport and the role in disease of ABCC1 see (Bakos and Homolya, 2007).

In summary, while there is evidence that at least ABCA1, ABCG2 and ABCB1 are implicated in trafficking of Aβ across the blood brain barrier, the main interest in ABCC1 has been outside the area of Alzheimer's research. New experimental evidence, however, as described in the next section, suggested an important role of ABCC1 in the clearance of Aβ. This evidence lead to questions which I strive to answer in the following chapters.

2.3. Research question

Experiments with two different mouse models of Alzheimer's disease in the neurodegeneration research laboratory of Prof. Jens Pahnke at the University of Rostock produced time series data of Aβ load in the brain of adult mice. The mice, expressing Swedish mutant human APP (APPswe) and mutant presenilin 1 (PS1) lacked specific ABC transporters. The first model, $APP/PS1 \times Abcb1^{-/-}$ lacked ABCB1, the second model $APP/PS1 \times Abcc1^{-/-}$ lacked ABCC1 (See Section 3). The data, depicted in Figure 2.3 show a constant increase in the concentration of soluble Aβ in both mice models until an age of 150 days. This increase is mirrored in the levels of insolube Aβ which increases until the end of the measurements (175 days). While the levels of soluble Aβ in the ABCB1-deficient mice continue to increase until the end of the measurements, the values of soluble Aβ in the ABCC1-deficient mice show an unexpected decrease at the age of 175 days (Figure 2.3, top left panel).

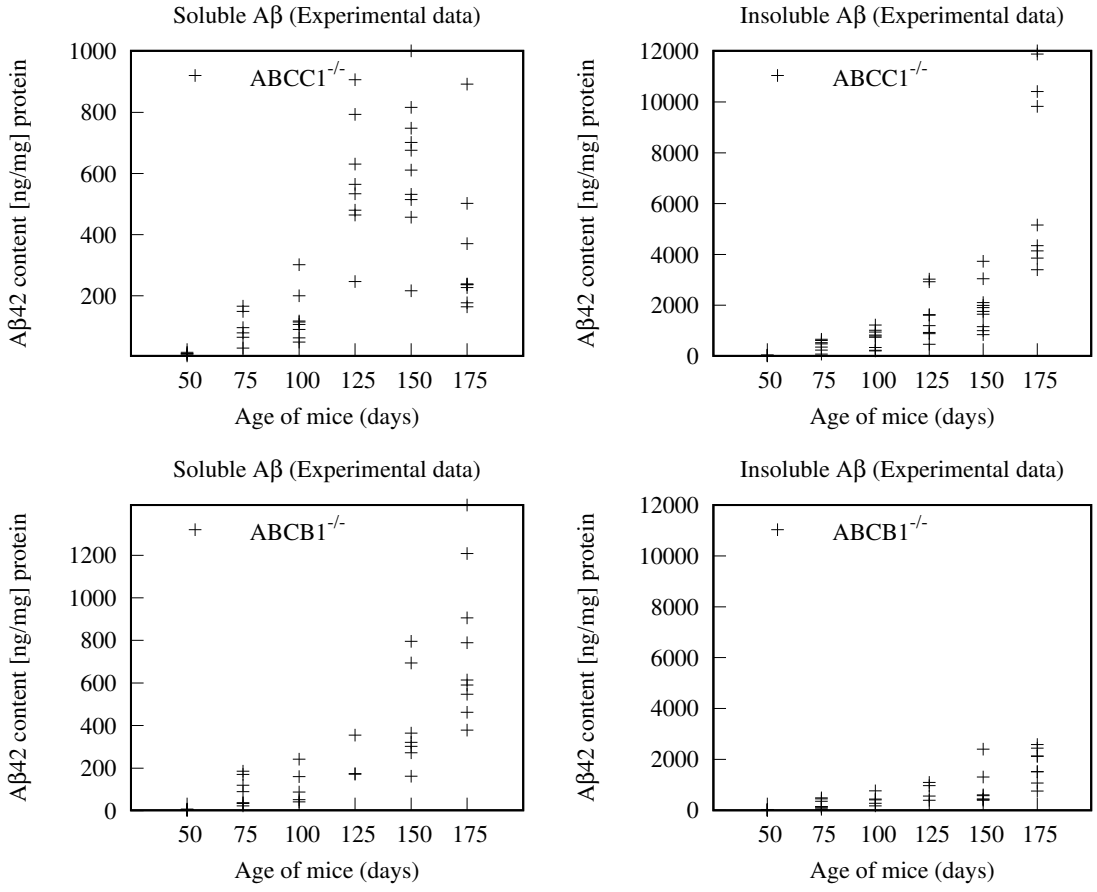

Figure 2.3.: Time series data measured in two mice models with specific transporter knockout. The top row shows data for soluble and insoluble Aβ for $ABCC1^{-/-}$ mice. The lower bar shows data for soluble and insoluble Aβ for $ABCB1^{-/-}$ mice.

These measurements not only indicate that ABCC1 plays in important role in the trafficking of Aβ but they also give rise to the following two groups of questions:

1. Which mechanisms are necessary to model protein aggregation *in vivo*? Can the time course data of soluble and insolube Aβ be explained by a mathematical model? In other words: 'How' does protein aggregation occur?

2. Can this mathematical model be used to quantify the influence of the missing transporter proteins? In other words 'How big' is the influence of the different transporters.

The question for the mechanisms of protein aggregation and the influence of the ABC transporters can be further refined to ask for the specific circumstances which led to the observed decrease in the soluble Aβ fraction in the ABCC1-deficient mice.

All these questions are exemplary for the type of questions that can be answered with mathematical modelling in that they ask 'How' in a quest for a mechanistic understanding of the biological question and 'How big' in an attempt to quantify the impact of the different genetic background of the two mice models. If one is able to answer these questions, one might be one important step closer to answering a much more important question: Can influencing the expression of ABC transporters delay the onset of Alzheimer's disease?

Before I give an overview of the mathematical models available from the literature that have been build to answer similar questions, I will first use the next chapter to describe the experimental data at hand in a little more detail.

3. Measuring amyloid beta load in the mice brain

For a quantitative model to be useful, one has to be able to reasonably compare its outcome to given or expected experimental data. Given the high variability inherent in biological measurements from animals, no comparison between simulated data and experimental data can be done before a suitable description of the experimental data is available. The following section will outline the steps taken in measuring the data and the subsequent statistical analysis to determine reasonable values that can later be compared to simulation results.

3.1. Mouse models of AD

As mentioned in Chapter 2, mouse models expressing genetic mutations responsible for early onset Alzheimer's disease can be used to model AD progression. The measurements relevant for this work were done in two different mouse models. Both mouse strains express the Swedish mutant human Aβ precursor protein (APP) and mutant presenilin-1 (PS1) and lack a specific ABC transporter, giving rise to their name $APP/PS1 \times Abcc1^{-/-}$ and $APP/PS1 \times Abcb1^{-/-}$, lacking the ABCC1 and ABCB1 transporter, respectively.

For each mouse strain, samples were taken from mice at the age of 11 weeks, 14 weeks, 18 weeks, 22 weeks and 25 weeks. For each sample time up to 10 different measurements were taken[1].

3.2. ELISA measurements

Aβ load in the mice brain was determined with ELISA measurements. ELISA (enzyme-linked immunosorbent assay) is a diagnostic technique which allows the quantification of molecules based on the binding of the molecule of interest to specific antibodies.

[1] For the exact number of samples see Table 3.1 on page 23.

3. Measuring amyloid beta load in the mice brain

The samples were taken from whole brain hemisphere from which the cerebellum and brain stem had been removed at the level of the midbrain (Krohn et al., 2011). After homogenization, the samples were diluted with carbonate buffer and centrifuged to separate the (buffer-) soluble from the (buffer-) insoluble fraction. The insoluble fraction was dissolved in guanidine hydrochloride. For all samples also the total protein content was measured using a NanoDrop spectrophotometer. The resulting values are measurements of soluble Aβ and insoluble Aβ in ng/mg per total protein (Fig. 2.3).

Unfortunately, the exact distribution of aggregates of different sizes (monomers, oligomers, protofibrils, fibrils and plaques) in the soluble and insolube fraction is not known. Still, according to the sample preparation protocol it is expected that most of the smaller aggregates up to protofibrils are contained in the soluble fraction while the larger aggregates (fibrils and plaques) make up the insoluble fraction.

One important consequence of this distribution is that the aggregates considered neurotoxic (c.f. Section 2.1) belong to the soluble fraction. This information will later be used in the construction of the mathematical model.

In addition to the quantification of Aβ load also the size and density of Aβ plaques was determined using immunohistochemical staining. These data were not used for the mathematical model and are therefore not described here. A detailed description of the measurement process can be found in the publication of this work (Krohn et al., 2011).

3.3. Testing the data for an underlying random distribution

To describe a sample of measurements with a single characteristic value, several possibilities exist. If no information about an underlying distribution is available, the arithmetic mean, the geometric mean or the median can be used to aggregate several independent points of data. In biology, however, the assumption of an underlying normal distribution is often used as it not only allows to easily characterise the location of the sample (via the arithmetic mean, μ) but also gives a measure of the dispersion (via the variance σ^2 or standard deviation σ). In addition, the property of symmetry with respect to the mean and the possibility to calculate often used quantiles via an easy rule of thumb[2] have made the normal distribution (also called the Gaussian distribution) a workhorse in experimental biology. From a mathematical point, this choice needs to be questioned.

The most important critique of the use of the normal distribution to describe the variation in biological samples is that the probability for the appearance of negative values is

[2]For a normal distributed sample approximately 99.7% of all measurements fall in the area $\mu \pm 3 \cdot \sigma^2$

always greater than zero, while the measurement of biochemical quantities such as protein concentrations cannot result in negative values.

To overcome this shortcoming of the normal distribution, the preferential use of the lognormal distribution has been advertised in the last years (Limpert et al., 2001). The lognormal distribution can be defined in terms of an underlying normal distribution. If $\log(X)$ follows a normal distribution ($\log(X) \sim \mathrm{N}(\mu, \sigma)$), then X follows are lognormal distribution. Using the two shape parameters μ and σ from $\log(X)$ we can write: $X \sim \Lambda(\mu^*, \sigma^*)$ with $\mu^* = e^{\mu}$ and $\sigma^* = e^{\sigma}$. The two resulting parameters, the scale parameter μ^* and the shape parameter σ^* can be used to express the same rules which make the use of the normal distribution so enticing: The interval $[\mu^*/\sigma^*, \mu^* \cdot \sigma^*]$ contains 68.3 % of randomly drawn samples, the interval $[\mu^*/(\sigma^*)^2, \mu^* \cdot (\sigma^*)^2]$ contains 95.4 % of randomly drawn samples and the interval $[\mu^*/(\sigma^*)^3, \mu^* \cdot (\sigma^*)^3]$ contains 99.7 % of randomly drawn samples.

One immediate conclusion from these rules is that the error bars for lognormal distribution are asymmetric, with a higher likelihood of large values. This means that the lognormal distribution is positively skew, i.e. the likelyhood for a value drawn from the distribution to be larger than the arithmetic mean is greater than the likelihood to be smaller than the arithmetic mean. The lognormal distribution does therefore also account for the rare appearance of very high values (compared to the mean) which under the assumption of normal distributed data are often considered *outliers*[3] and are removed from the experimental data.

Besides these practical considerations on the use of the normal distribution and the lognormal distribution to describe the location and dispersion of experimental data there is also a more technical difference between these two, which can be used to argue in support of the preference of the assumption of lognormal distributed data.

One of the interesting properties of the normal distribution is its relation to the additive central limit theorem. According to this theorem, the arithmetic mean of a large number of independent random variable will be approximately normal distributed. Following this theorem, we can assume that if we apply an additive model of random error for a series of reactions and measurements, the resulting data should follow a normal distribution. However, the model of additive error is not well suited for biochemical reactions. Following the well established concept of mass-action kinetics, the rate of a reaction depends on the product of the individual substrate concentrations and a rate constant. Any variation in either the concentrations or the rate constant would therefore be multiplied rather than added. Multiplicative error propagation instead of additive error propagation leads to a

[3]Including these so-called outliers in the calculation of the mean and variance may have an enormous impact on the estimated mean an variance.

lognormal distribution of the resulting random variable.

To test whether the assumptions that the measured data follows either a normal distribution or a lognormal distribution can be rejected, I applied the Lilliefors goodness-of-fit test. This test is based on the Kolmogorov-Smirnov test, which can be used to test whether a set of observations could be from a completely specified continuous random distribution. The Lilliefors test uses the same test statistics as the Kolmogorov-Smirnov test, but the table of critical values takes into account that the mean and variance (for an assumed normal distribution) are not known and have to be calculated from the sample (Lilliefors, 1967). The test is suitable for the data at hand, as it can be used with small sample sizes. The results given in Table 3.1 were obtained using the function `lillietest()` from Matlab 2011b. The impact of the two possible assumptions — normal data vs. lognormal data — on the location of the mean and the size of the error bars is illustrated in Figure 3.1.

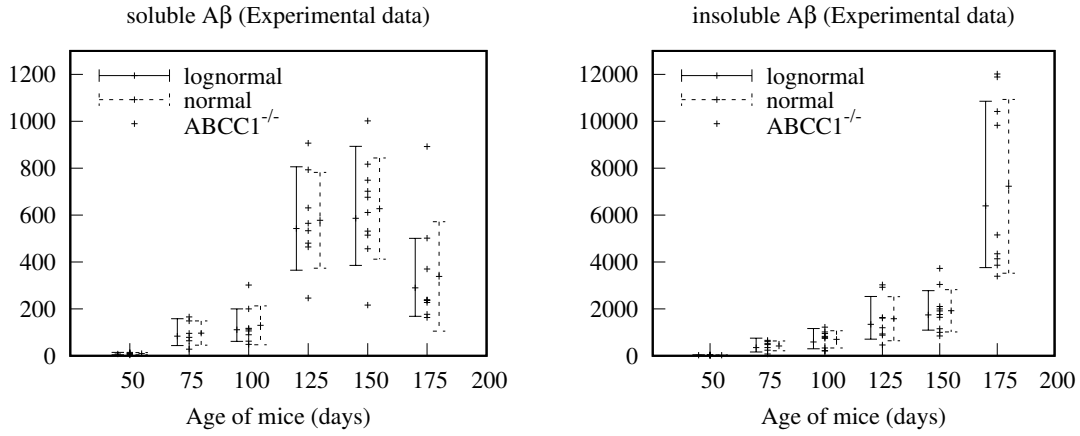

Figure 3.1.: Experimental data with calculated mean and error bars for the assumption of normal data (dashed) and the assumption of lognormal data (solid). Calculated mean and error bars for the assumption of normal and lognormal data are plotted with a positive and negative shift in time, respectively. Note the asymmetric error bars and the overall lower values of the mean value for the assumption of lognormal data.

Despite the small sample size, the assumption of normal distributed data was rejected for 4 out of 28 samples and the assumption of lognormal distributed data was rejected for 3 samples. This result is in line with the observation described by Limpert et al., who report that for most datasets with a small coefficient of variation, both distributions fit well (Limpert et al., 2001). Consistent with the observation of predominantly positive skew and strict positive sample data I discarded the assumption of normal distributed data. Mean values and confidence intervals were consequently calculated assuming an underlying lognormal distribution.

Table 3.1.: p-values for Lillietest of ELISA samples. *: for assumption of normal distributed data. **: for assumption of lognormal data. *** Values omitted from statistical analysis due to small sample size.

	11w	14w	18w	22w	25w
$Abcc1^{-/-}$ soluble					
P-value*	0.714	0.304	0.252	0.194	0.061
P-value**	0.324	0.023	0.916	0.749	0.159
n	7	9	8	10	9
skewness	0.16	-0.24	0.61	0.79	0.27
$APP/PS1 \times Abcc1^{-/-}$ insoluble					
P-value*	0.804	0.022	0.756	0.971	0.004
P-value**	0.834	0.348	0.297	0.483	0.015
n	6	8	8	10	9
skewness	0.16	1.20	0.13	-0.18	1.68
$ABCB1^{-/-}$ soluble					
P-Value*	0.322	0.500	***	0.056	0.209
P-Value**	0.483	0.862	***	0.436	0.560
n	7	5	***	7	9
skewness	0.38	0.62	***	0.75	0.8
$ABCB1^{-/-}$ insoluble					
P-Value*	0.023	0.349	***	0.007	0.428
P-Value**	0.457	0.885	***	0.054	0.292
n	8	5	***	7	8
skewness	0.53	0.69	***	1.45	-0.25
control group, soluble					
P-value*	0.162	0.162	0.127	0.082	0.546
P-value**	0.826	0.254	0.036	0.355	0.834
n	9	8	4	7	6
skewness	1.35	-0.60	- 0.70	1.11	0.14
control group, insoluble					
P-value*	0.487	0.227	0.794	0.305	0.219
P-value**	0.978	0.544	0.901	0.188	0.239
n	9	9	4	7	6
skewness	0.68	0.21	0.45	-0.51	0.48

4. Mathematical models of protein aggregation

The first research question developed in Section 2.3 is: "Which mechanisms are necessary to model protein aggregation *in vivo*?". To answer this question, I will first give an overview of the state of the art, i.e. mathematical models that have tried to capture the kinetics of protein aggregation. Given the importance of protein aggregation for many different diseases outlined in the beginning of Section 2.1, it will come as no surprise that there have been several attempts to describe and understand this process with the help of mathematics. According to Morris et al. (2009), an in-depth review of the protein aggregation literature, there is a common agreement that the first studies on protein aggregation have been published in 1959 and 1962 by Oosawa et al.. These studies, not related to neurodegeneration, focused on the polymerization of actin, a major multi-functional protein in eukaryotes, from the globular form to the fibril form. The authors assumed a mechanism of subsequent monomer addition, and modelled attachment and detachment of monomers as well as forward and reverse transformation of trimers to helical polymers (Oosawa et al., 1959).

In the following years, the mathematical analysis of amyloid beta aggregation has received considerable attention and several different approaches can be distinguished. On the one hand, the fitting of 'simple' mathematical models to *in vitro* data of protein aggregation has resulted in a series of high-level descriptions of the process. Examples include the model by Lomakin et al. from 1996, the model by Pallitto and Murphy in 2001 and finally the minimal model by Finke and Watzky in 2008. These models are discussed below. On the other hand, 'coarse-grained' models of protein aggregation have evolved which describe the process at an atomic level with the aim to predict the three-dimensional shape and size of aggregates. One example of these models is the one by Auer et al. (2008). While this class of models offers valuable insights into the mechanistic regulation of protein aggregation, it requires very precise data currently not available from *in vivo* studies and therefore cannot serve as a blueprint to model protein aggregation using the data available for the work presented here. Besides these two distinct approaches to the mathematical description of protein aggregation based on *in vitro* time series data, a third

route has been taken which uses experimentally determined rate constants to describe *in vivo* aggregation of Aβ. A main representative of this route is the model by Craft et al. (2002). In their work, as described below, the authors analyse the effect of several disease-modifying treatments on Aβ42 concentration in the brain, the cerebrospinal fluid (CSF) and plasma.

4.1. Lomakin 1996 – Protein aggregation by nucleation and subsequent monomer addition

In the realm of Aβ aggregation, one of the first kinetic models has been proposed by Lomakin et al. (1996). This model is based on aggregation experiments with synthetic Aβ40 observed by quasi-elastic light-scattering spectroscopy and modelled aggregation as the reversible self-association of monomers (C in the notation used by the authors,) to form so-called micelles. These micelles initiate the first of two subsequent steps: formation of nuclei from micelles (rate constant k_n, ratio 1:1) and elongation by monomer addition (rate constant k_e):

$$C \leftrightarrow \text{Micelles}$$
$$\text{Micelles} \xrightarrow{k_n} N$$
$$C + N \xrightarrow{k_e} F$$

The parameter values are given as $1.1 \times 10^{-6} \cdot \text{sec}^{-1}$ for k_n and $65\text{M}^{-1} \cdot \text{sec}^{-1}$ for k_e. The number of monomers per micelle, and therefore the number of monomers per nucleus, is suggested to be between 15 and 70. The authors suggest that a threshold c^* for the initial concentration of monomers exists, below which no micelles are formed and nucleation is initiated predominantly by non-Aβ seeds. Above this concentration, the reversible formation of micelles results in an almost constant concentration of monomers. In this domain ($C_0 > c^*$), the initial elongation rate is given by $k_e \cdot c^*$ and is independent of the initial Aβ concentration. Using their model of nucleation and subsequent monomer addition, Lomakin et al. discuss the effect of influencing the rate of nucleation k_n and the rate of elongation k_e on the resulting amount and length of fibrils. Given a fixed initial amount of monomers above the critical concentration necessary to form micelles, an increased rate of nucleation would lead to higher numbers of fibrils with a comparably shorter length. An increased rate of elongation instead would result in fewer but longer fibrils. The authors argue that this behaviour might be behind the observation that several compounds have been reported to both "inhibit" and "promote" fibril formation and that the concepts of "inhibition" and "promotion" might be "inadequate and misleading descriptors of the effect of external agents on fibrillogenesis" (Lomakin et al., 1996). Instead, the study

of protein aggregation should focus on the two steps of nucleation and elongation. The observation of a critical monomer concentration c^* which is necessary for homogeneous aggregation to start is also suggested to be the reason for the absence of aggregates in the plasma and CSF, where the concentration of Aβ is very low.

4.2. Pallitto and Murphy 2001 – Negligible importance of reversibility over long time spans

In 2001, Pallitto and Murphy presented a detailed kinetic model of the aggregation of Aβ (Pallitto and Murphy, 2001). This model considers an aggregation pathway which consists of four different steps: Refolding of naturally unfolded monomers, filament initiation by nucleation, filament elongation by monomer addition and end-to-end association of filaments and finally fibril formation by filament lateral aggregation and end-to-end association of fibrils. The model distinguishes between the irreversible formation of stable

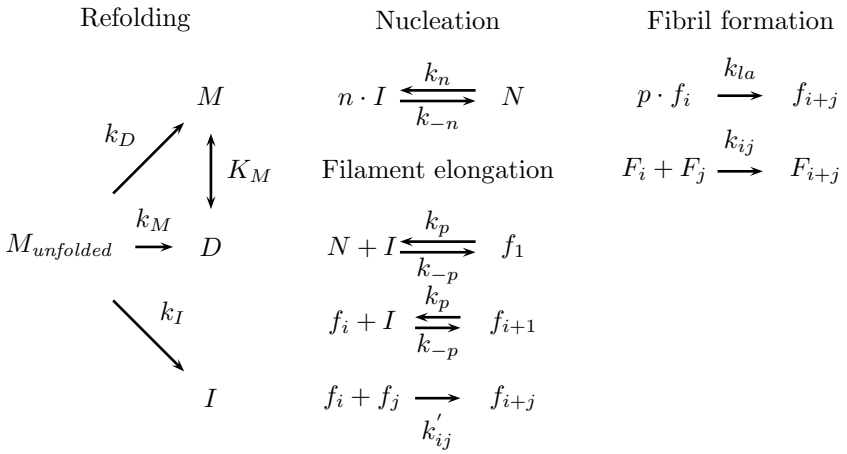

Figure 4.1.: Refolding and aggregation steps considered by Pallitto and Murphy (2001).

folded monomers (M, rate constant k_M) and dimers (D, rate constant k_D) which do not take part in the association pathway and the formation of unstable intermediates (I, rate constant k_I) which follow the proposed aggregation pathway. Filament initiation by nucleation and filament elongation by monomer addition are considered reversible processes (rate constants k_n, k_{-n} and k_p, k_{-p}, respectively), while end-to-end association of filaments and fibrils (rate constant k'_{ij} and k_{ij}) as well as filament lateral aggregation (rate constant k_{la}) are considered irreversible (Fig. 4.1). To determine meaningful values for the model parameters, the authors use experimental data of Aβ40 aggregation from size exclusion chromatography, dynamic light scattering and static light scattering.

For the first step, the initial refolding of the denatured protein into either stable monomers, dimers or unstable intermediates, a rapid process is assumed so that the initial concentrations of M, D and I can be calculated using a steady state expression. Aggregation of the unstable intermediates I to the initial filament (N, i.e. the nucleus) as well as the further aggregation steps are modelled as a time dependent dynamic process using ordinary differential equations. The model does not explicitly state the size of the largest aggregate, instead the authors employ a mathematical trick by introducing moments for the filament size distribution and fibril size distribution, thereby reducing the size of the system from ∞ to six. In addition to real-valued parameters for the rate constants for the formation of stable monomers (k_M), formation of stable dimers (k_D), formation of unstable intermediates (k_I), nucleation (k_n), monomer addition (k_p) and filament lateral aggregation (k_{la}) the authors also estimate three integer parameters. From these parameters, the first one, nucleus size (n) is fixed to calculate the best-fit value for k_n/k_p. The remaining two parameters, the number of filaments participating in fibril formation (p) and the reaction order for filament to fibril association (q) are estimated by fixing them "arbitrarily to different integer values between 2 and 6, based on reports that fibrils contain three to six subunits" (Pallitto and Murphy, 2001) and then fitting the remaining kinetic rate constants.

Interestingly, the rate constants for nucleus breakup (k_{-n}) and fibril breakup (k_{-p} "were kept close to zero", assuming that "filament initiation and elongation are irreversible" (Pallitto and Murphy, 2001). The authors specifically state, that "no unique values for these reverse rate constants could be ascertained from the data" (Pallitto and Murphy, 2001). This suggests, that for studies which model the time evolution of protein aggregates over more than a few hours, reversibility may be insignificant compared to the nucleation and aggregation steps.

4.3. Morris 2008 – A minimal "Ockhams' Razor" model of protein aggregation

In 2008, Morris et al. showed that a large majority of the published data of protein aggregation can be fitted using a "2-step Minimal/Ockhams' Razor model"(Morris et al., 2008), which they name the "Finke-Watzky mechanism of nucleation followed by autocatalytic surface growth":

$$\begin{aligned} \mathrm{A} &\xrightarrow{k_1} \mathrm{B} \\ \mathrm{A} + \mathrm{B} &\xrightarrow{k_2} 2\mathrm{B} \end{aligned}$$

In this mechanism, the initial, typically slow, nucleation step (rate constant k_1) is followed by a fast autocatalytic growth step (rate constant k_2). This mechanism is a special case

of the 'generalized form of the Finke-Watzky mechanism':

$$\begin{aligned} n\mathrm{A} &\xrightarrow{k_1'} \mathrm{B}_n \\ \mathrm{A} + \mathrm{B}_n &\xrightarrow{k_2'} \mathrm{B}_{n+1} \end{aligned}$$

In the publication, the authors show the application of their mechanism to aggregation data of α-synuclein, polyglutamine, β2-microglobulin and several datasets of amyloid beta. The authors also provide the rate law for the time evolution of the concentration of A

$$\frac{\mathrm{d}[\mathrm{A}]}{\mathrm{d}t} = k_1[\mathrm{A}] + k_2[\mathrm{A}][\mathrm{B}]$$

as well as the analytical solution for both $[\mathrm{A}]_t$ and $[\mathrm{B}]_t$:

$$\begin{aligned} [\mathrm{A}]_t &= \frac{\frac{k_1}{k_2} + [\mathrm{A}]_0}{1 + \frac{k_1}{k_2[\mathrm{A}]_0} \exp\left(k_1 + k_2[\mathrm{A}]_0\right) t} \\ [B]_t &= [\mathrm{A}]_0 - \frac{\frac{k_1}{k_2} + [\mathrm{A}]_0}{1 + \frac{k_1}{k_2[\mathrm{A}]_0} \exp\left(k_1 + k_2[\mathrm{A}]_0\right) t} \end{aligned}$$

for systems with mass balance $[\mathrm{A}]_t = [\mathrm{A}]_0 - [\mathrm{B}]_t$.

The resulting fits of the model parameters to the amyloid beta datasets resulted in parameter values ranging from $6 \times 10^{-7}\mathrm{h}^{-1}$ to $6 \times 10^{-3}\mathrm{h}^{-1}$ for k_1 and $7 \times 10^{-4}\mathrm{h}^{-1}$ to $3 \times 10^{-1}\mathrm{h}^{-1}$ for k_2 with the resulting fits "in all cases [...] very good if not excellent" (Morris et al., 2008). While Morris et al. highlight the ability of their model to describe a vast array of different protein aggregation data and deconvolute nucleation from growth, they also discuss the limitations of their minimalistic approach. The Finke-Watzky mechanism is a highly simplified, phenomenological model. Species A describes the unfolded protein, while species B is an aggregate of all sizes of aggregates. This makes it impossible to distinguish "hypothesized toxic intermediate species" from "hypothesized nontoxic fibrils". In addition, the two calculated rate constants k_1 for nucleation and k_2 for growth are therefore averages of the true rate constants of the many steps merged into the two steps described by the model.

4.4. Craft 2002 – The importance of transport of Aβ to monitor disease progression

Craft et al. (2002) developed a compartmentalized model of Aβ production, degradation and aggregation. Their aim, motivated by an increasing number of preclinical trials to evaluate the effectiveness of therapeutic inventions in Alzheimer's disease, was to assess

the relation between the clinically easily accessible Aβ levels in plasma and CSF, and the unobservable levels of brain Aβ.

In their model, Aβ42 is produced in the brain at a constant rate (rate constant p_b) and degraded in the brain (rate constant l_b) and the plasma (rate constant (l_p). Transport is considered from the brain towards the CSF (rate constant r_{bc}), from the CSF to the plasma (rate constant r_{cp}) and from the plasma to the brain (rate constant r_{pb}). Aggregation and fragmentation occur only in the brain:

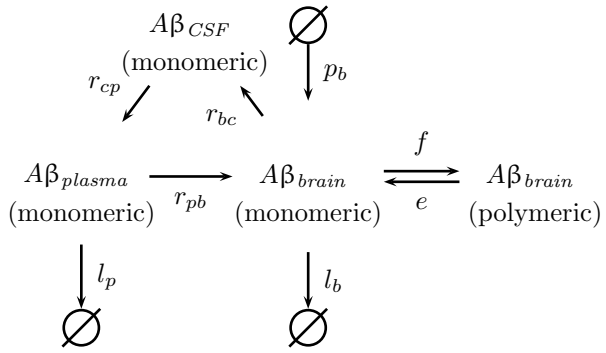

The model consists of an infinite number of ordinary differential equations, which arise from the rate laws for fibril formation by subsequent monomer addition. The parameter values for monomer loss, elongation and transport between the compartments are taken from different experiments with transgenic mice, synthetic fibril analysis, studies in guinea pigs and rats. For the estimation of polymerization rate and production rate data about total Aβ42 level in demented patients, CSF Aβ42 levels and the fraction of brain Aβ that consists of monomers are used. Monomer loss and transport between the compartments is modelled by first order kinetics.

Using a steady state solution of their model, the authors differentiate between two scenarios. In the first scenario (*Subcritical regime*), which is analysed in depth, the concentration of Aβ approaches a steady state in all compartments. In the second scenario (*Supercritical regime*) the amount of Aβ in the brain is constantly increasing while the concentration of monomeric Aβ in the plasma and in the CSF remains constant. The two regimes are distinguished by a unitless quantity which the authors call 'polymerization ratio'. This ratio is defined as the "product of production and elongation rates divided by the product of the fragmentation and loss rates" (Craft et al., 2002). In the subcritical regime, changes in the production rate (e.g. due to modifications in the APP cleaving secretases), enhanced fragmentation (e.g. after administration of a fragmentation enhancer) and increased monomer loss (e.g. after Aβ vaccination) lead to a simultaneous decrease in the levels of CSF Aβ, plasma Aβ and brain Aβ. The authors speculate that the subcritical regime is the clinically relevant one and conclude, that CSF and plasma levels can be

used as biomarkers to assess the effectiveness of therapeutic interventions which effect production, degradation or fragmentation rates.

4.5. Comparison of the available models

Despite the different approaches applied to model protein aggregation in the models presented above, there are several aspects which are shared. All models use ordinary differential equations to describe the dynamical process of aggregation. In addition, all models differentiate between at least two different aggregation steps, which are modelled using different rate constants.

The models by Lomakin et al. (1996); Morris et al. (2008) and Pallitto and Murphy (2001) are compared to time series data of *in vitro* aggregation data. The only model that explicitly describes the *in vivo* situation uses no experimental data for comparison (Craft et al., 2002). This model is also the only model that explicitly considers transport of Aβ between different compartments.

All models agree in the inclusion of a nucleation step and at least a single aggregation step. In three of the models, further aggregation is included, either by monomer addition (Lomakin et al., 1996; Morris et al., 2008) or by end-to-end aggregation of larger aggregates (Pallitto and Murphy, 2001). The most general model is the "Finke-Watzky" model by Morris et al. (2008).

The mandatory initial refolding step has only been considered in two model based on *in vitro* data (Lomakin et al., 1996; Pallitto and Murphy, 2001). These models cover the time frame of several hours. This time frame is much smaller than the time over which that data described in Chapter 3 has been measured.

5. Building an *in silico* model of *in vivo* protein aggregation

5.1. Assumptions made in the construction of the model

Every modelling project relies on a set of assumptions, that leads to decisions shaping the final model. In addition to the choice of an appropriate modelling formalism, decisions about the inclusion or omittance of every process that might have an influence of the system under consideration have to be made.

Owing to the multitude of mechanisms involved in the *in vivo* aggregation of Aβ, some of which almost certainly remain unknown, I did not attempt a detailed mechanistic mathematical representation. Instead I concentrated on distilling the available knowledge into a model that illuminates the underlying dynamics and provides explanations for the experimental observations in ABC transporter-deficient mice. The phenotypic changes in the different transgenic mice that were employed are the result of a complicated interplay between protein aggregation and aggregate removal processes.

In the following paragraphs, the set of assumptions made in the development of the model are discussed. These assumption deal with the choice of a suitable model formalism, the scope of the model, and the importance of the different factors influencing the aggregation and removal processes.

The case for ODEs to model protein aggregation

When deciding on a modelling paradigm to use for a particular project, the decision is often guided by several factors. For protein aggregation, the assumption that aggregation dynamics depends on the concentration of the available species under consideration can be interpreted as an application of the law of mass action. This law, established more than 150 years ago (Voit et al., 2015), states that under ideal conditions the speed of an reaction depends on the product of its substrates and a rate constant, the latter often denoted by k.

While the assumption of "ideal conditions" can be debated, the law of mass action is currently the prevailing mechanism in quantitative models of biochemistry (Le Novère, 2015). The derivation of the law of mass action is based on several assumptions: a well stirred medium (more precisely: and ideal gas), constant temperature and constant pressure, and detailed information about these conditions is required. Unfortunately, for the modelling project at hand, these data are not available. Information about the spatial distribution of amyloid beta is lost as the samples have been homogenized. Variations in temperature and pressure have not been measured.

The law of mass action has it's mathematical counterpart in ordinary differential equations (ODEs). These equations relate the rate of change of a quantity to the value of the quantity or, biologically speaking, the rate of change of a species is a function of it's amount.

Besides this more theoretical consideration there is also a practical reason to choose ODEs as modelling paradigm. The available experimental data consist of time series measurements of relative concentrations, i.e. the data describes a dynamical process that occurs over time. Ordinary differential equations which describe the rate of change in the concentrations with respect to time, are therefore an obvious choice.

Based on these observations together with the fact that the use of ordinary differential equations is a common feature of the models discussed in Chapter 4, this mechanism was chosen to model *in vivo* protein aggregation in mice.

The decision which species to include — and which to leave out

Protein aggregation is a complex process which consists of several sequential steps. Following the description in Chapter 2 one can distinguish at least the following six different quantities: monomeric Aβ, nuclei (seeds), oligomers, protofibrils, fibrils and plaques. With the exception of monomers, each of these quantities is the result of a multi step aggregation process and can contain aggregates of variable size. To complicate the situation even further, there is no clear cutoff between the different types of aggregates with respect to the number of monomers they consist of. To decide which species to consider in the model additional information needs to be taken into account.

Based on the data which has been measured in mice I assume that monomeric Aβ is constantly produced during lifetime, may therefore make up at least part of the measured Aβ load, and needs to be considered in the model. From the history of mathematical models of protein aggregation I take that nucleation is a decisive factor in the aggregation process. Consequently nuclei, formed from monomeric Aβ, acting as seeds for the larger aggregates, are explicitly considered in the model. Following the conclusion from Chapter

4, I assume that larger aggregates are formed by monomer addition to the initial nucleus. Given the assumed constant production of monomeric Aβ, there is theoretically no upper limit for the size of an individual aggregate in the model. To guarantee a finite number of differential equations, however, I have to introduce a limit for the number of species considered in the model. This limit, i.e. the number of monomers considered in the largest aggregate, is in the following denoted by n_i.

Contrary to the classification given above, I do not divide the different sized aggregates into oligomers, protofibrils, fibrils and plaques. Instead, I distinguish between two groups of aggregates larger than the nucleus. The first group contains all aggregates which contain up to n_s monomers and forms together with the monomers and the nuclei the pool of solube Aβ. The second group contains all aggregates which contain more than n_s monomers up to the largest aggregate considered in the model. The distinction between these two pools of Aβ allows a direct mapping of the quantities considered in the model to the experimentally determined Aβ load. Figure 5.1 illustrates the assumed aggregation mechanisms and the species considered in the model.

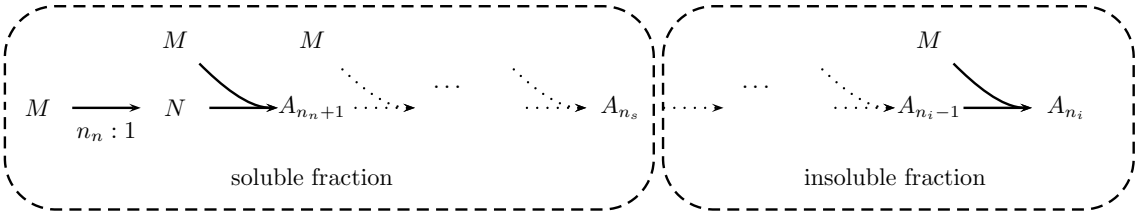

Figure 5.1.: Overview of the different aggregates considered in the model. Shown are monomers (M), nuclei (N) and aggregates of size n_n+1 (A_{n_n+1}), n_s (A_{n_s}) and n_i (A_{n_i}). Aggregation occurs by initial nucleation of n_n monomers into a nucleus and subsequent monomer addition.

Assumptions regarding the production, degradation and transport of Aβ

In addition to the choice of ODEs as modelling formalism, and the decision which quantities to consider in the model, I made the following assumptions:

1. *Monomeric Aβ is produced at a constant rate.* Our experimental data show constant APP expression by the transgene. I therefore assume constant monomer production in our transgenic model. This assumption has been used previously by Craft et al. (Craft et al., 2002).

2. *The first step in Aβ aggregation is the formation of nuclei of a fixed number of monomers.* Nucleation is known to be an important first step in the aggregation of proteins and is a feature of all *in vitro* models of Aβ aggregation discussed in

Chapter 4.

3. *Aβ aggregation occurs by monomer addition to the nuclei.* Sequential monomer addition is included in many models of protein aggregation and has been used to fit several sources of experimental data.

4. *Monomeric Aβ removal from the brain is mediated by ABC transporters.* This assumption is the main motivation for my model. There is increasing evidence of the implication of ABC transporters in the trafficking of Aβ (Krohn et al., 2011; Kuhnke et al., 2007). I refrain from assuming a particular mode of transport as there is most likely not a single transport mechanism which can be attributed to all ABC transporters known to influence Aβ abundance in the brain (See Section 2.2).

5. *Knockout of Aβ-excreting ABC transporters permanently decreases Aβ removal by active molecular transporters.* This assumption is a direct consequence of assumption 4. Other mechanisms that clear Aβ from the brain, such as enzymatic cleavage and proteasomal degradation, are not effected by the ABC transporter knockouts.

6. *Removal of monomeric Aβ by ABC transporters is hampered by Aβ aggregates.* There is ample evidence that increased levels of Aβ critically alter clearance rates from the brain (Zlokovic, 2008). While the exact relation is still unclear, I assume a causal connection to larger Aβ aggregates which might block the access to the transporters. Following this assumption the clearance of Aβ in my model is hampered by the insoluble Aβ fraction.

7. *Aggregation occurs at different rates.* To reduce the reaction networks complexity, two groups of aggregates are considered according to the available experimental data: 'soluble' (i.e. buffer-soluble Aβ) and 'insoluble' (i.e. guanidine-soluble Aβ). I assume that all aggregates in one group are formed with the same aggregation constant: k_{sol} for the soluble fraction and k_{insol} for the insoluble fraction. An additional rate constant is considered for the formation of nuclei (k_{nuc}).

5.2. Translation of the assumptions into a mathematical model

The assumptions were translated into a system of algebraic and ordinary differential equations that describe the temporal evolution of aggregate concentrations as a function of the aggregation and transport processes.

The constant production of Aβ monomers minus the removal via the ABC transporter mediated clearance results in the net inflow I_{net}.

The negative influence of insoluble aggregates is modelled as

$$\frac{s_T^{e_T}}{s_T^{e_T} + L^{e_T}} \tag{5.1}$$

with the two shape parameters s_T and e_T. This term guarantees that for small values of L ($L \ll s_T^{e_T}$), the transport is nearly unaffected by L, whereas for increasing values of L the transport is reduced. This choice presents a general and simple description of a broad range of possible mechanism leading to the reduction for monomeric Aβ transport. The full equation of I_{net} is accordingly:

$$I_{net} = p - (c_T \cdot M) \cdot \frac{s_T^{e_T}}{s_T^{e_T} + L^{e_T}} \tag{5.2}$$

In order to reduce the complexity of the model, all transport mechanisms are merged into the transport capacity c_T.

Monomeric Aβ forms nuclei. The first step in Aβ aggregation is the formation of nuclei consisting of n_n monomers. The reaction rate for the production of nuclei depends on the nucleation constant k_n and monomer concentration M. According to the law of mass action, the rate for monomer decrease is: $-k_n \cdot n_n \cdot M^{n_n}$ while the concentration of nuclei is increased at rate $k_n \cdot M^{n_n}$.

Aβ aggregation occurs by subsequent monomer addition to the nuclei: Each aggregate A_j of size j is formed by addition of one monomer to one aggregate of size $j-1$. Depending on the pool an aggregate belongs to, the aggregation rate is computed as either $k_{sol} \cdot A_j \cdot M$ or $k_{insol} \cdot A_j \cdot M$. A_j is used to identify both the species and the concentration of that species.

Equations of the model

Following the description in the previous paragraphs, the temporal changes in the concentration of monomers, nuclei (N) and all other aggregates (A_{n_n+1} to A_{n_i}) are described by the equations given in Table 5.1:

Table 5.1.: Equations for the time evolution of monomers, nuclei and aggregates of different size in the model

$\frac{\mathrm{d}M}{\mathrm{d}t} =$	$I_{net} - k_n \cdot n_n \cdot M^{n_n}$ - $k_{sol} \cdot N \cdot M$	Net inflow minus decrease by nucleation decrease by monomer addition to nucleus

	- $k_{sol} \cdot A_{n_n+1} \cdot M$	decrease by monomer addition to an aggregate of size $n_n - 1$
	- $k_{sol} \cdot A_{n_n+2} \cdot M$	decrease by monomer addition to an aggregate of size $n_n + 2$
	$\vdots$	
	- $k_{sol} \cdot A_{n_s-1} \cdot M$	decrease by monomer addition to an aggregate of size $n_s - 1$
	- $k_{insol} \cdot A_{n_s} \cdot M$	decrease by monomer addition to an aggregate of size n_s
	$\vdots$	
	- $k_{insol} \cdot A_{n_i-1} \cdot M$	decrease by monomer addition to an aggregate of size $n_i - 1$
$\frac{\mathrm{d}N}{\mathrm{d}t} =$	$k_n \cdot M^{n_n} - k_{sol} \cdot N \cdot M$	Nuclei produced by monomer nucleation minus nuclei converted to larger aggregates by monomer addition
$\frac{\mathrm{d}A_{n_n+1}}{\mathrm{d}t} =$	$k_{sol} \cdot N \cdot M - k_{sol} \cdot A_{n_n+1} \cdot M$	Aggregates of size $n_n + 1$ produced by monomer addition to nuclei minus aggregates converted to larger aggregates by monomer addition
$\frac{\mathrm{d}A_j}{\mathrm{d}t} =$	$k_{sol} \cdot A_{j-1} \cdot M - k_{sol} \cdot A_j \cdot M$ $j = n_n + 2, \ldots, n_s - 1$	Aggregates of size j produced by monomer addition to aggregates of size $j-1$ minus aggregates of size j converted to larger aggregates by monomer addition
$\frac{\mathrm{d}A_{n_s}}{\mathrm{d}t} =$	$k_{sol} \cdot A_{n_s-1} \cdot M - k_{insol} \cdot A_{n_s} \cdot M$	Aggregates of size n_s produced by monomer addition to aggregates of size $n_s - 1$ minus aggregates of size j converted to larger aggregates by monomer addition
$\frac{\mathrm{d}A_j}{\mathrm{d}t} =$	$k_{insol} \cdot A_{j-1} \cdot M - k_{insol} \cdot A_j \cdot M$ $j = n_s + 1, \ldots, n_i - 1$	Aggregates of size j produced by monomer addition to aggregates of size $j-1$ minus aggregates of size j converted to larger aggregates by monomer addition
$\frac{\mathrm{d}A_{n_i}}{\mathrm{d}t} =$	$k_{insol} \cdot A_{n_i-1} \cdot M$	Aggregates of size n_i produced by monomer addition to aggregates of size $n_i - 1$.

The model contains ten parameters, three integer-valued and seven real-valued, which are listed in Table 5.2.

Table 5.2.: Parameters of the model

Parameter	Interpretation
$k_n \in \mathbb{R}^+$	rate constant for nucleation
$k_{sol} \in \mathbb{R}^+$	rate constant for aggregation in the soluble fraction
$k_{insol} \in \mathbb{R}^+$	rate constant for the aggregation in the insoluble fraction
$p \in \mathbb{R}^+$	production rate of monomeric Aβ
$c_T \in \mathbb{R}^+$	maximal capacity for Aβ removal
$s_T \in \mathbb{R}^+$	shape parameter for transport mechanism
$e_T \in \mathbb{R}^+$	shape parameter for transport mechanism
$n_n \in \mathbb{N}^+$	number of monomers inside the nucleus
$n_s \in \mathbb{N}^+$	number of monomers in the largest aggregate in pool of soluble aggregates
$n_i \in \mathbb{N}^+$	number of monomers in the largest aggregate in pool of insoluble aggregates

5.3. Implementation of the model and determination of parameter values

To solve a set of ordinary differential equations and thereby simulate the model the values of all its parameters need to be known. In absence of experimentally determined values, parameter values can be estimated based on the comparison of a model's simulation with experimental data. There exist several global optimization algorithms which promise to find the best fitting set of parameters.

For a model which has both real-valued (i.e. continuous) and integer-valued (i.e. discrete) parameters, at least two different approaches can be taken. The first approach is the application of a mixed-integer nonlinear programming (MINLP) algorithm, which simultaneously determines candidates for the full set of parameters (Bussieck and Pruessner, 2003). The second approach is to limit the application of optimization algorithms to the set of continuous parameters only. In this work I used the second approach: The values of the three discrete parameters were fixed to meaningful values and the set of continuous parameters was determined by global optimization. This decision is based on the following consideration:

The 'correct' value of the parameters cannot be determined from the available data. The experimental data available distinguishes only two types of Aβ. Not only is there no distinction between the different size of aggregates which can be observed *in vitro*, also the line between the two pools of Aβ reported is blurry. Given the fact that even much more sophisticated approaches to determine the rate constants and the size distribution of Aβ aggregates arrive at inconclusive results, it is highly unlikely to extract 'correct' parameter values from the data available for this project.

The 'true' values of the parameters are not required for the model to fulfil its purpose. The purpose of the model is to deliver a phenomenological description of the process of Aβ aggregation and Aβ removal from the brain. The high-level descriptions of aggregation and transport abstract from the underlying biophysical aspects. The significance of the model lies therefore in its ability to reproduce the observed data using a clearly defined set of assumptions. For this purpose, it does not depend on the actual parameter values.

Choice of values for discrete parameters

The value of n_n, the number of monomers per nucleus was set to six. This value is in line with the value chosen in (Pallitto and Murphy, 2001). Further evidence for this value can be taken from the analysis by Bernstein et al., who report hexamer paranuclei for Aβ42 (Bernstein et al., 2009).

The value of n_i, the largest aggregate considered in the model was set to 55. This choice was guided by the aim to keep the number of differential equations low enough to guarantee rapid simulation time. One the other hand, the number should be high enough to mimic the multi-step nature of the aggregation process.

The value of n_s, the number of monomers in the largest aggregate belonging to the insoluble pool, was set to 15. This value guarantees that there is a reasonable amount of aggregates belonging to the soluble pool while keeping the majority of aggregates in the insoluble pool.

While these value are not meant as reasonable estimates of the true values of the parameters, they provide sufficient boundaries for the estimation of the values of the continuous parameters.

Comparison of model simulation with experimental data

The experimental data consist of measurements at six points in time for both soluble Aβ42 and insoluble Aβ42 (See Chapter 3). To compare the output of a model simulation with

Table 5.3.: Transformed species and parameters

$M' = M \cdot X$	concentration of monomers in ng/mg
$N' = N \cdot X$	concentration of nuclei in ng/mg
$A'_j = A_j \cdot X$	concentration of different aggregates in ng/mg ($j = n_n + 1, \ldots, n_i$)
$k'_n = k_n \cdot X^{-n_n+1}$	rate constant for nucleation
$k'_{sol} = k_{sol} \cdot X^{-1} \in \mathbb{R}^+$	rate constant for aggregation in the soluble fraction
$k'_{insol} = k_{insol} \cdot X^{-1}$	rate constant for the aggregation in the insoluble fraction
$p' = p \cdot X$	production rate of monomeric Aβ
$s'_T = s_T \cdot X$	shape parameter for transport mechanism

the data, at least one model constituent needs to be mapped to the data. In the initial formulation, the variables (species) are given in units of aggregate numbers normalized to total protein mass. To compare the model simulations with the experimental data, given in Aβ mass per total protein mass (ng/mg), I transformed the variables of the model such that the new variables have the unit ng/mg. The mass of an Aβ monomer is $\sim X = 4$kDA, which is about $6.642 \cdot 10^{-12}$ ng. Each equation in Table 5.1 was multiplied by X. I then introduced new variables M', N', A'_j and new parameters as follows: Each variable value is proportional to the number of the respective aggregate though the new variables have the unit ng/mg. The concentration of monomeric Aβ included in each aggregate was calculated by multiplying the concentration of the aggregate in terms of the new variables with the number of monomers the aggregate is composed of. In a second step, the simulated concentration of monomers in the pool of soluble Aβ ($\widehat{A\beta}_{sol}$) and the simulated concentration of monomers in the pool of insoluble Aβ ($\widehat{A\beta}_{insol}$) were computed as the sum of monomer concentrations in all aggregates belonging to the respective pool:

$$\widehat{A\beta}_{sol} = M + n_n \cdot N + \sum_{j=n_n+1}^{n_s} j \cdot A_j$$

$$\widehat{A\beta}_{insol} = \sum_{j=n_s+1}^{n_i} j \cdot A_j$$

This procedure results in two quantities which can be compared to the measured data of soluble and insoluble Aβ respectively.

Estimation of values for continuous parameters

To find a set of parameters p which allows the model to fit the experimental data, I used global optimization with the following cost function:

$$f(p) = \sum_{t=1}^{6} \frac{\left(\sqrt{A\beta_{sol}(t_i) - \widehat{A\beta}_{sol}(t_i, p)}\right)^2}{\left(\frac{|lb(t_i) - ub(t_i)|}{\max_i |lb(t_i) - ub(t_i)|}\right)} \tag{5.3}$$

with $A\beta_{sol}(t_i)$ the measured value of soluble Aβ at time point i, $\widehat{A\beta}_{sol}(t_i, p)$ the simulated value of soluble Aβ at time point i given the parameter set p, $lb(t_i)$ the lower bound of the error bar at time point t_i and $ub(t_i)$ the upper bound of the error bar at time point t_i. The lower and upper bounds of the error bars were calculated using the assumption of lognormal data for the 68.3% confidence interval (Limpert et al., 2001):

$$lb(x) = \frac{\bar{\mu^*}}{s^*},\ ub(x) = \bar{\mu^*} \cdot s^*$$

with $\bar{\mu^*}$ and s^* being the maximum likelihood estimators for mean and standard deviation.

$$\bar{\mu^*} = \sqrt{\prod_{i=1}^{n} A\beta_i(t_i)}$$

$$s^* = \exp\left(\left(\frac{1}{n-1}\sum_{i=1}^{n}\left(\log\left(\frac{A\beta_i(t_i)}{\bar{\mu^*}}\right)\right)^2\right)^{\frac{1}{2}}\right)$$

The inclusion of the confidence intervals in Equation 5.3 guarantees that any deviation from the expected value will be weighted by the dispersion of the measurements at the respective time point. This is necessary as otherwise only absolute deviations would be considered which may can be problematic for experimental data covering several orders of magnitude.

I decided to use only the soluble pool of Aβ for the calculation of the cost function to assess, whether the model was able to predict the time course of the insoluble Aβ fraction given the assumptions discussed above. Optimization was performed using the Matlab implementation of the particle swarm optimization algorithm described in (Vaz and Vicente, 2007). All options of the optimization algorithms were kept at their default values, with the exception of `Size` which was set to 300, `MaxIter` which was set to 100 and `MaxObj` which was set to 100 000. The particle swarm algorithm was chosen because of its availability as Matlab code and the good results I had achieved using it for my diplom thesis. Initial values for all estimated values were randomly drawn using the *rand*

function from Matlab. Lower and upper bounds for the parameters which were initially set to $1e-6$ and $1e06$, respectively. After several runs of the optimization algorithm they were refined to cover a smaller search space which covered the resulting parameter sets from the previous runs. These boundaries are listed in Table 5.4.

To account for the stochastic nature of the algorithm the estimation process was repeated 300 times and the parameter set which resulted in the smallest value of the cost function was chosen for further analysis. Initially, parameter value estimation was performed only

Table 5.4.: Bounds for the estimation of parameter values and initial conditions and value for best fit. X is the mass of an Aβ monomer.

Parameter	lower bound	upper bound	value for best fit	unit
k'_n	0	1.5	0.3451	$t^{-1} \cdot \left(\frac{X}{mg}\right)^{-n_n+1}$
k'_{sol}	0	0.5	0.3424	$t^{-1} \cdot \left(\frac{X}{mg}\right)^{-1}$
k'_{insol}	0	1.5	0.3586	$t^{-1} \cdot \left(\frac{X}{mg}\right)^{-1}$
p'	50	200	91.239	$t^{-1} \cdot \frac{X}{mg}$
c_T	0	100	82.419	t^{-1}
s'_T	1	100	17.744	$\frac{X}{mg}$
e_T	1	10	7.8115	
$M'(t=50)$	1	15	1.0439	$\frac{X}{mg}$

for the dataset of ABCC1-deficient mice. The parameter set for which the smallest value of the cost function was computed is given in Table 5.4 and the resulting model simulation is shown in Figure 6.1.

6. Results and discussion

6.1. Simulation results for ABCC1-deficient mice

The model simulation shows excellent agreement with the experimental data of soluble Aβ42 in ABCC1-deficient mice. For all six points of data, the simulated amount of soluble Aβ is inside the error bar and close to the calculated mean. For the data of insoluble Aβ42,

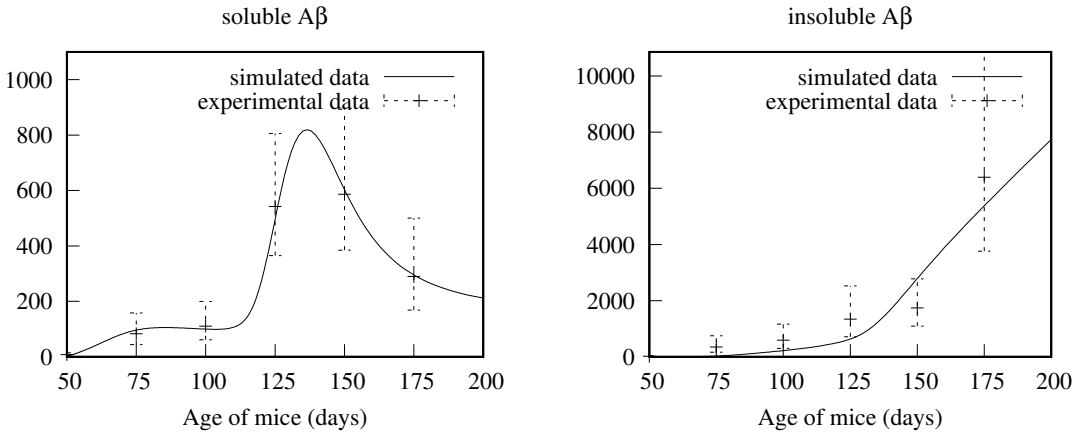

Figure 6.1.: Simulation result for best fitting parameter set for ABCC1 data.

which was not used for the parameter calibration and is predicted by the model, a good agreement is achieved. According to this result, the newly developed model is able to capture the dynamics of the given dataset of protein aggregation in mice.

Given this excellent agreement between the simulated curve and the measured data, it is worthwhile to have a look at the estimated values and see how they relate to experimental findings.

- *The increase in insoluble Aβ results in a switch-like regulation of the net inflow.* The two shape parameters estimated for the negative influence of larger aggregates indicate that already at an amount of 17.744 ng/mg of insoluble Aβ only half of the initial transporter capacity is left. The value of 7.811 for the exponent used in the

description of the regulation of the transport process leads to a switch-like response on the increase in insoluble Aβ42 (See Figure 6.2).

- *Fully active transporters remove the majority of monomeric Aβ from the brain.* The constant production rate of monomeric Aβ has been estimated to be 91.239 $t^{-1} \cdot \frac{X}{mg}$. This is only slightly larger than the estimated capacity of the transport mechanism considered in the model (82.419 t^{-1}).

- *Nucleation, aggregation in the pool of soluble Aβ and aggregation in the pool of insoluble Aβ occur at similar rates.* With values of $k'_n = 0.345$, $k'_{sol} = 0.342$ and $k'_{insol} = 0.358$ for the rates of nucleation, aggregation in the soluble pool and aggregation in the insolube pool, respectively (cf. Tables 5.2 and 5.3), there is no large difference between these rates. This is a contradiction to the finding of slow nucleation and fast growth reported in other modelling studies. However, as the model's simulation starts not at $t = 0$ days, but at $t = 50$ days, the first day for which experimental data is available, a potentially slower nucleation may be occurring already before. As this is not captured by the model, the parameter values should not be taken to argue against the idea that nucleation is usually much slower than the subsequent aggregation steps.

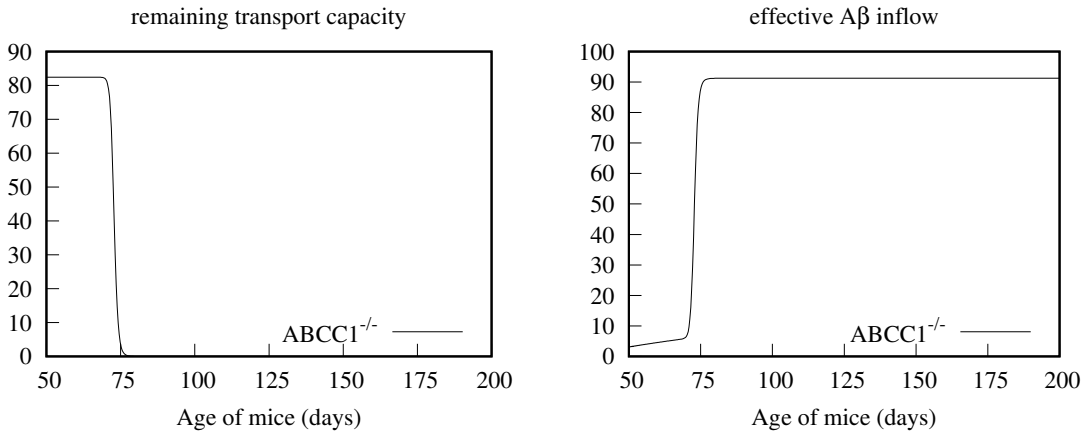

Figure 6.2.: Capacity of transporters, net inflow and concentration of monomers

The switch-like increase of the net inflow of monomeric Aβ is important. It suggests that, while there is constant deposition of soluble and insoluble Aβ from the beginning, at a certain point in time, a drastic change in the regulation of Aβ removal is happening. Compared with the observed peak of the potential neurotoxic pool of soluble Aβ at around day 130 (Fig. 6.1) , the increase of inflow of monomeric Aβ happens already much earlier, at around day 73.

6.2. Modelling the influence of a different transporter knockout

The second application of the model is the prediction of experimental data that has not been used for model calibration. This is done using the Aβ aggregation data from a mouse model lacking a different ABC transporter, namely ABCB1. This mouse model is the second model for which data for modelling was available (See Figure 2.3, Page 17).

Assuming that the new model covers the main mechanisms responsible for Aβ aggregation and that these mechanisms are in principle independent of the way Aβ is removed from the brain, the difference resulting from the knockout of different transporters should be limited to the parameter c_T, the capacity of the modelled transport mechanism. A change in this parameter alone should therefore be enough to describe the time course of Aβ42 aggregation in ABCB1-deficient mice.

To test this hypothesis, I performed a linear parameter search by gradually increasing the value of c_T and simultaneously calculating the best fit according to Equation 5.3, this time comparing the simulated time course with the experimental data obtained for the ABCB1-deficient mice. The resulting best fit, shown in Figure 6.3, shows a very good fit for five out of six measurements for the pool of soluble data, and a good fit for all six measurements in the pool of insoluble data.

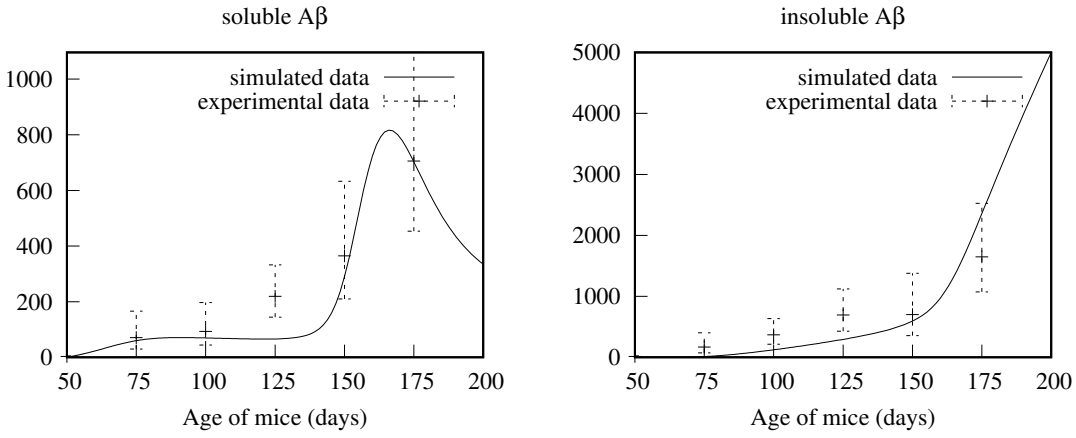

Figure 6.3.: Simulation result for best fitting parameter set for ABCB1 knockout data. Except for c_T, all parameters have the same value as in the model for ABCC1-deficient mice.

The value of c_T for the best fit (c_T^{ABCB1}) is 89.4851, or $1.11 \cdot c_T^{\mathrm{ABCC1}}$. This result suggests that the knockout of ABCB1 decreases the removal of Aβ42 less than the knockout of ABCC1.

The difference in the value of c_T between the model for ABCC1-deficient mice and ABCB1-deficient mice does influence the time course of the remaining transporter capacity and the resulting effective Aβ inflow. Figure 6.4 shows these differences. Interestingly, while there is a distinct difference in the initial transport capacities, the time of the sudden decrease in transporter capacity and increase in Aβ inflow are quite similar. These small

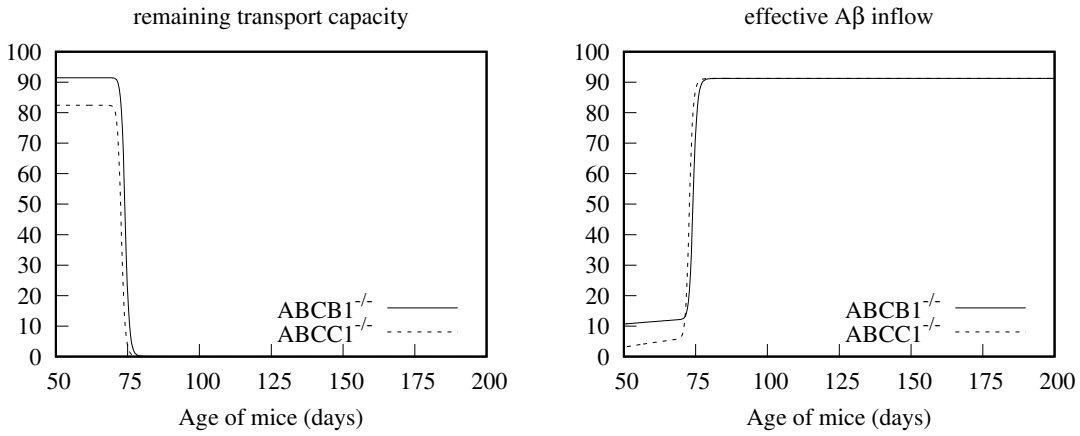

Figure 6.4.: Remaining transporter capacity and effective influx of Aβ for the simulated aggregation profile in ABCB1 and ABCC1-deficient mice.

differences, however, result in the rather larger shift in the peak of soluble Aβ42 captured in the experimental data.

Given the good fit of the model's simulation to two different data sets, the model is not only able to capture the main dynamics of Aβ aggregation in mice, it can be also used to quantify the effect of different transporter knockouts.

6.3. Discussion

The modelling project described in the previous chapters was motivated by two groups of questions:

1. Can the time course data of soluble and insolube Aβ be explained by a mathematical model? Which mechanisms are necessary to model protein aggregation *in vivo*? In other words: 'How' does protein aggregation occur?

2. Can this mathematical model be used to quantify the influence of the missing transporter proteins? In other words 'How big' is the influence of the different transporters.

To answer the first question, I have constructed a phenomenological model of *in vivo* protein aggregation in mice. The model is able to fit the observed time course of soluble Aβ42 aggregates and to predict the time course of insoluble Aβ42 aggregates. To achieve this result, I have included the following mechanistic assumptions:

(I) Protein aggregation occurs by initial nucleation followed by subsequent monomer addition,

(II) ABC transporter mediate the removal of monomeric Aβ,

(III) Breakage of aggregates can be neglected for studies of *in vivo* protein aggregation over long timescales, and

(IV) Larger aggregates impede the removal of Aβ from the brain.

Assumption (I) has been taken from the literature discussed in Chapter 4 and has been previously applied in several other kinetic models of amyloid beta aggregation. It is based on experimental evidence from in vitro studies of protein aggregation. While there is evidence that aggregation itself is not a simple one-way process, this assumption can still be assumed to cover the core mechanism of protein aggregation.

The second assumption (II), is a consequence of the experimental data available for this modelling project. The restriction to transport of only monomeric Aβ42 was a deliberate choice not enforced by the data, but is in line with experimental evidence available in the literature as detailed in Chapter 2.

Assumption (III) was made after the contradicting assumption, that breakage needs to be considered, was discarded. In a previous model I had included a breakage constant which was consistently estimated to be zero over several runs of the parameter estimation routine.

The most interesting assumption is the negative influence of larger Aβ aggregates on the removal of monomeric Aβ (IV). The estimation of the values for parameters which describe this negative influence, s^T and e^T, showed that the observed time course is the result of a sharp decrease in the removal of monomeric Aβ at around $t = 75$ days. In my model this is simply the result of the accumulation of larger aggregates of Aβ42, i.e. all aggregates belonging to the fraction of insoluble Aβ42. While this is, by all measures, a very simplified description and should not be considered the 'true' cause of the sudden increase in the net inflow, it is still a very important finding especially considering the answer to the second research question:

2. Can this mathematical model be used to quantify the influence of the missing transporter proteins? In other words 'How big' is the influence of the different transporters.

As the model is able to closely fit the data for soluble Aβ42 and, in addition, predicts the data for insoluble Aβ42 for both mouse models, it can be assumed that the increase in the net inflow of Aβ is actually a feature of the transport mechanism. Whether the observed increase in the net inflow is really a result of the observed aggregation of insoluble Aβ42 as postulated in the assumptions, cannot be answered by mathematical modelling alone. However, the fact that the sharp increase in Aβ inflow happens before the drastic increase in soluble Aβ indicates that there might be an disease-initiating step already long before the first symptoms become visible.

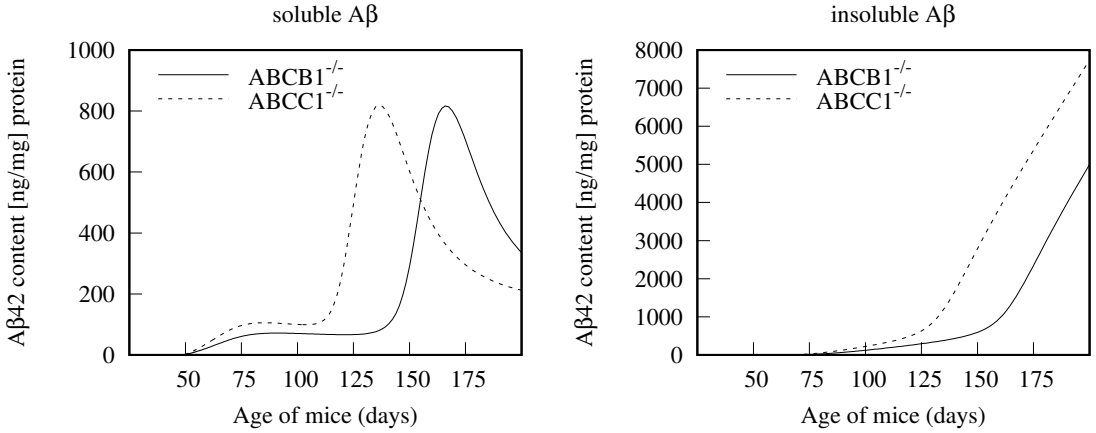

Figure 6.5.: Time course of aggregation for soluble and insoluble Aβ for both mouse models as predicted by the model.

A comparison of the predicted aggregation time course for both mouse models (Figure 6.5) and the calculated effective Aβ inflow (Figure 6.4) highlights the enormous effect a small difference in the onset of increased inflow of Aβ has on the aggregation profile. The neurotoxic soluble fraction in the ABCC1-deficient mice peaks at around 136 days. The same fraction in the ABCB1-deficient mice peaks at around 165 days, a difference of 22 days. The difference between the time when the transport capacity decreases below one is, however, only two days: day 76 for ABCC1 knockout mice and 78 days for ABCB1 knockout mice.

Summing up these results, it is clear that my new models is able to provide answers for both groups of questions that guided this work. There are, however, a few points that can be improved in future modelling projects.

As detailed in Section 2.1 many of the aggregates included in the soluble fraction can be

considered neurotoxic. In the current setup of the model this information is not used. An analysis of the effect of neurotoxicity on the amount of Aβ that is produced might improve the models prediction especially for later point in time.

The data used to calibrate the model was measured in mice lacking specific ABC transporters. While this allowed to analyse the observed decrease in soluble Aβ42 observed in ABCC1$^{-/-}$ mice, an inclusion of data from a control group is desirable. Comparing knockout data with control data would allow quantifying not only the difference between different knockouts, but instead to quantify the effect of each individual transporter. To do so, a more elaborate model of the transport process would be required, as it is very likely that the missing transporters activity can be at least partially replaced by an increased activity of the remaining transporters.

Future work should therefore concentrate on understanding the regulation of ABC transporter mediated removal of Aβ from the brain, and especially the reason for the sudden decrease in transport capacity predicted by the model. Improved understanding of the negative influence of larger aggregates on amyloid beta on the removal of monomers might be a key step towards the development of interventions that keep its production and degradation in balance, and thereby at least delay the onset of cognitive decline.

Part II.

Modelling the brain energy metabolism in humans

7. Predicting the influence of early metabolic alterations on the BOLD shape

7.1. Objective and outline of the work

Changes in brain energy metabolism are an important characteristic of Alzheimer's disease. Decreased glucose metabolism as observed by FDG-PET, for example, is one of the early biomarkers and can precede cognitive decline by several years (Jack Jr et al., 2013). In addition, altered expression of various enzymes involved in different pathways of brain energy metabolism has been observed (Bigl et al., 1996, 1999; Palmer, 1999; Orešič et al., 2011). Region specific changes in the ratios of the different cell types in the brain have also been described in AD patients (Vanzani et al., 2005; Robinson, 2001).

The objective of the present work is to understand how knowledge about these changes can be used to improve the understanding of blood-oxygen-level dependent functional magnetic resonance imaging (BOLD fMRI) data, an important imaging modality in AD. The main tool applied towards this goal is enzyme kinetic modelling of metabolic reaction networks.

I will use the following structure for the next chapters:

The remainder of Chapter 7, starting with Section 7.2, explains the origin of the blood-oxygen-level dependent signal (BOLD signal) used in fMRI, with a focus on the metabolic component of the signal. This section contains the information required to understand the biological background and application of BOLD fMRI. Section 7.3 introduces the hemodynamic response function (HRF), a mathematical description of the physiological response to neuronal stimulation currently used in clinical practice. Chapter 7 concludes with a description of the specific research questions that guide this project and explains its integration into the "VPH DARE@IT" project.

Chapter 8 outlines the main metabolic pathways and reactions of cerebral energy metabolism. It also includes a description of several alterations reported in AD patients relevant for this work. Chapter 9 introduces a selection of mathematical models available in the

literature that describe the networks of brain energy metabolism and the hemodynamic response. In some instances, the models described in Chapter 9 introduced mathematical descriptions of biochemical processes which are also part of the new model developed in the present work. In these cases, the corresponding equations are described in this chapter.

Chapter 10 contains the description of the new kinetic model of brain energy metabolism I have developed. This includes a discussion of the requirements for the model, derived from the research questions (Chapter 7), the biological background (Chapter 8) and the models available from the literature (Chapter 9). Chapter 10 also contains a description of the implementation of the model as part of a Taverna workflow, deployed via the VPH-Share infrastructure. Finally, Chapter 11 shows the application of my model to the analysis of several AD-specific alterations in the brain. This analysis is completed by a discussion of the results of the project with respect to the initial research question. The description of AD-related changes in brain energy metabolism in Chapter 8 as well as large parts of Chapter 10 and Chapter 11 are based on the publication (Winter et al., 2017).

7.2. The BOLD signal: biological background and clinical application

The use of the BOLD signal to detect brain activation is the result of a long history of research. In 1936, Linus Pauling and Charles D. Coryell reported that oxyhemoglobin, i.e. oxygen bound to hemoglobin, contains "no unpaired electrons", whereas hemoglobin (also: deoxyhemoglobin) itself contains "four unpaired electrons per heme" (Pauling and Coryell, 1936). This difference leads to hemoglobin being diamagentic, i.e. it is repelled by an applied magnetic field as opposed to oxygenated hemoglobin (oxyhemoglobin), which is paramagnetic, i.e. it is attracted by an external magnetic field. The first application of the paramagnetic property of deoxyhemoglobin as a tracer for magnetic resonance imaging dates back to 1990. Ogawa et al. (1990) showed that the difference in magnetic susceptibility of the blood, depending on the blood oxygen level, can be used for noninvasive detection of processes which influence this level. In their paper, they analysed the effect of anaesthesia and insulin-induced hypoglycaemia, but already suggested that BOLD fMRI could be used to study regional brain activity (Ogawa et al., 1990). Since then, the importance of BOLD fMRI has continuously increased and it has become a standard tool for clinical brain activity imaging with a wide range of applications (Ulmer and Jansen, 2010). For this project, the relevance of BOLD fMRI lies in its application to monitor brain activation and disease progression in Alzheimer's disease (Kivistö et al., 2014). To understand why brain activation can be measured by BOLD fMRI, it is necessary to recapitulate the origin of the BOLD signal.

As outlined above, the signal observed in BOLD fMRI depends on a change in the ratio of oxyhemoglobin and deoxyhemoglobin. The reason that this ratio changes upon neuronal activation is twofold. First and foremost, neural activity leads to increased cerebral blood flow. Second, but with a special importance for this work, neuronal activity leads to an increased demand of energy, which is supplied by a chain of metabolic pathways, including glycolysis and oxidative phosphorylation. The degree in which the two processes contribute to the supply of energy during and after stimulation and the biochemical processes that govern their interaction, are a matter of ongoing research. However, it is undoubted that oxygen consumption during oxidative phosphorylation increases compared to the resting state (Raichle and Mintun, 2006). It has also been established that the increase in blood flow is more pronounced than the increase in oxygen consumption. This observation has lead to a definition of brain activation generally agreed upon in the imaging community. In short, regional activity in the brain is characterized by an increase in blood flow that is higher than the observed increase in oxygen consumption (Raichle and Mintun, 2006).

To detect an increase in both blood flow and oxygen consumption it is necessary to compare measurements at different time points. The temporal resolution of the measurement depends heavily on the chosen spatial resolution. For example, it takes about 2 seconds to acquire a full brain volume of dimension $64 \times 64 \times 30$ voxels using the currently dominant slicing approach (Lindquist, 2008). While it is possible to decrease the repetition time (TR) by a reduction of the spatial resolution to obtain a higher temporal resolution, a TR value of 2 seconds is generally assumed adequate given the time scale of the BOLD response (cf. Figure 7.1, p59).

Shape of the BOLD response

Friston (2007) describes the typical BOLD response to a "single, impulsive stimulation", shown in Figure 7.1, by its peak "approximately 5 s after stimulation" and the following undershoot "that lasts as long as 30 s". For comparison, it can be characterized by three measures: peak height, peak time, and full width at half maximum (FWHM) (Lindquist et al., 2009). The physiological interpretation of the shape is that the increase in blood flow, which is higher than the increase in oxygen demand, leads to a higher fraction of oxygenated hemoglobin, visible in the increase in the BOLD signal until its peak. After a certain time, the blood flow decreases faster than the blood volume, thereby shifting the ratio towards deoxyhemoglobin which leads to the observed undershoot (Lindquist, 2008). Some authors have also observed an initial dip, i.e. a short decrease in the BOLD signal below its baseline value before the first onset. The usual interpretation of this dip is that oxygen consumption and thereby the fraction of deoxyhemoglobin increases slightly faster

than the blood flow. Overall, the full time course of the BOLD response takes at least 20 to 30 seconds. The BOLD response is thus much slower than the actual neuronal activity, which has a time scale of milliseconds (Lindquist, 2008).

7.3. The canonical hemodynamic response function

The typical BOLD shape as described by Friston (2007) can be assumed to be the hemodynamic response to said "single, impulsive stimulation". To determine whether or not a specific brain region is activated in response to a stimulus, statistical tools are used to compare the measured BOLD response in this particular region with the expected BOLD response. For this comparison, the expected response has to be precisely defined. One attempt to provide a mathematical description of the expected signal is the canonical hemodynamic response function (HRF) shown in Figure 7.1. First used by Glover (1999) to describe the characteristics of the BOLD signal in the sensorimotor and auditory cortices, the function is now a staple in the analysis of functional fMRI data. The function consists of the linear combinations of two gamma functions $\Gamma(\cdot)$. I shall here denote the time-dependent HRF as $\mathrm{hrf}(t)$:

$$\mathrm{hrf}(t) = \frac{\frac{\mathrm{dt}}{p(3)}^{\frac{p(1)}{p(3)}} \cdot t^{\frac{p(1)}{p(3)}-1} \cdot e^{-\frac{\mathrm{dt}}{p(3)}t}}{\Gamma\left(\frac{p(1)}{p(3)}\right)} - \frac{1}{p(5)} \cdot \frac{\frac{\mathrm{dt}}{p(4)}^{\frac{p(2)}{p(4)}} \cdot t^{\frac{p(2)}{p(4)}-1} \cdot e^{-\frac{\mathrm{dt}}{p(4)}t}}{\Gamma\left(\frac{p(2)}{p(4)}\right)} \tag{7.1}$$

The canonical HRF has six parameters of which the first five influence its shape. $p(1)$ and $p(3)$ control the delay and dispersion of the response, respectively. $p(2)$ and $p(4)$ control the delay and dispersion of the undershoot, respectively, and $p(5)$ gives the ratio of onset and undershoot. The last parameter, dt, is determined by the ratio of scan repeat time and time resolution of the experimental protocol. The parameter names given here correspond to the implementation of the canonical HRF in SPM (Statistical Parametric Mapping), a widely used tool for the analysis of fMRI images[1]. There exist other approaches to model the hemodynamic response, but the canonical HRF is the typical choice in clinical routine (Lindquist, 2008). For a detailed overview of different methods see Friston (2007, Chap. 14)

Convolution models for dynamic stimulation patterns

As outlined above, the canonical hemodynamic response function is a model of the hemodynamic response expected after a single, instantaneous stimulation of the brain. In an

[1] http://www.fil.ion.ucl.ac.uk/spm/

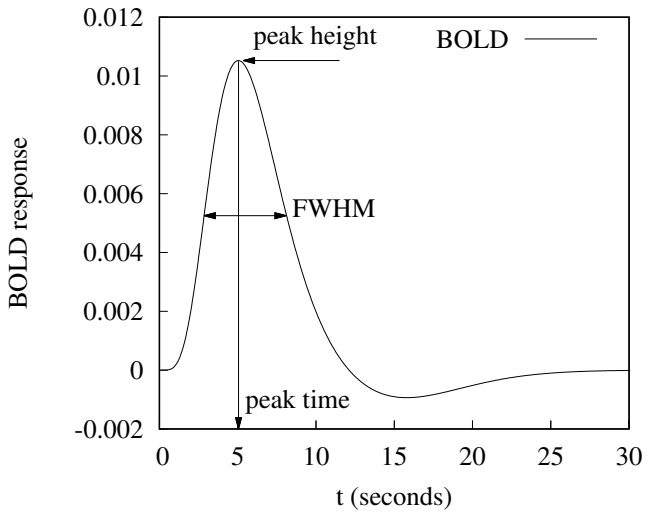

Figure 7.1.: Typical shape of the BOLD response to a single instantaneous stimulation. It can be described by its three characteristic properties peak height, peak time and full width at half maximum (FWHM).

experimental setting, however, the stimulus usually does not consist of a single stimulation, but of a pattern of stimuli which are applied. The observed BOLD response can therefore not be expected to follow the shape of the canonical HRF. Instead, the observed BOLD signal can be modelled as the convolution of the stimulus pattern and the hemodynamic response function. See Figure 7.2 for an example. The resulting shape, the expected BOLD signal in response to the applied stimulus pattern, is what the measured BOLD signal is compared to, to decide whether a region in the brain is active or not. The comparison is done via sophisticated statistical tests, whose details are not covered here. An excellent introductory review of the topic is the article by Lindquist (2008).

With the information about the origin of the BOLD signal and its description via the canonical HRF in mind, I will now outline the research questions that guided this modelling project.

7.4. Research questions for the present work

As outlined in Section 7.2, the shape of the BOLD response is determined by dynamic changes in both blood flow and oxygen level. However, the purely *phenomenological* description of the HRF currently used in clinical practice (Eq. 7.1) does not relate the BOLD shape to the underlying biological processes. It is therefore not possible to incorporate information about blood composition, vascular compliance or metabolic reaction dynamics

7. Predicting the influence of early metabolic alterations on the BOLD shape

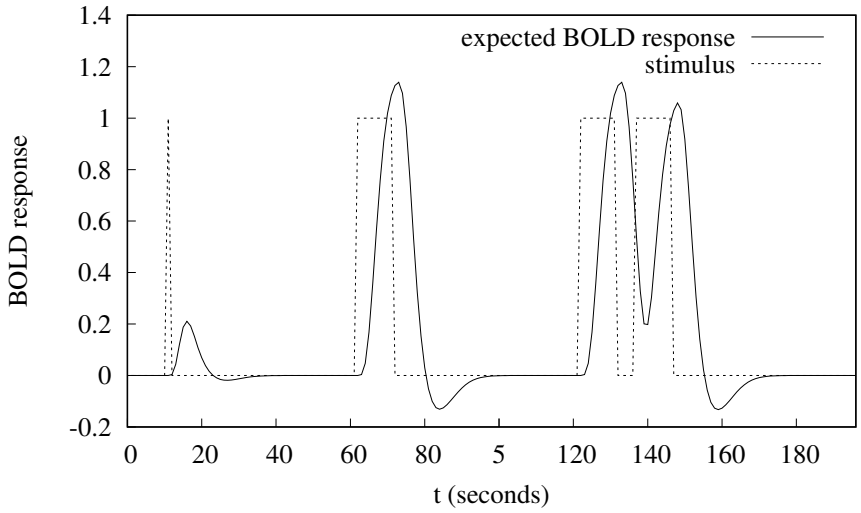

Figure 7.2.: Expected shape of the BOLD response to different stimuli.

in the clinical analysis of BOLD fMRI data. To include this information, a *mechanistic* description of the hemodynamic response and its biochemical foundations is needed.

This mechanistic descriptions needs to account for both components of the hemodynamic response: The vascular component, i.e. the increase in blood flow following a neuronal stimulation, and the metabolic component, i.e. the increased demand for oxygen as a result of neuronal activity. Understanding the importance of the latter component, the metabolic influence on the BOLD shape, is of special interest for Alzheimer's disease, where several metabolic alterations have been described to occur during disease progression.

Currently, it is still unknown how much the BOLD shape responds to changes in the underlying metabolic network. Answering this question would allow us to understand whether the changes observed in AD patients influence the result of BOLD fMRI.

The research questions that guide this modelling project are therefore as follows:

1. Is the shape of the BOLD signal sensitive to changes in the underlying metabolic network?

2. How much do known alterations in brain energy metabolism in AD affect the BOLD shape

The answer to these questions can be approached with the help of mathematical modelling. To do so, a suitable mathematical model would need to fulfil several requirements:

(I) The model needs to be able to describe the healthy state.

(II) It should be detailed enough to analyse the reported alterations.

(III) The model should allow for a quantification of the impact of the observed changes on the chosen outcome measure (i.e. the BOLD signal).

Ultimately, a model that fulfils these three requirements can be used to described the BOLD shaped using the three shape characteristics of the HRF (cf. Figure 7.1). Once the effect of alterations in the metabolic network and tissue composition can be quantified in terms of these three characteristics, this information can be used to calculate parameters of the canonical HRF (Equation 7.1), that mimic these changes. This, in turn, is a first step towards the inclusion of patient-specific data into the clinical analysis of fMRI data.

7.5. Metabolic modelling as part of the "VPH DARE@IT" project

The work presented in the following chapters is part of the EU-funded project "Virtual Physiological Human DementiA Research Enabled by IT" (VPH DARE@IT). The "VPH DARE@IT" project[2], running from 2013 to 2017, has the goal to improve the early differential diagnosis of dementia with a special focus on the influence of lifestyle and environmental factors. Part of the project is concernced with the mechanistic modelling of metabolism in dementia, and the application of the results to the analysis of clinical imaging data. One of the imaging modalities used in the project is BOLD fMRI.

The kinetic model whose development is described in the next chapters is part of a much larger modelling pipeline, depicted in Figure 7.3. The pipeline describes a multi-step process which incorporates gene expression analysis, constraint-based modelling and kinetic modelling. All these different techniques and paradigms have been applied by various partners in the "VPH-DARE@IT" project. The final goal is to generate patient-specific and disease state-specific models of brain energy metabolism. These models are intended to improve the clinical analysis of fMRI data for patients with Alzheimer's disease.

The first step in the pipeline is the measurement of gene expression data in brain samples of AD cases. The patients have been grouped according to Braak stages. Braak staging uses information about the spatial occurrence of neurofibrillary aggregates of the tau protein which correlates to cognitive decline in Alzheimer's disease (Braak and Braak, 1991). Sample preparation and data analysis was conducted in the laboratory of Mikko Hiltunen, University of Eastern Finland[3].

The second step in the pipeline is the use of this gene expression data to construct whole

[2] www.vph-dare.eu

[3] http://www.uef.fi/en/web/molecular-genetics-of-alzheimers-disease/home

genome metabolic models for humans at the different Braak stages. Model construction and calibration was performed by Paula Jouthen, Merja Oja and Gholamreza Bidhkori at the VTT Technical Research Centre of Finland[4].

The third step in the pipeline consists of the calibration of the kinetic metabolic model described in this thesis with the disease state-specific flux data calculated by the stoichiometric model. This step implements the calculation of disease state-specific parameters for the canonical hemodynamic response functions as envisaged above. More information about the implementation can be found in Section 10.5.

The next chapter introduces the main metabolic pathways and reactions that control oxygen consumption in the brain and which consequently need to be considered in a mathematical model.

[4]http://www.vtt.fi/

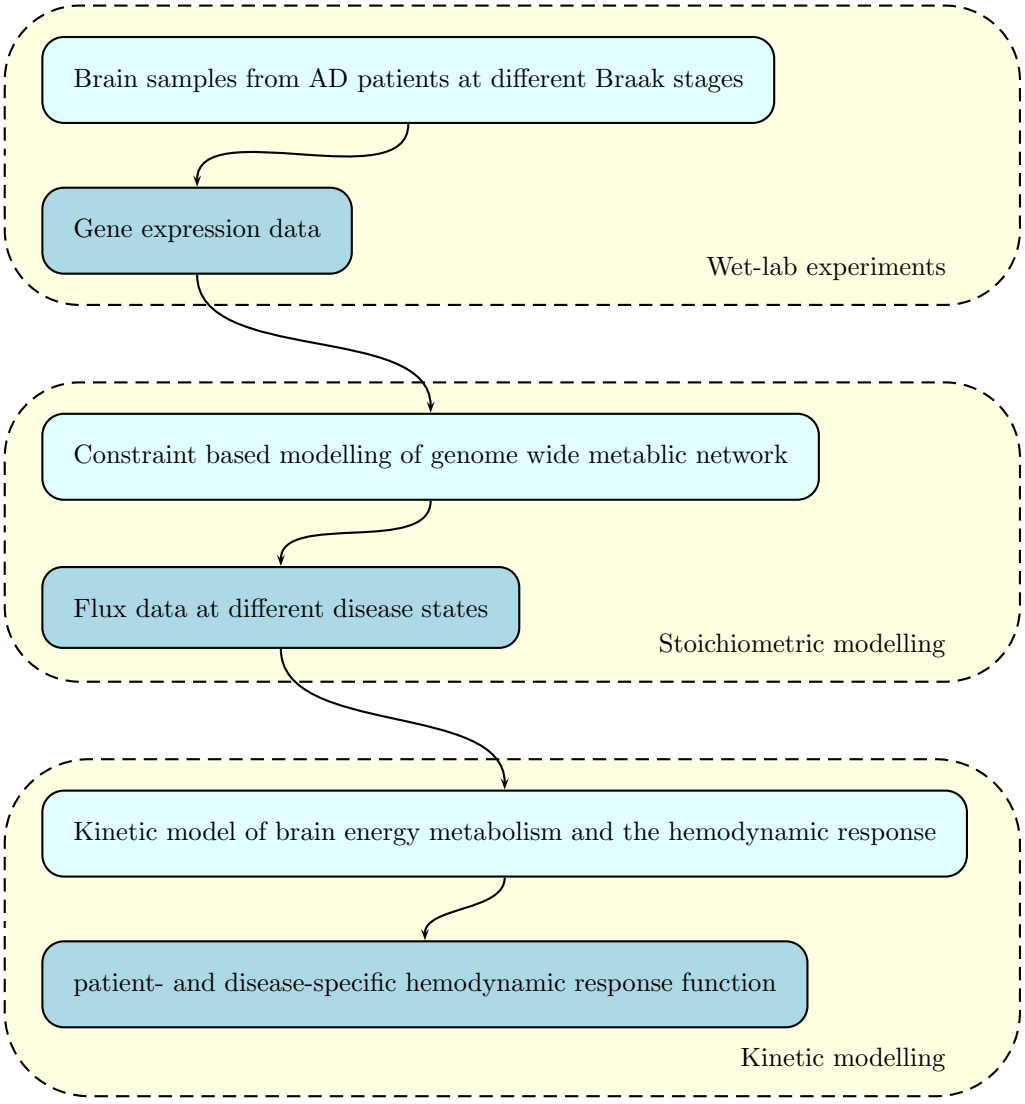

Figure 7.3.: Outline of "VPH DARE@IT" pipeline for the generation of a disease state-specific hemodynamic response function. Patient data for gene expression analysis are collected post-mortem for all six Braak stages. These data are used to calculate disease-state specific flux distributions for a brain specific metabolic network model by Sertbaş et al. (2014). The calculated fluxes are used as an input for the calculation of disease-specific kinetic models.

8. From Glucose to ATP – Main pathways of energy metabolism in the brain and their importance in AD

The human brain has a high demand for energy. While it usually makes up for only 2 percent of the total body mass, it utilizes about 25% of glucose consumed by the body (Bélanger et al., 2011). Glucose enters the brain via the blood-brain barrier, using specialized membrane proteins called glucose transporters (GLUTs). Once inside the brain, glucose is processed by the glycolytic pathway, which transforms it via several metabolic steps into pyruvic acid (pyruvate). Pyruvate can be transported into the mitochondria, where it constitutes the main substrate of the citric acid cycle. The citric acid cycle produces, besides other products, NADH which is consumed during oxidative phosphorylation to create ATP from ADP. If pyruvate is not transported into the mitochondria, it can be reversibly transformed into lactate, which can be exchanged between different cell types in the brain.

The process of generation of energy in the form of ATP from glucose, outlined above, is highly regulated, with the interactions between neurons and astrocytes being paramount for its functioning in the brain (Bélanger et al., 2011). Before I discuss the role of neurons and astrocytes in detail, I will describe the metabolic pathways mentioned above at a level necessary to understand the mathematical models presented in Chapter 9 and Chapter 10. I will also present the pentose phosphate pathway, which connects to the glycolytic pathway and is of special importance in Alzheimer's disease.

8.1. Glycolysis – fast anaerobic production of small amounts of ATP

The first reaction in the glycolytic pathway (shown in Figure 8.1, p66) is the phosphorylation of glucose (GLC) into glucose 6-phosphate (G6P) catalysed by the enzyme hexokinase (HK, EC 2.7.1.1). The phosphate group used in this reaction is donated by ATP, which is

thereby transformed into ADP. G6P can be transformed into several different molecules,

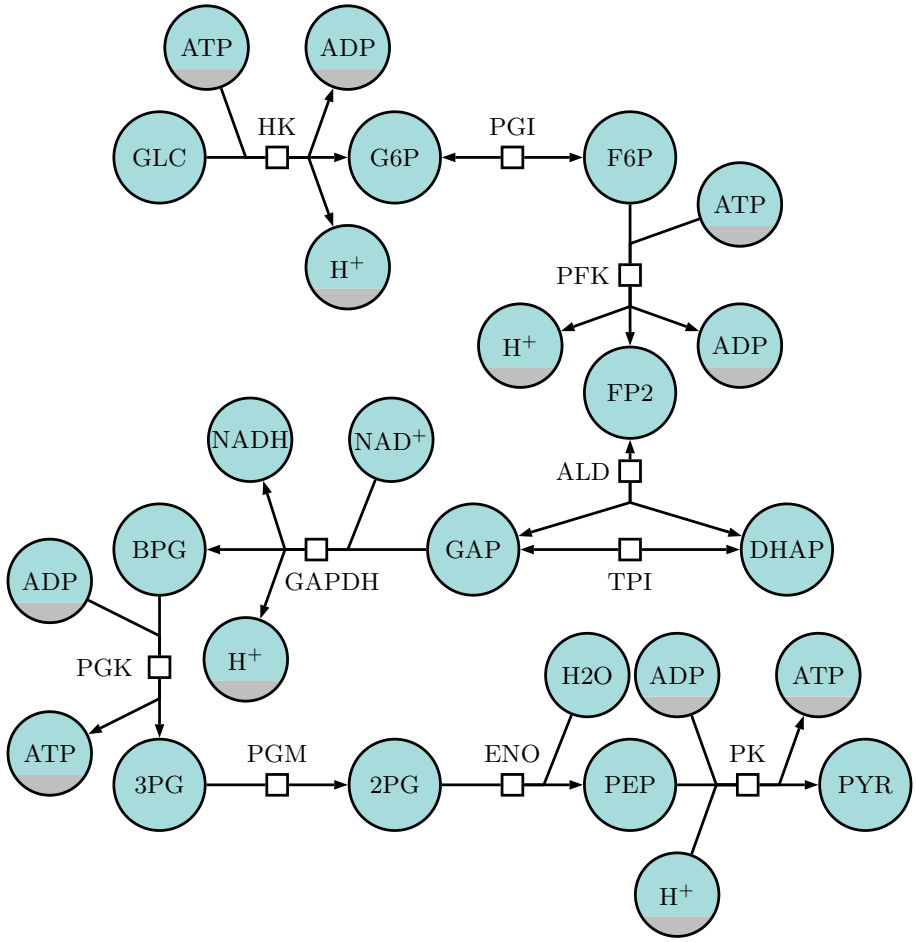

Figure 8.1.: SBGN process description (PD) map of reactions inside the glycolytic pathway. For enzymes catalysing each reaction only the short names are given to avoid crowding. For each molecule of glucose that enters the glycolytic pathway two molecules of ATP and two molecules of NADH are produced.

but in the glycolytic pathway it is isomerized to fructose 6-phosphate (F6P) by the enzyme phosphoglucose isomerase (PGI, EC 5.3.1.9). F6P is then phosphorylated to fructose 1,6-bisphosphate (FP2) by the enzyme phosphofructokinase (PFK, EC 2.7.1.11). This reaction again requires ATP to donate a phosphate group. FP2 is split by the enzyme aldolase (EC 4.1.2.13) into glyceraldehyde 3-phosphate (GAP) and dihydroxyacetone phosphate (DHAP). Each of these two molecules can be converted into the other, a reaction catalysed by triosephosphate isomerase (TPI, EC 5.3.1.1). GAP is subsequently transformed into 1,3-bisphosphoglyceric acid (BPG) by the enzyme glyceraldehyde 3-phosphate dehydrogenase (GAPDH, EC 1.2.1.12). The reaction includes a reduction of NAD+ to NADH. The next reaction is the first reaction to produce ATP: BPG is converted into 3-phosphoglyceric acid (3PG), catalysed by phosphoglycerate kinase (PGK, EC 2.7.2.3).

In this process, a phosphate group is released from BPG and attached to ADP, producing ATP. 3PG is then converted into 2-phosphoglyceric acid by the enzyme phosphoglycerate mutase (PGM, EC 5.4.2.11). In the penultimate step of the glycolytic pathway, the enzyme enolase (EC 4.2.1.11) catalyses the conversion of 2PG into phosphoenolpyruvic acid (PEP). As a byproduct, a water molecule is released. Finally, pyruvic acid (PYR) is produced from PEP. This reaction is catalysed by pyruvate kinase (PK, EC 2.7.1.40) a reaction which moves a phosphate group from PEP to ADP, thereby creating another molecule of ATP.

The glycolytic pathway is regulated mainly by three reactions: the reactions catalysed by hexokinase, phosphofructokinase and pyruvate kinase. Hexokinase is inhibited by the product of the reaction it catalyses, glucose 6-phosphate. Phosphofructokinase is allosterically inhibited by ATP. This reaction can therefore act as an energy requirement sensor. Pyruvate kinase, the enzyme catalysing the last reaction in the glycolytic pathways is also inhibited by ATP. However, in contrast to the other two enzymes, it can also be activated by fructose 1,6-bisphosphate. Summing up over the different reactions, the total gain of ATP is 2 molecules per molecule of glucose which enters the glycolytic pathway. In addition to these molecules of ATP, the main products of the glycolytic pathway are pyruvate and one molecule of NADH, which enter the citric acid cycle discussed next.

8.2. The citric acid cycle and oxidative phosphorylation – aerobic generation of energy

Unlike glycolysis, which takes place in the cytoplasm, the citric acid cycle and oxidative phosphorylation take place in the mitochondria. Together, these two pathways provide most of the energy needed in the brain. They are linked to glycolysis via the uptake of pyruvate by the mitochondria. Inside the mitochondria, pyruvate undergoes a complicated and highly regulated conversion into acetyl coenzyme A (acetyl CoA) before it can enter the citric acid cycle (Fig 8.2, p68). This conversion is catalysed by several enzymes, which form the pyruvate dehydrogenase complex.

The following description of the citric acid cycle and oxidative phosphorylation is kept very brief. For a more detailed explanation see a standard text book on biochemistry (e.g. Berg et al. (2002)).

Acetyl CoA enters the citric acid cycle together with oxaloacetate (OA) as a substrate in the first reaction, the formation of citrate (Cit) and coenzyme A (CoA, See Figure 8.3, p69). The transfer of the acetyl unit from acetyl CoA to OA is catalysed by citrate

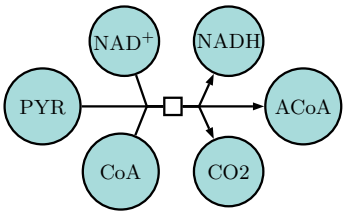

Figure 8.2.: SBGN PD map of the conversion of pyruvate (PYR) to acetyl coenzyme A (ACoA) catalyzed by the pyruvate dehydrogenase complex. One molecule of NADH is produced for each molecule of pyruvate that is decarboxylized. Hydrogen which is the fourth product of this reaction is not shown.

synthase (CS, EC 2.3.3.1). The next reaction is the isomerisation of citrate into isocitrate (IsoCit), catalysed by aconitase (AC, EC 4.2.1.3). Isocitrate itself is oxidized and decarboxylated to alpha-ketoglutarate (aKG). This reaction is catalysed by isocitrate dehydrogenase (IDH, EC 1.1.1.42). During this reaction, hydrogen is moved from IsoCit to NAD+ to generate NADH. This transfer is important, as it is the first of several times NADH is generated. NADH will later be used during oxidative phosphorylation to generate ATP. In the next step in the citric acid cycle, catalysed by the α-ketoglutarate dehydrogenase complex (OGDC), alpha ketoglutarate is oxidized to succinyl coenzyme A (succinyl CoA, SucCoA), This reaction has CoA and NAD+ as additional substrates and is the second reaction that generates NADH. The following reaction, the cleavage of CoA from succinyl catalysed by succinyl coenzyme A synthesase (SCS, EC 6.2.1.4), is coupled to the phosphorylation of ADP to ATP. This is the only instance that ATP is directly produced in the cycle. Besides ATP, this reaction also produces CoA and succinate (Suc). Succinate is subsequently oxidized to fumarate (Fum). This reaction is catalysed by succinate dehydrogenase (SQR, EC 1.3.5.1) and includes the conversion of FAD to FADH2. FADH2 is later consumed during oxidative phosphorylation. Next, fumarate is converted into malate (Mal), a reaction catalysed by the enzyme fumarase (EC 4.2.1.2). The citric acid cycle is closed by the oxidation of malate to oxaloacetate. This final reaction is catalysed by malate dehydrogenase (MDH, EC 1.1.1.37) and produces a further NADH from NAD+.

Regulation of the citric acid cycle is mainly achieved by allosteric inhibition or activation of the two enzymes isocitrate dehydrogenase (activation by ADP, inhibited by ATP and NADH) and α-ketoglutarate dehydrogenase (inhibited by NADH, ATP and SucCoA).

In summary, the energetically relevant products of the citric acid cycle are one molecule of ATP, three molecules of NADH and one molecule of FADH2. The ATP can be directly used as a source of energy, while NADH and FADH2 are used during oxidative phosphorylation, as described next.

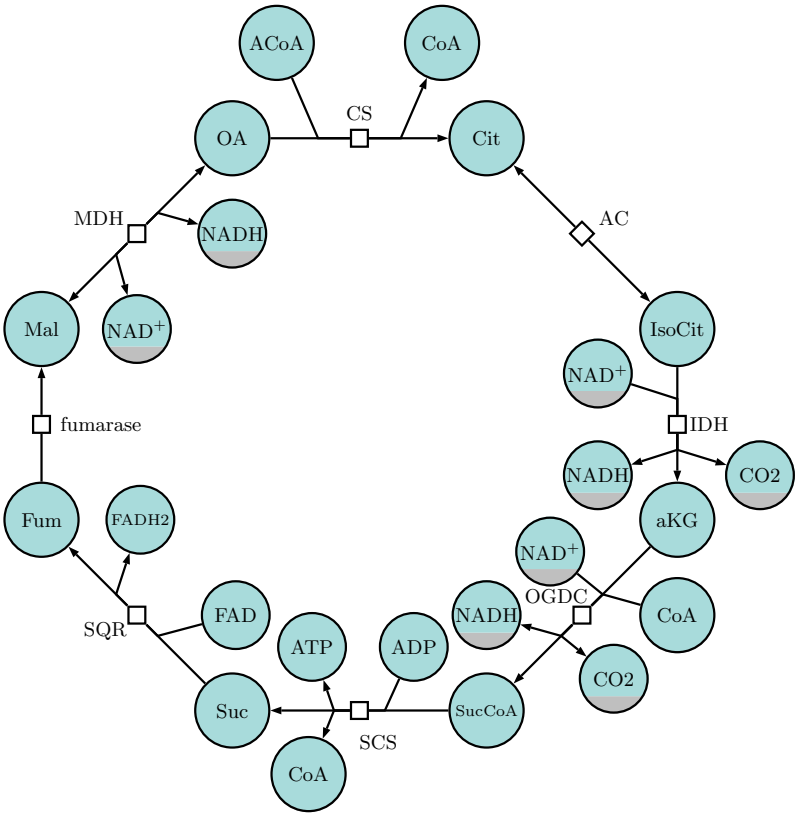

Figure 8.3.: SBGN PD map of the main metabolic reactions of the citric acid cycle. The enzymes catalysing the different reactions are only shown with the names.

Oxidative phosphorylation takes place in the mitochondrial matrix, and is achieved by the electron transport chain, a set of four large protein complexes. In a first step, oxygen is reduced to water, using hydrogen donated by FADH2 and NADH. This process takes place by a series of reactions inside the electron transport chain. Besides the reduction of oxygen, these reactions also create a proton gradient between the inner and the outer mitochondrial membranes. This proton gradient is the source of energy used for synthesis of ATP from ADP.

Oxidative phosphorylation is the source of most of the ATP used in the brain. For each molecule of glucose that enters the brain and is completely oxidized to water, 26 molecules of ATP are generated by this process alone. Five from the NADH produced during the decarboxylation of pyruvate, three from the two molecules of FADH2 produced in the citric acid cycle, fifteen from the 6 molecules of NADH produced in the citric acid cycle and three from the two molecules of NADH produced in the glycolytic pathway. The ATP gain from the NADH produced in the glycolytic pathway is smaller than the ATP gain from the NADH produced during the citric acid cycle as NADH cannot be transported into the mitochondria directly. Instead, electrons from cytosolic NADH enter via different

intermediates which lead to a lower ATP yield.

The overall gain of ATP for one molecule of glucose that is completely oxidized is therefore 30 molecules of ATP: Two from glycolysis, two from the citric acid cycle and twenty-six from oxidative phosphorylation.

8.3. The pentose phosphate pathway – biosynthesis and protection against oxidative damage

The pentose phosphate pathway (PPP) uses glucose 6-phosphate, an intermediate of the glycolytic pathway, to produce carbon dioxide, NADPH and ribose 5-phosphate. It can be divided into the oxidative branch which consists of three reactions and the non-oxidative branch which consists of five reactions. NADPH is required for the defence against oxidative damage. Ribose 5-phosphate is required for the biosynthesis of many molecules, including RNA and DNA (Stincone et al., 2015).

The first reaction in the oxidative branch of the pentose phosphate pathway is the transformation of glucose 6-phosphate (G6P) into 6-phosphoglucono-δ-lactone (G6L) (Fig. 8.4, p72). This reaction is catalysed by the enzyme glucose 6-phosphate dehydrogenase (G6PDH, E.C. 1.1.1.49) and produces the first molecule of NADPH. The next reaction is the hydrolization of G6L to 6-phosphogluconate (P6G), catalyzed by 6-phosphogluconolactonase (6PGL, E.C. 3.1.1.31). P6G is subsequently decarboxylized into ribulose 5-phosphate (Ru5P). This reaction is catalysed by 6-phosphogluconate dehydrogenase (GND, E.C 1.1.1.44) and produces a second molecule of NADPH. The following five reversible reactions make up the non-oxidative branch of the pentose phosphate pathway. R5uP can take part in two different reactions. In the first reaction, it is converted into xylulose 5-phosphate (X5P) by the enzyme ribulose 5-phosphate epimerase (RPE, E.C. 5.1.3.1). In the second reaction, it is isomerized into ribose 5-phosphate (R5P) by the enzyme ribulose 5-phosphate isomerase (RPI, E.C. 5.3.1.6).

The remaining three reactions of the pentose phosphate pathway connect this pathway with the glycolytic pathway. X5P and R5P are transformed into GAP and sedoheptulose 7-phosphate (S7P), catalysed by transketolase (TKL, E.C. 2.2.1.1). GAP and S7P are transformed into F6P and erythrose 4-phosphate (E4P), catalysed by transaldolase (TAL, E.C. 2.2.1.2). Finally, E4P and X5P are transformed into F6P and GAP, catalysed again by transketolase.

As all reactions of the non-oxidative branch are reversible, the pentose phosphate pathway can remove molecules from the glycolytic pathway to produce ribose 5-phosphate in

situations of high demand. In situations of low demand for ribose 5-phosphate, the flux can go towards the intermediates of the glycolytic pathyway.

In brain energy metabolism, the most important role of the PPP is the generation of NADPH needed for defence against oxidative damage (Stincone et al., 2015).

For a detailed review of the properties, regulation and importance of the pentose phosphate pathway see the detailed review by Stincone et al. (2015). A discussion of the role of the PPP for oxidative defence and in other diseases such as cancer, can be found in (Riganti et al., 2012).

8.4. Energy buffers: glycogen and creatine kinase

Two systems for short term energy buffering can be found in the brain. The first, active in both neurons and astrocytes, consists of the reversible phosphorylation of creatine to phosphocreatine by the enzyme creatine kinase (CK, EC 2.7.3.2). The second system, in the brain active predominantly in astrocytes, is the storage of glycogen.

Creatine - phosphocreatine conversion

The reversible phosphorylation of creatine (Cr) to phosphocreatine (PCr) catalysed by the enzyme creatine kinase (CK) has been extensively studied. The phosphorylation step takes a phosphate group from ATP and attaches it to Cr. The reverse reaction, the dephosphorylation of PCr, transfers the phosphate group from creatine to ADP (See Figure 8.5). Dephosphorylation of PCr can therefore serve as a rapid source of ATP.

Several functions for the CK/PCr system have been identified, including that of a temporal energy buffer, a spatial energy buffer and prevention of the loss of intracellular adenine nucleotides (Wallimann et al., 1992).

For the discussion here, the first of these functions is of main importance. In the brain, creatine kinase has been observed in neurons, astrocytes and oligodendrocytes (Wallimann et al., 1992). Different isoenzymes have been described in the mitochondria and in the cytosol, and their interplay may allow for an “energy shuttle” from the mitochondria to the cytosol (Schlattner et al., 2006).

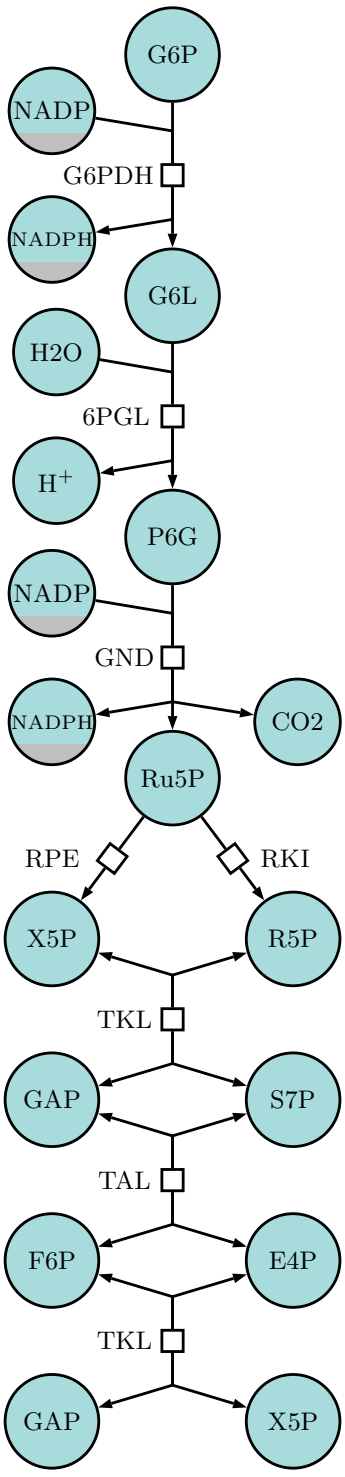

Figure 8.4.: SBGN PD map of the main metabolic reactions of the pentose phosphate pathway. Note the two molecules of NADPH produced in the oxidative branch as well as the connection to glycolysis via G6P, GAP and F6P.

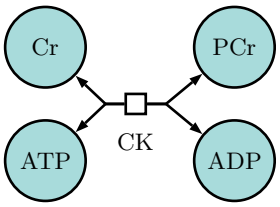

Figure 8.5.: Reversible conversion of creatine to phosphocreatine catalysed by creatine kinase

Glycogen storage

Glycogen is a crystalline repository for stored glucose, abundant in liver and muscle cells. In the adult human brain, comparatively smaller pools of glycogen can be found mainly in astrocytes, especially in the grey matter. While the role of glycogen in the liver and in muscle cells is well established, its functional role in the brain has been debated (Brown and Ransom, 2007). Only with the observation of the exchange of lactate from astrocytes to neurons, as discussed later, its importance in the supply of energy during hypoglycemia and during increased energy demand in neurons has been established (Brown and Ransom, 2007).

Glycogen is formed by transformation of glucose 6-phosphate via two reversible metabolic steps into uridine diphosphate glucose (UDP-glucose), catalysed by phosphoglucomutase (EC 5.4.2.2) and UDP-glucose pyrophosphorylase (EC 2.7.7.9). The active (dephosphorylated) form of glycogen synthase then catalyses the buildup of glycogen from UDP-glucose. Glycogen breakdown (glycogenolysis) is catalysed by active (phosphorylated) form of glycogen phosphorylase (See Figure 8.6). The process of glycogenolysis takes only milliseconds and provides a fast substrate for glycolysis which is independent of the blood flow (Raichle and Mintun, 2006).

For a detailed description of the role of glycogen storage in astrocytes see the review by Brown and Ransom (2007). Neuronal glycogen is discussed in (Saez et al., 2014).

8.5. The importance of astrocyte-neuronal interaction for brain energy metabolism

With the exception of glycogen storage, all of the metabolic reactions introduced above can be found in both astrocytes and neurons. However, based on their physiology, location and different enzyme expression levels, neurons and astrocytes have different roles in the provision of energy. The following short discussion is largely based on the excellent review

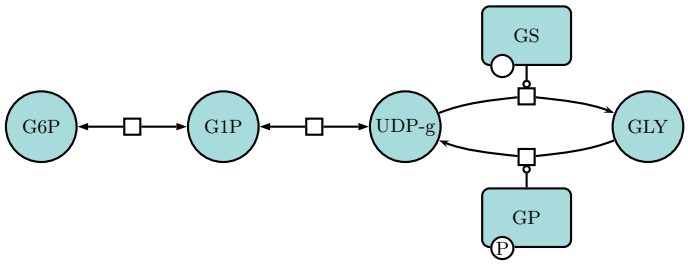

Figure 8.6.: Glycogen is produced by the reversible conversion of glucose 6-phosphate (G6P) into glucose 1-phosphate (G1P), the reversible conversion of G1P into uridine diphosphate glucose (UDP-glucose) and the final synthesis of glycogen from UDP-glucose. The first two steps are catalysed by phosphoglucomutase and UDP glucose pyrophosphate. Synthesis of glycogen is regulated by glycogen synthase (GS), breakup into UDP-glucose is regulated by glycogen phosphorylase (GP). The process is regulated by the phosphorylation and dephosphorylation of GS and GP.

by Bélanger et al. (2011) and the reader is referred there for further information.

Astrocytes, whose endfeet enwrap the cerebral blood vessels have direct access to glucose and oxygen delivered via the blood. Due to their location, astrocytes have been implicated in the regulation of cerebral blood flow (Bélanger et al., 2011). Neurons, instead, have no direct connection to the vasculature and rely on supply of substrates from the extracellular space. In addition to the different location, there are also differences in the activity of the metabolic pathways in neurons and astrocytes. Astrocytes are considered to rely mainly on glycolysis for the fast production of ATP. As a consequence, they produce more pyruvate than needed for oxidative phosphorylation. Without uptake of pyruvate into the mitochondria, it is converted into lactate, thereby shifting the lactate/pyruvate ratio. Raichle and Mintun (2006) suggested that this shift, which is closely coupled to the NADH/NAD+ ratio, might act as a sensor for the regulation of blood flow. The excess lactate can be transported into neurons, where it can be used as additional fuel for the citric acid cycle. The use of astrocytic lactate in neurons may also spare neuronal glucose for its use in the PPP (Stincone et al., 2015).

This transport of lactate from astrocytes to neurons has been termed the “astrocyte neuron lactate shuttle” (ANLS). How important the ANLS is, is a matter of an ongoing debate and several experimental and modelling works specifically target this question. One of the open questions, for example, is how much of the excess lactate produced by astrocytes is used in neurons, and how much is removed via the blood (Raichle and Mintun, 2006).

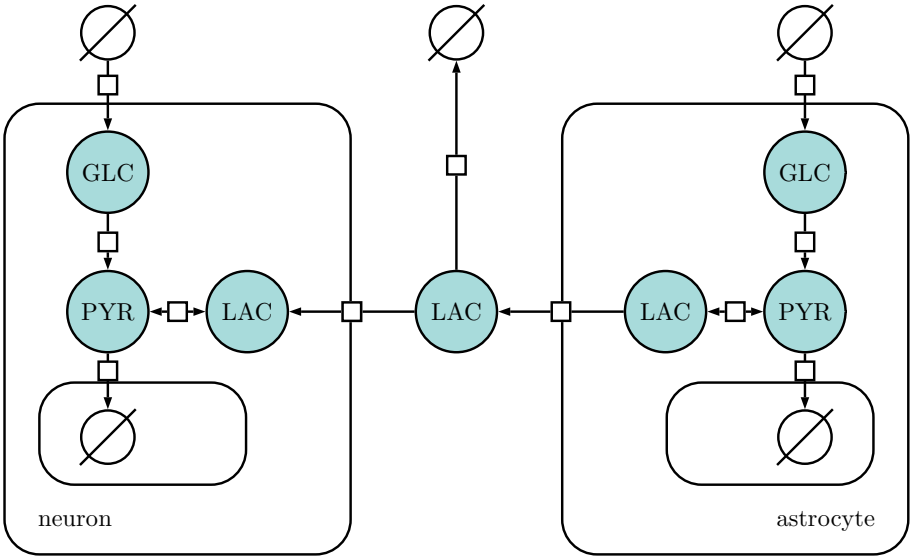

Figure 8.7.: SBGN PD map of the main ideas behind the astrocyte neuron lactate shuttle (ANLS). Glycolysis in astrocytes produces excess lactate, which is shuttled into the extracellular space. From there, it can be taken up by neurons which use it as additional fuel for oxidative phosphorylation. How much of the extracellular lactate is taken up by neurons is still a matter of research.

8.6. Alterations in brain energy metabolism in Alzheimer's disease

Alzheimer's disease has been shown to influence all of the different pathways of brain energy metabolism. In the following, I will only describe the observations that have been analysed in Chapter 11, namely changes in glycolysis, the pentose phosphate pathway and alterations in the tissue composition in AD. I will specifically not elucidate the important role of mitochondria in AD, a topic that has been outside the scope of my work. The interested reader is referred to the publications by Wang et al. (2014); Swerdlow et al. (2014) and Salminen et al. (2015). The role of creatine kinase in Alzheimer's disease is discussed in Bürklen et al. (2006).

The expression of pyruvate kinase, lactate dehydrogenase and phosphofructokinase is increased in several brain regions in AD

Changes in the glycolytic pathway are the topic of a series of articles by Bigl et al. (Bigl et al., 1996, 1999). In particular, the authors report increased levels of phosphofructokinase in the frontal and temporal cortex of AD patients compared to a control group. In the same

study, no change in the activity of aldolase was found (Bigl et al., 1996). In 1999, the same group of authors analysed the activity of other glycolytic enzymes, including hexokinase, pyruvate kinase and lactate dehydrogenase. In this study, significantly increased levels of lactate dehydrogenase in the basal forebrain and in the frontal cortex as well as significantly increased levels of pyruvate kinase in the frontal cortex are reported. For hexokinase, no significant change was established (Bigl et al., 1999).

The activity of the pentose phosphate pathway is increased in AD

The pentose phosphate pathway has been the subject of several publications related to AD. In the publication by Russel et al. (1999) an upregulation of neuronal glucose-6-phosphate dehydrogenase was observed. The authors concluded that the observed increase in PPP activity is consistent with an "attempted reductive compensation to oxidative stress". In the paper by Palmer (1999), a significant increase in glucose-6-phosphate dehydrogenase and 6-phosphogluconate dehydrogenase in the inferior temporal cortex of AD patients is described. The authors use this observation to suggest a "state of oxidative stress in the AD brain".

Astrocyte hyperplasia and hypertrophy have been reported in AD patients

In addition to the changes in the metabolic pathways, there are studies that indicate changes in the cerebral composition in AD. Of main importance is the finding, that both astrocyte hyperplasia and astrocyte hypertrophy have been reported in AD. Immunochemical studies of activated astrocytes in hippocampus and enthorinal cortex of Alzheimer's disease patients have shown an increased number of GFAP positive astrocytes (Vanzani et al., 2005). Similar results were published by Robinson (2001), who reported a 1.4-fold increase in astrocytic density in AD patients compared to controls, and Vijayan et al. (1991), who found a general increase in the number of astrocytes. Recent evidence suggests, however, that the observed changes in the number of astrocytes are not due to increased proliferation, but are a consequence of phenotypic changes (Serrano-Pozo et al., 2013). This would be in line with several reports of astrocytic hypertrophy as a consequence of reactive astrogliosis in AD (Sofroniew and Vinters, 2010; Rodríguez et al., 2008).

Regardless of the underlying phenomena, both hyperplasia and hypertrophy could influence the result of BOLD fMRI analyses, as they result in an increased astrocytic volume fraction in the observed voxel.

9. Computational models of brain energy metabolism and the hemodynamic response

The history of mathematical models of energy metabolism can be traced back to publications from Evgeni Selkov at the end of the 60s of the previous century, who constructed and analysed simplified models of glycolysis (Selkov, 1968, 1975). Since then, a plethora of models have been developed, and even a list of them is beyond the scope of this work. I will restrict the discussion therefore here to the models that can be seen as the ancestors of the new model developed as part of this work, i.e. those models which through various generations have contributed to the model described in Chapter 10. This includes one model for glycolysis in erythrocytes (Heinrich and Schuster, 1996), three models with an increasingly detailed description of human brain energy metabolism (Aubert et al., 2001; Aubert and Costalat, 2002, 2005) and one model of brain energy metabolism in mice (Cloutier et al., 2009). For each model, I will highlight the main contributions with respect to the covered scope and the relevance for the application to BOLD fMRI. To do so, I will focus mainly on the concepts which have been newly introduced with each model, and the mathematical descriptions used to express these concepts.

The first model in this lineage is a simplified model of erythrocyte glycolysis, constructed by Heinrich and Schuster (1996).

9.1. Heinrich and Schuster 1996 – Glycolysis in erythrocytes

The model describes the production of pyruvate (PYR) from glucose (GLC) via four, partially parallel, steps (Figure 9.1). Six differential equations describe the kinetics of 1,3BPG, 2,3BPG, PEP, AMP, ATP and ADP, while the concentration of glucose and pyruvate are not part of the model:

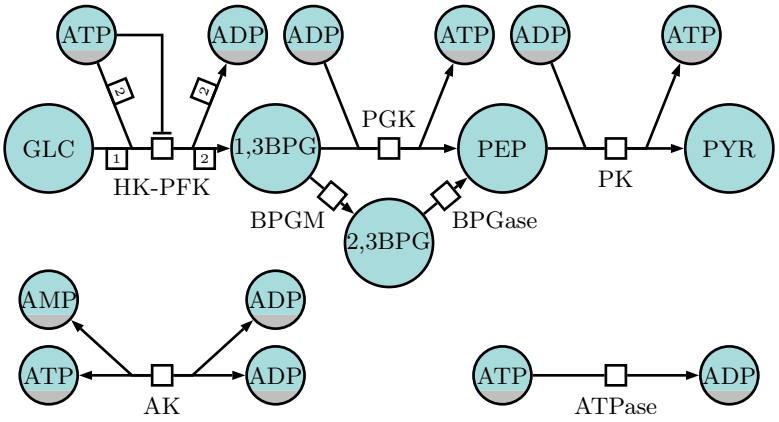

Figure 9.1.: SBGN-PD map of the metabolic reactions considered by Heinrich and Schuster (1996).

$$\frac{\mathrm{d1,3BPG}}{\mathrm{d}t} = 2v_{\mathrm{HK-PFK}} - v_{\mathrm{BPGM}} - v_{\mathrm{PGK}}, \tag{9.1}$$

$$\frac{\mathrm{d2,3BPG}}{\mathrm{d}t} = v_{\mathrm{BPGM}} - v_{\mathrm{BPGase}}, \tag{9.2}$$

$$\frac{\mathrm{dPEP}}{\mathrm{d}t} = v_{\mathrm{BPGase}} + v_{\mathrm{PGK}} - v_{\mathrm{PK}}, \tag{9.3}$$

$$\frac{\mathrm{dAMP}}{\mathrm{d}t} = -v_{\mathrm{AK}}, \tag{9.4}$$

$$\frac{\mathrm{dADP}}{\mathrm{d}t} = 2v_{\mathrm{HK-PFK}} - v_{\mathrm{PGK}} - v_{\mathrm{PK}} + v_{\mathrm{ATPase}} + 2v_{\mathrm{AK}}, \tag{9.5}$$

$$\frac{\mathrm{dATP}}{\mathrm{d}t} = -2v_{\mathrm{HK-PFK}} + v_{\mathrm{PGK}} + v_{\mathrm{PK}} - v_{\mathrm{ATPase}} - 2v_{\mathrm{AK}}. \tag{9.6}$$

Although the model is a quite reduced depiction of the glycolytic network in erythrocytes, the authors introduce several features which are present in the models described later. Three of these features merit an explanation:

1. *The HK-PFK reaction is inhibited by its substrate ATP.* The reaction HK-PFK is a lumped description of the first steps of the glycolytic pathway. One of these reactions is catalysed by the enzyme phosphofructokinase, which is inhibited by its substrate ATP (See Section 8.1). This inhibition is explicitly expressed in the model, as $v_{\mathrm{HK-PFK}}$ is described as

$$v_{\mathrm{HK-PFK}} = k_{\mathrm{HK-PFK}} \cdot \mathrm{ATP} \cdot \left(1 + \frac{\mathrm{ATP}}{K_{I,ATP}}^{nH}\right)^{-1} \tag{9.7}$$

   with the inhibition constant $K_{I,ATP} = 1.0mM$ and the cooperativity constant $nH = 4$.

2. *The sum of the concentrations of ATP, AMP and ADP are constant.* According to Equations (9.4),(9.5) and (9.6) the sum of ATP, ADP and AMP is constant.

$$\mathrm{ADP} + \mathrm{ATP} + \mathrm{AMP} = A = const.$$

This can be used to express the amount of AMP as

$$\text{AMP} = A - \text{ADP} - \text{ATP}. \tag{9.8}$$

3. *The reaction catalyzed by adenylate kinase is assumed to reach a rapid equilibrium.* Heinrich and Schuster (1996) assume that the rapid-equilibrium approximation can be applied to Equation 9.4, i. e.

$$2 \cdot ADP \overset{AK}{\leftrightarrow} ATP + AMP$$

can be rewritten as

$$\frac{(ADP)^2}{ATP \cdot AMP} = q_{ak} \tag{9.9}$$

The model is used to analyse the dynamic properties of the glycolytic pathway in dependence of the rate of v_{ATPase} and describes stable steady states of the ATP concentration. These steady states are identified as the result of both the substrate inhibition of the HK – PFK reaction and the ability of the system to vary the amount of ATP produced by changing the level of flux through the 2,3BPG bypass.

This model by Heinrich and Schuster provided the basis for a first model describing the coupling between brain electrical activity and metabolism. Aubert et al. (2001) presented a model which couples brain energy metabolism with neuronal stimulation, already with the application to functional imaging techniques in mind.

9.2. Aubert 2001, 2002 and 2005 – Brain energy metabolism and the BOLD response

The next three models are all published by a single group, which made major contributions to the current state of the art.

Aubert, Costalat and Valabrègue 2001 – From blood cells to brain cells

The core of the first model are eight metabolic reactions, of which five are taken from the model by Heinrich and Schuster (1996). The first reactions of glycolysis are again modeled as one step (HK-PFK), although this time the resulting species is glyceraldehyde 3-phosphate (GAP), instead of 1,3-biphosphoglycerate (BPG). This difference is motivated by the absence of the 2,3-biphosphoglycerate bypass in the brain and the additional

inclusion of NAD^+ and NADH. The first reaction is followed by PGK which incorporates the different metabolic steps from GAP to PEP. The following transformation of PEP into PYR is catalysed by pyruvate kinase (PK). In addition to these reactions, Aubert et al. extend the metabolic network by explicitly describing the lactate dehydrogenase catalysed transformation of pyruvate into lactate, the consumption of pyruvate and oxygen by mitochondrial respiration and the buffering of energy by creatine kinase (cf. Section 8.4). The ATP/ADP balance already considered by Heinrich and Schuster (1996), is complemented by the balance of NAD^+ and NADH (NAD^+ + NADH = N) and the balance of creatine and phosphocreatine (Cr + PCr = C). The full metabolic network consists of eight reactions (Figure 9.2, p81).

Another important extension compared to the model by Heinrich and Schuster (1996) is the introduction of compartments and corresponding transport reactions for glucose, lactate and oxygen. The concentration of these three species is considered in capillaries and neurons. Capillary concentration is assumed to be equal to the average value of arterial and venous concentrations and the time derivatives of capillary glucose, lactate and oxygen are given as:

$$\begin{aligned}
\frac{\mathrm{dGLC}^c}{\mathrm{d}t} &= v_{\mathrm{GLC}^c} - \frac{1}{r_c} v_{\mathrm{GLC}^m} \\
\frac{\mathrm{dLAC}^c}{\mathrm{d}t} &= v_{\mathrm{LAC}^c} + \frac{1}{r_c} v_{\mathrm{LAC}^m} \\
\frac{\mathrm{dO_2}^c}{\mathrm{d}t} &= v_{\mathrm{O_2}^c} - \frac{1}{r_c} v_{\mathrm{O_2}^m}
\end{aligned}$$

with v_{GLC^c} being the contribution of arterial and venous glucose concentrations, v_{GLC^m} describing the transport from the blood to the brain and r_c the ratio of capillary volume and neuronal volume ($r_c = \frac{V_c}{V_n}$). $v_{\mathrm{LAC}^c}, v_{\mathrm{LAC}^m}, v_{\mathrm{O_2}^c}$ and $v_{\mathrm{O_2}^m}$ are defined accordingly. For the derivation of these equations see the Appendix, Section A. For the transport of glucose and lactate through the blood brain barrier, v_{GLC_m} and v_{LAC_m}, facilitated transport is assumed:

$$v_{\mathrm{GLC}^m} = V_{max,\mathrm{GLC}} \left(\frac{\mathrm{GLC}^c}{\mathrm{GLC}^c + K_t} - \frac{\mathrm{GLC}^t}{\mathrm{GLC}^t + K_t} \right) \tag{9.10}$$

$$v_{\mathrm{LAC}^m} = V_{max,\mathrm{LAC}} \left(\frac{\mathrm{LAC}^t}{\mathrm{LAC}^t + K_t} - \frac{\mathrm{LAC}^c}{\mathrm{LAC}^c + K_t} \right) \tag{9.11}$$

with maximum transport rates V_{max} and Michaelis constant K_t. The description of the transport of oxygen is more complicated, as transport is assumed to operate by simple diffusion according to Fick's law (Aubert et al., 2001). Using the permeability P and surface S_c of the blood-brain barrier and following several previous approaches to model

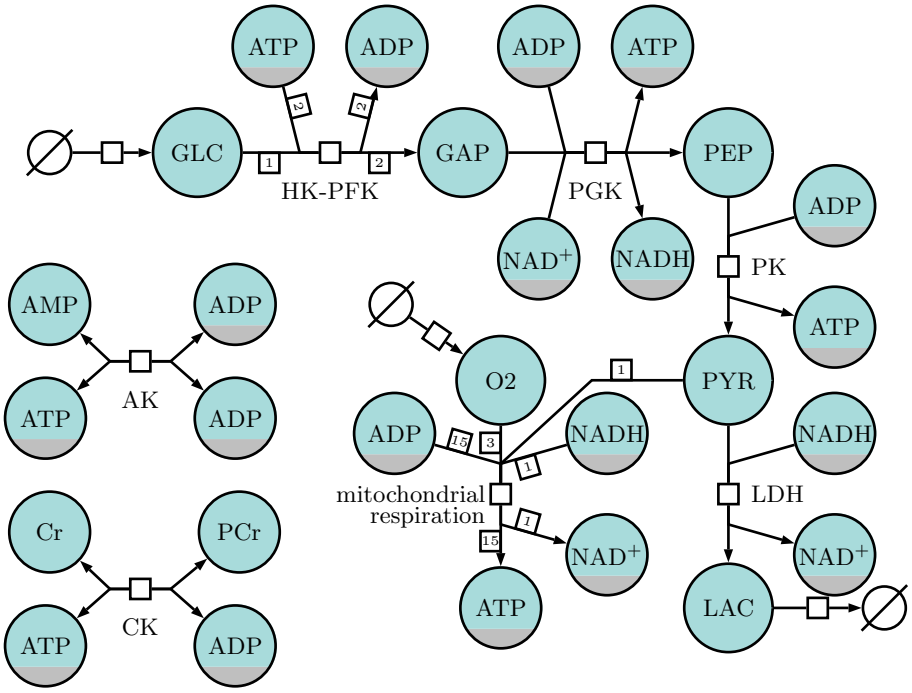

Figure 9.2.: Metabolic reactions considered in the model by Aubert et al. (2001). In addition to the reactions considered by Heinrich and Schuster (1996), the consumption of pyruvate either via transformation into lactate of via the mitochondria is considered.

the transport from blood to the brain, Aubert et al. write

$$v_{\mathrm{O}_2^{\mathrm{m}}} = \frac{P \cdot S_c}{V_n} \left(\frac{K_{\mathrm{O}_2}}{\sqrt[nH]{\frac{Hb \cdot OP}{\mathrm{O}_2^{\mathrm{c}}} - 1}} - \mathrm{O}_2^{\mathrm{t}} \right). \tag{9.12}$$

This description uses the product of hemoglobin concentration by its oxiphoric power ($Hb \cdot OP$), the product of oxygen P_{50} by O_2 solubility (K_{O_2}) and a Hill coefficient (nH). A full derivation of this equation is outside the scope of this work and the interested reader is referred to the description in Aubert et al. (2001), which is based on the work by Vafaee and Gjedde (2000). Equations 9.10, 9.11 and 9.12 are preserved in the models described in the following sections.

Most of the metabolic reactions are modelled via simple mass-action kinetics, with the two notable exceptions of HK-PFK and the mitochondrial respiration.

Compared to the model by Heinrich and Schuster (1996), the rate law for HK-PFK is extended by a term describing its dependence on the availability of glucose using the Michaelis-Menten formalism:

$$v_{\mathrm{HK-PFK}} = k_{\mathrm{HK-PFK}} \cdot \mathrm{ATP} \cdot \left(1 + \frac{\mathrm{ATP}}{K_{I,\mathrm{ATP}}}^{nH} \right)^{-1} \cdot \frac{\mathrm{GLC}_t}{\mathrm{GLC}_t + K_g} \tag{9.13}$$

For the mitochondrial respiration two different hypotheses are compared, of which only the first is relevant for the further discussion. According to this hypothesis, the rate of mitochondrial respiration depends on the availability of the substrates PYR and O_2, again following a Michaelis-Menten kinetics, and on the ATP/ADP ratio following a Hill-type curve:

$$v_{Mito} = V_{max,Mito} \cdot \frac{\mathrm{PYR}}{K_{m,Mito} + \mathrm{PYR}} \cdot \frac{\mathrm{O_2}}{K_{\mathrm{O_2}} + \mathrm{O_2}} \cdot \frac{1}{1 + \left(\frac{\mathrm{ATP}}{\mathrm{ADP} \cdot K_{I,Mito}}\right)^n} \tag{9.14}$$

where $K_{m,Mito}$ and $K_{\mathrm{O_2}}$ are the Michaelis constants of pyruvate uptake and oxygen, respectively. $K_{I,Mito}$ is the inhibition constant, n the Hill coefficient for the regulation by the ATP, ADP ratio.

The model discussed so far allows the analysis of steady state conditions for the extended metabolic network. The most interesting part in the work of Aubert et al. (2001), however, is the coupling of the metabolic network to electric activity of the brain, i.e. neuronal stimulation.

Neuronal stimulation as a disturbance of steady state sodium concentration

The model includes a description of intracellular, i.e. neuronal sodium concentration, which is controlled by three reactions:

(a) the increase in neuronal sodium in response to neuronal stimulation: v_{stim},

(b) sodium leakage through conductance: $v_{Leak-Na^+}$,

(c) and active sodium removal via the sodium/potassium pump: v_{pump}.

The rate laws for the first two reactions are quite different from the metabolic rate laws, as stimulation and leakage do not depend on species concentrations, but on potentials and physical constants. Accordingly, the increase in neuronal sodium is given as

$$v_{stim}(t) = K_{PA} \frac{S_n}{V_n} f_{PA} \tag{9.15}$$

with S_n the neuronal membrane surface, V_n the neuronal intracellular volume, K_{PA} the number of sodium molecules entering the cell per action potential and unit membrane area and f_{PA} the average frequency of action potentials (Aubert et al., 2001).

The leakage current is given as follows:

$$v_{Leak-Na^+} = \frac{S_n}{V_n} \frac{g_{Na}}{F} \left(E_{Na} - V_m\right) \tag{9.16}$$

with S_n and V_n as above, g_{Na} the conductance, F the Faraday constant, E_{Na} the potential and V_m the average membrane potential (Aubert et al., 2001).

The rate law for v_{pump} gives the rate depending on the concentration of its substrate, ATP and Na^+, and is taken again from a model by Heinrich and Schuster (1996, Chap. 5.4.4.4):

$$v_{pump} = \frac{S_n}{V_n} k_{pump} \cdot \mathrm{ATP} \cdot \mathrm{Na}^+ \cdot \left(1 + \frac{\mathrm{ATP}}{K_{m,pump}}\right)^{-1} \tag{9.17}$$

The full model was parameterized using data from previous published models such as the model by Heinrich and Schuster (1996), data from wet-lab experiments published in a wide array of studies and physiological constants, where applicable (Aubert et al., 2001). The authors use their model to simulate a sustained stimulation over 360 seconds and compare the resulting time curves of glucose and lactate concentrations with data obtained from magnetic resonance spectroscopy (MRS) and magnetic resonance imaging (MRI). One major result is the proposed sequence of energy provision, which postulates that at first phosphocreatine is used to generate ATP, afterwards ATP is provided by glycolysis before at last oxidative phosphorylation increases.

Aubert and Costalat 2002 – The metabolic origin of the BOLD signal

The second model published by Aubert and Costalat (2002) was an extension of the model published by the same authors in 2001. While the extent of the metabolic network and the description of the transport processes remained the same as in the previous work (cf. Figure 9.2), this model contains the first coupling of the metabolic network to a description of the venous volume (V_v), given by:

$$\frac{\mathrm{d}V_v}{\mathrm{d}t} = F_{in} - F_{out} \tag{9.18}$$

with

$$F_{in} = \begin{cases} (1 + \alpha_F) \cdot F_0 & \text{for } t_1 \leq t \leq t_{end} \\ F_0 & \text{for } t = 0 \text{ or } t \geq t_{end} + t_1 \end{cases} \tag{9.19}$$

and

$$F_{out} = F_0 \cdot \left(\left(\frac{V_v}{V_{v,0}}\right)^{1/\alpha} + \left(\frac{V_v}{V_{v,0}}\right)^{-1/2} \tau_v \frac{1}{V_{v,0}} \frac{\mathrm{dV}_v}{\mathrm{dt}} \right). \tag{9.20}$$

In the equations above, $V_{v,0}$ denotes the initial venous volume, F_0 stands for the cerebral blood flow at rest and α_F for the fraction by which the cerebral blood flow increases. For the times not accounted for in equation 9.19, the author describes the inflow of blood as a trapezoid, linearly increasing for $0 \leq t \leq t_1$ and linearly decreasing for $t_{end} \leq t \leq t_{end} + t_1$.

α and τ_v are used to parameterize the balloon-like response of the venous volumes to a sudden increase in blood flow with viscoelastic effects.

Equation 9.20 is an exact reproduction of the so–called balloon model, developed by Richard B. Buxton in a series of publications (Buxton and Frank, 1997; Buxton et al., 1998b,a).

Having a description of the venous volume dynamics as well as the oxygen consumption at their hand, the authors used an equation also proposed by Buxton et al. (1998b,a) to describe the change in the concentration of deoxyhemoglobin (dHb):

$$\frac{\mathrm{ddHb}}{\mathrm{d}t} = F_{in}\big(O_2^a - (2 \cdot O_2^c - O_2^a)\big) - \frac{F_{out} \cdot \mathrm{dHb}}{V_v} \tag{9.21}$$

with O_2^a and O_2^c being the arterial and capillary concentration of oxygen, respectively. The final link to functional imaging is made by calculating the BOLD signal using an equation again suggested by Buxton et al. (1998b)

$$\mathrm{BOLD} = V_{v,0} \cdot 7 \cdot \left(1 - \frac{\mathrm{dHb}}{\mathrm{dHb}_0}\right) + 2 \cdot \frac{1 - \frac{\mathrm{dHb}}{\mathrm{dHb}_0}}{\frac{V_v}{V_{v,0}}} + (2 \cdot E_0 - 0.2) + \left(1 - \frac{V_v}{V_{v,0}}\right), \tag{9.22}$$

For a detailed discussion of the equation as well as the integer parameters see (Friston et al., 2000).

With respect to the stimulation, modelled as an inflow of sodium into the neurons, the authors introduced the following description:

$$v_{stim}\,(t) = v_1 + v_2 \frac{t}{\tau_{stim}} e^{-t/\tau_{stim}} \tag{9.23}$$

This equation, the sum of a constant and an alpha function, fits the recorded local field potential as measured by Logothetis et al. (2001).

Aubert and Costalat use their extended model to study the effect of typical stimulation profiles, such as prolonged activation and repetitive activation, on the dynamic profile of the model constituents. They analyse the effect of changes in vascular parameters and the creatine buffering system on the BOLD response by parameter variation, and discuss different hypotheses regarding the regulation of mitochondrial respiration. As a result, they propose their model as "a tool for exploring the relationship between neural activation, energy metabolism and hemodynamics" with an explicit reference to neurodegenerative diseases and brain tumors.

Aubert and Costalat 2005 – The interaction between neurons and astrocytes

The third important publication by the same group of authors focused on the interaction between neurons and astrocytes (Aubert and Costalat, 2005). To simulate these

interactions, the authors extended their previous model (Aubert and Costalat, 2002) and included a description of the energy metabolism in astrocytes. Glycolysis and mitochondrial respiration in astrocytes are modelled using the same equations previously used only in neurons. To model the differences in location and therefore supply with glucose, the model also features an "extracellular space" compartment. While astrocytes can take up glucose directly from the capillaries, neurons rely on glucose from the extracellular space. Lactate, which is produced by both astrocytes and neurons can be shuttled into the extracellular space and is then transported into the capillaries where it is removed by the blood flow. Transport between the compartments is described using symmetric facilitated transport, e.g. the exchange of glucose between the capillaries and the extracellular space is described by the following equation:

$$v_{Glc}^{ce} = V_{max} \cdot \left(\frac{\mathrm{Glc}^c}{\mathrm{Glc}^c + K_{Glc}^{ce}} - \frac{\mathrm{Glc}^e}{\mathrm{Glc}^e + K_{Glc}^{ce}} \right) \tag{9.24}$$

This model also introduces the relative volumes for neurons ($V_n = 0.45$), astrocytes (glia cells, $V_g = 0.25$), the extracellular space ($V_e = 0.2$), capillaries ($V_c = 0.0055$) and veins ($V_v = 0.0237$), which are a feature of all other models presented later. The model is

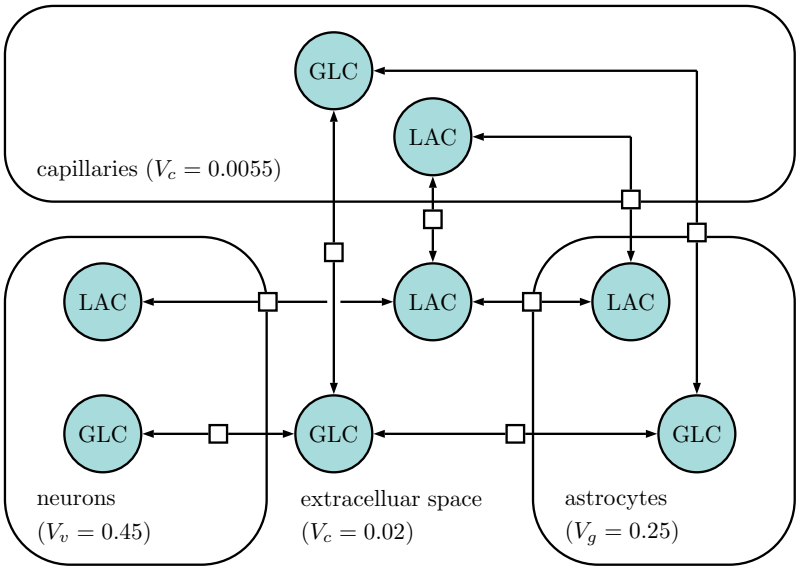

Figure 9.3.: Compartments and exchange reactions for glucose and lactate considered in the model by Aubert and Costalat (2005). This model is the first model that included an explicit description of the interactions between neurons and astrocytes. The volumes are relative volumes with respect to the total tissue volume.

used to analyse the interactions between astrocytes in neurons in response to neuronal stimulation. In particular, the authors analyse the conditions under which the astrocyte-neuron lactate shuttle (ANLS, cf. Section 8.5) is active. Using hypotheses about the steady

state fluxes which the authors deem unfavorable for the occurrence of ANLS, Aubert and Costalat observe production of lactate by astrocytes and simultaneous uptake of lactate by neurons. The resulting dynamic profile of extracellular lactate is compared with experimental finding. As a result, the authors conclude that the available data are compatible with the notion of an ANLS.

9.3. Cloutier 2009 – Neurotransmitter cycling and the role of glycogen in astrocytes

Four years after the publication of the model described above, Cloutier et al. (2009) presented a model of brain energy metabolism that went beyond the earlier models. In their paper *"An integrative dynamic model of brain energy metabolism using in vivo neurochemical measurements"*, the authors extended the Aubert (2005) model to include a description of glycogen storage in astrocytes and the coupling of neurons and astrocytes via neurotransmitter cycling. The latter is of special importance, as it links ATP consumption in both cell types (Figure 9.4, p86). The inclusion of glycogen lead to the

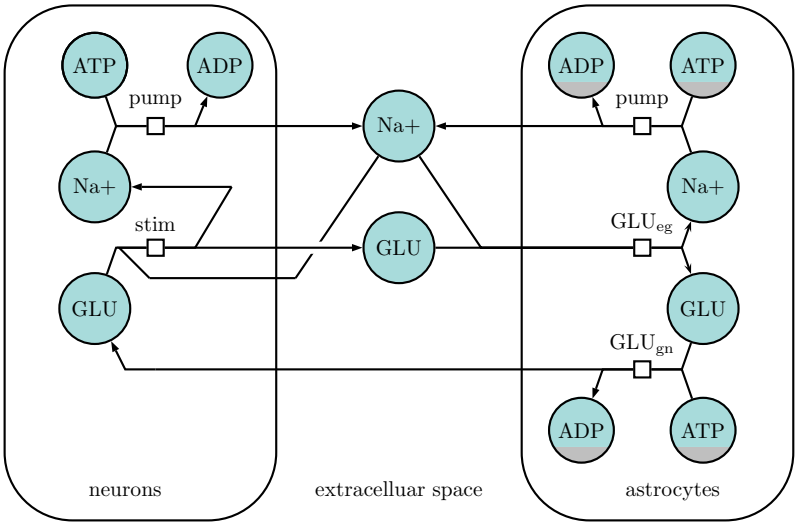

Figure 9.4.: Coupling of energy consumption in neurons and astrocytes through neurotransmitter cycling as implemented in the model by Cloutier et al. (2009). Stimulation results in the release of glutamate from neurons to the extracellular space and occurs simultaneous to the uptake of extracellular sodium ions by neurons (stim). Extracellular glutamate is taken up by astrocytes with the co-transport of sodium ions (GLU_{eg}). Conversion of glutamate to glutamine is not considered, instead glutamate is shuttled back to neurons (GLU_{gn}). Inflow of sodium ions activates sodium-potassium pumps which require ATP to remove sodium from the cells (pump).

requirement to model the concentration of glucose 6-phosphate, which has not been con-

sidered explicitly in earlier models. The mathematical description used to describe the hexokinase-phosphofructokinase part of the glycolytic pathway have, therefore, been replaced by three consecutive reactions leading from glucose to glyceraldehyde 3-phosphate. These three reactions are catalysed by hexokinase, phosphoglycerate isomerase and phosphofructokinase, respectively. While the general structure of the model is taken from previous publications, the model parameters were calibrated using *in vivo* measurements of extracellular glucose and extracellular lactate from mice during stimulation. As a result, not only the model parameters differ from previous publications, but also the steady state values of the different metabolites are altered. Consequently, the authors do not portray their results as relevant for neuroimaging, but emphasize the "descriptive capacity" of the model and its ability of "integrate available knowledge" of brain energy metabolism.

9.4. Other models

Besides the models discussed so far, there have been several other models which are worth mentioning, even if they are not direct ancestors of my own model. One of those models is another important work published by Aubert et al. (2007). This publication contains a modified version of the model from 2005 (Aubert and Costalat, 2005). On one hand, the model presents a drastic decrease in the level of detail compared to the previous models. The glycolytic pathway, for example, is modelled as a single reaction, e.g. only glucose and pyruvate are considered. On the other hand, this model introduces for the first time the need for NADH to be shuttled into the mitochondria and the dependence of many of the previously considered transport mechanism on proton concentrations.

Another notable contribution came from Tiveci et al. (2005). This model is special in that it has been developed and analysed with the influence of AD-driven alterations in the blood flow on the BOLD signal in mind. The authors use the model from Aubert and Costalat (2002) and extend it with a description of calcium dynamics presented by Grubelnik et al. (2001). The only AD-driven alteration analysed in this publication is the decrease of the cerebral blood flow increase fraction α_F (Equation 9.2, p83).

10. Construction and implementation of a new model of brain energy metabolism and the hemodynamic response

The mathematical models described in the previous chapter were all constructed for a specific purpose. In contrast to the mathematical models of protein aggregatation, discussed in Part I, this purpose was not the understanding of available experimental data. Instead, the models aimed at building mechanistic descriptions of the underlying biochemical processes. To decide, whether these models can also be used to answer the research questions, it is necessary to refine the requirements for the model, defined in Section 7.4.

10.1. Comparison of the available models with the compiled requirements

The first of the requirements is the ability of the model to describe the healthy state. Based on the description of the main pathways of energy metabolism in the brain as described in Chapter 8, it can be rewritten to require the model to

- describe the main pathways on energy metabolism, i.e. glycolysis, the TCA-cycle and the pentose phosphate pathway at the healthy state.

The second requirement is that the model is detailed enough to analyse the reported alterations (cf. Section 8.6). These alterations affect the expression of enzyme levels as well as changes in the composition of brain tissue. The model needs to be able to deal with both, i.e. it needs to

- be detailed enough to reflect changes in individual enzymes in the glycolytic pathway and in the pentose phosphate pathway, and
- contain a description of the metabolic interactions between astrocytes and neurons, to allow an analysis of the impact of astrocyte hyperplasia and hypertrophy.

The third requirement concerns the quantification of the impact of the different AD-related changes on a chosen measure of outcome. Given the aim of improving the analysis of BOLD fMRI data, this means that the model needs to

- include a description of neuronal activity to evoke a hemodynamic response, and
- allow a quantification of the impact of the observed changes the BOLD signal.

None of the models described in the previous chapter fulfils all of these requirements. The healthy state, i.e. the situation without any disease-related alterations is probably best approximated by the model of Aubert and Costalat (2005), with the steady state value of all metabolites being in good alignment with experimentally obtained values.

With respect to the second requirement, the ability to model AD-related alterations, the situation is more difficult. None of the models contains a description of the pentose phosphate pathway, whose activity is increased in Alzheimer's disease. Moreover, only the model by Cloutier et al. (2009) contains a description of the first steps of the glycolytic pathway, which is required to analyse the influence of the observed increase in enzyme activity. The equations and parameters used to describe these steps, however, lead to physiologically not meaningful steady state values for the affected metabolites.

Astrogliosis, i.e. an increase in number and volume of astrocytes, can only be modelled if there is a distinction between cerebral cell types, and if the interactions between these cell types are considered. The model which comes closest to this ideal is the model by Cloutier et al. (2009), which not only contains compartments for both cell types, but also a detailed description of neuron-astrocytic interaction.

To satisfy the last requirement, the model needs to contain a description of the BOLD signal. This is true for the models by Aubert and Costalat (2002) and Aubert and Costalat (2005).

In summary, to really account for the different alterations observed in AD, a new model is needed that comprises features from several of the established models as well as new components. Construction and implementation of this model are described in the next sections.

10.2. Compartments, transport reactions and energy metabolism

The new model describes the compartmentalized pathways of energy metabolism that convert glucose through various intermediates into ATP and water. The arterial con-

centrations of glucose, oxygen, lactate and carbon dioxide are used as fixed boundary conditions.

Compartments and transport reactions

The model uses the compartmentalization proposed by Aubert and Costalat (2005) with five compartments having a fixed volume (arteries, capillaries, neurons, astrocytes, extracellular space) and one compartment having a dynamic volume (veins) (cf. Section 9.2, Equation 9.24 and Figure 9.3). The change in the venous volume is included to account for the increase in blood volume as a response to neuronal excitation. All initial compartment sizes are taken from Aubert and Costalat (2005).

Transport of glucose, lactate and oxygen is modelled with equations and parameters used by Aubert and Costalat (2005). This leads to steady state concentrations for these three metabolites that are close to experimental findings. The same approach is used for the transport of carbon dioxide, a feature taken from Cloutier et al. (2009). To model the close interaction of neurons and astrocytes, I apply the description of sodium transport and neurotransmitter cycling used by Cloutier et al. (2009) (cf. Figure 9.4). An overview of the different compartments and their connection via transport reactions is shown in Figure 10.1. This figure also shows the sodium and glutamate exchange reactions that will be used to describe neuronal stimulation. The full list of equations for these reactions together with the respective parameter values can be found in the appendix, Table C.3.

The glycolytic pathway

The glycolytic pathway is considered in astrocytes and neurons. To allow the analysis of the observed changes in glycolytic enzymes (Bigl et al., 1996, 1999), a detailed description of the reactions catalysed by hexokinase and phosphoglycerate kinase is needed. While the model by Cloutier et al. (2009) already contains a description of these reactions, the equations and parameters chosen by the authors are not fully in line with available information about the underlying reaction mechanisms. In particular, the rate law for hexokinase does not allow the incorporation of the inhibition constant for the substrate inhibition by G6P (cf. Section 8.1). I therefore removed the equations for these two reactions, and inserted a description previously employed by Heinrich and Schuster (1996, p173ff):

$$v_{\mathrm{HK}} = k_{\mathrm{HK}} \cdot \mathrm{ATP} \left(1 + \frac{\mathrm{G6P}}{K_{I,\mathrm{G6P}}}\right)^{-1} \tag{10.1}$$

$$v_{\mathrm{PGI}} = k_{\mathrm{PGI},f} \cdot \mathrm{G6P} - k_{\mathrm{PGI},r} \cdot \mathrm{F6P} \tag{10.2}$$

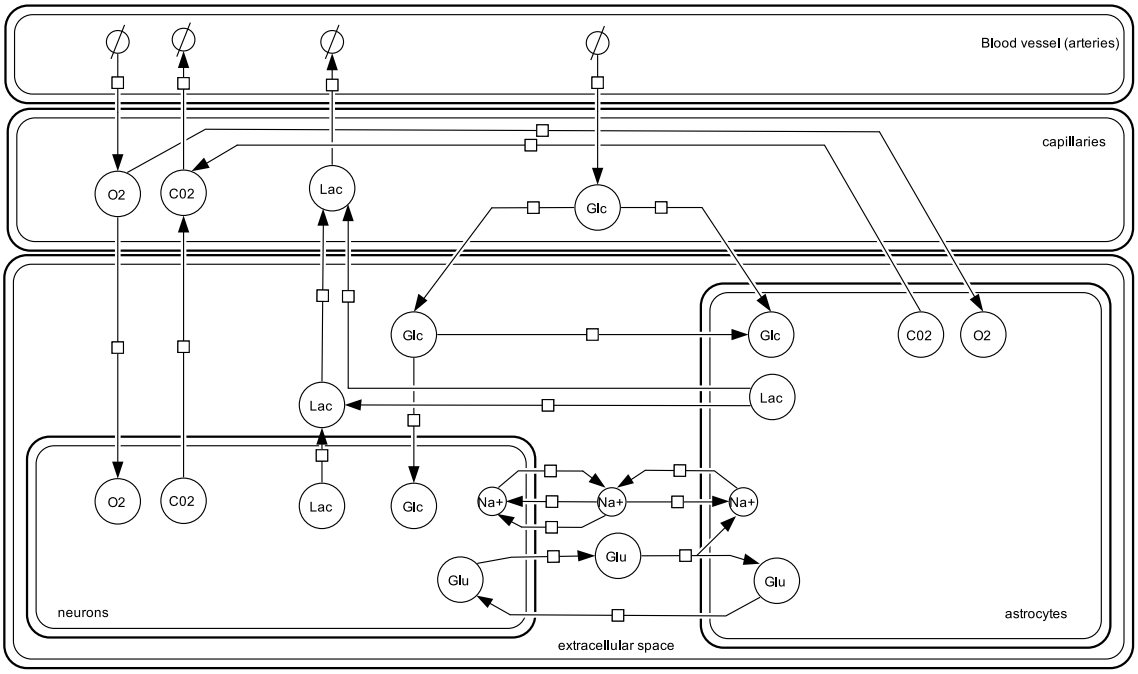

Figure 10.1.: Overview of the different transport and exchange reactions considered in the model. For glucose, lactate, oxygen and carbon dioxide the arrows indicate flux at steady state. The figure is a reproduction of Figure 1 in (Winter et al., 2017).

$K_{I,\mathrm{G6P}}$ is the inhibition constant and $k_{\mathrm{HK}}, k_{\mathrm{PGI},f}$ and $k_{\mathrm{PGI},r}$ are rate constants. All parameter values are given in the appendix (Table C.2 and Table C.1). The next three reactions of the glycolytic pathway, catalysed by PFK, ALD and TPI (cf. Fig 8.1, p66) are collectively described by a single rate law:

$$v_{\mathrm{PFK}} = k_{\mathrm{PFK}} \cdot \mathrm{ATP} \cdot \left(1 + \left(\frac{\mathrm{ATP}}{K_{I,\mathrm{ATP}}}\right)^{nH}\right)^{-1} \cdot \frac{\mathrm{F6P}}{\mathrm{F6P} + K_{m,\mathrm{F6P}}} \tag{10.3}$$

with $K_{m,\mathrm{F6P}}$ the Michaelis constant, nH a Hill coefficient $K_{I,\mathrm{ATP}}$ the inhibition constant and k_{PFK} the rate constant.

The subsequent conversion of GAP to PEP via three consecutive reactions is again described by a single rate law, a procedure already applied by Aubert et al. (2001); Aubert and Costalat (2002, 2005) and Cloutier et al. (2009) (cf. Figure 9.2).

$$v_{\mathrm{PGK}} = k_{\mathrm{PGK}} \cdot \mathrm{GAP} \cdot \mathrm{ADP} \cdot \frac{\mathrm{NAD}}{\mathrm{NADH}} \tag{10.4}$$

with k_{PGK} as rate constant. The final reaction in the glycolytic pathway, the conversion of phosphoenolpyruvic acid to pyruvic acid, is described by an individual rate law:

$$v_{\mathrm{PK}} = k_{\mathrm{PK}} \cdot \mathrm{PEP} \cdot \mathrm{ADP}, \tag{10.5}$$

with k_{PK} as rate constant.

The regulation constants for Equations 10.1 to 10.5 have been set to values proposed by Heinrich and Schuster (1996) and Aubert et al. (2001) and are identical in neurons and astrocytes. Rate constants for all reactions have been adjusted to guarantee physiological meaningful steady state concentrations sampled from the literature. The ratio of rate constants between neurons (Table C.2) and astrocytes (Table C.1) is motivated by the corresponding ratio used by Aubert and Costalat (2005).

TCA cycle and oxidative phosphorylation

The complex pathways of the TCA cycle and oxidative phosphorylation are described with a single reaction:

$$v_{\mathrm{Mito}} = V_{\mathrm{max}} \cdot \frac{\mathrm{PYR}}{\mathrm{PYR} + K_{m,\mathrm{PYR}}} \cdot \frac{\mathrm{ADP}}{\mathrm{ADP} + K_{m,\mathrm{ADP}}} \cdot \frac{\mathrm{O_2}}{\mathrm{O_2} + K_{m,\mathrm{O_2}}} \cdot \left(1 - \frac{1}{1 + e^{-5 \cdot \left(\frac{\mathrm{ATP}}{\mathrm{ADP}} - 20\right)}}\right). \tag{10.6}$$

V_{max} is the maximal velocity and $K_{m,\mathrm{PYR}}, K_{m,\mathrm{ADP}}$ and $K_{m,\mathrm{O_2}}$ are Michaelis constants. This description is taken from Cloutier et al. (2009) and accounts for the dependence on PYR, O_2 and ADP as well as the inhibition at high levels of energy (i.e. a high ATP/ADP ratio). The assumed stoichiometry for this reaction is:

$$1 \cdot \mathrm{PYR} + 3 \cdot \mathrm{O_2} + 15 \cdot \mathrm{ADP} + 1 \cdot \mathrm{NADH} \rightarrow 15 \cdot \mathrm{ATP} + 1 \cdot \mathrm{NAD+} + 3 \cdot \mathrm{CO_2}$$

i.e. 15 molecules of ATP are produced for one molecule of pyruvate and one molecule of NADH shuttled into the mitochondria. The same stoichiometric factors have been used in all models discussed earlier.

10.3. Construction of a detailed model of the reactions of the pentose phosphate pathway

The pentose phosphate pathway (PPP) has not been considered in earlier models, and its inclusion is one of the major contributions of the work presented here. To achieve a physiologically meaningful description of the reactions comprising the PPP (cf. Section 8.3) I chose to use an approach developed by Stanford et al. (2013) to generate kinetic models. This approach consists of several stages, which for the ease of presentation are here condensed into two consecutive steps:

- The generation of a skeleton ("scaffold") model of generic rate laws which are able to describe a vast array of dynamics,

- The calculation of thermodynamically meaningful parameters sets for each equation and for the whole network based on available (experimental) data.

While the method by Stanford et al. (2013) also includes the generation of flux data from flux balance analysis, this is not part of the work presented here.

To describe the dynamics of the individual reactions, I follow the approach by Stanford et al. (2013), and use the *common modular rate law* for all reactions of the PPP. The common modular rate law is "a generalized form of the Michaelis-Menten kinetics that applies to any reaction stoichiometry" (Liebermeister et al., 2010). This rate law has at least two interchangeable notations. The first notation, as used in (Liebermeister et al., 2010) uses enzyme levels (u) as well as forward and backward rate constants (k^+, k^-), whereas the second notation, applied by Stanford et al. (2013) uses the parameters V_{max} and K_{eq} instead. For a simple bimolecular reaction $A + B \Leftrightarrow 2C$, the first notation would read:

$$v = u \cdot \frac{k^+ \cdot \frac{A}{k_A^M} \cdot \frac{B}{k_B^M} - k^- \cdot (\frac{C}{k_C^M})^2}{(1 + \frac{A}{k_A^M})(1 + \frac{B}{k_B^M}) + (1 + \frac{C}{k_C^M})^2 - 1}$$

with enzyme level u, forward rate constant r^+, reverse rate constant r^- and Michaelis constants k_A^M, k_B^M and k_C^M. Conversion between the two notations is trivial, an example is given in Appendix B. I use the first notation as it corresponds to the equations used to describe the glycolytic pathway.

The skeleton model of the PPP included all reactions depicted in Figure 8.4. Water (H2O) and hydrogen ions (H+) are not included in the description of the second reaction, as both are considered to be abundant. This is in line with other kinetic models of the pentose phosphate pathway, e.g. by Messiha et al. (2014). This skeleton model was encoded in COPASI 4.16 (Hoops et al., 2006) and exported as SBML L2V1 (Hucka et al., 2003).

Parameter balancing

To achieve a physiologically and thermodynamically meaningful parametrization, I collected available data from several sources:

- Equilibrium constants were calculated using the eQuilibrator webservice[1] provided by the Milo Lab at the Weizmann Institute[2] (Flamholz et al., 2012),

- Michaelis constants were collected from SabioRK database (Wittig et al., 2012),

[1] http://equilibrator.weizmann.ac.il
[2] http://www.weizmann.ac.il/plants/Milo

- Initial concentration for G6P, F6P and GAP were taken from the steady state solution of my model without the PPP,
- Initial concentrations for all other species were set to the mean value of all metabolites in my model without the PPP.

The assembled data were stored as an SBTab file (Lubitz et al., 2016). A tabular representation can be found in Table 10.1.

Table 10.1.: Values from databases and publications used to provide an initial guess for the parameter balancing routine

Quantity Type	Reaction ID	Species	Value	Reference
equilibrium constant	R01056		0.457	eQuilibrator
equilibrium constant	R01528		170	Joshi and Palsson (1989)
equilibrium constant	R01529		3.91	eQuilibrator
equilibrium constant	R01641		0.216	eQuilibrator
equilibrium constant	R01827		1.34	eQuilibrator
equilibrium constant	R01830		0.01777	eQuilibrator
equilibrium constant	R02035		4.7e+03	eQuilibrator
equilibrium constant	R02736		2.56	eQuilibrator
concentration		G6L	0.45366	sampled from glycolytic species
concentration		G6P	0.1	from glycolysis model
concentration		NADP	0.45366	sampled from glycolytic species
concentration		NADPH	0.45366	sampled from glycolytic species
concentration		P6G	0.45366	sampled from glycolytic species
concentration		Ru5P	0.45366	sampled from glycolytic species
concentration		X5P	0.45366	sampled from glycolytic species
concentration		R5P	0.45366	sampled from glycolytic species
concentration		GAP	0.0056	from glycolysis model
concentration		S7P	0.45366	sampled from glycolytic species
concentration		E4P	0.45366	sampled from glycolytic species
concentration		F6P	0.1091	from glycolysis model
Michaelis constant	R02736	NADP	3.0e-05	SabioRK
Michaelis constant	R02736	G6P	6.9e-05	SabioRK
Michaelis constant	R02736	NADP	1.2e-05	SabioRK
Michaelis constant	R01528	P6G	3.0e-05	SabioRK
Michaelis constant	R01528	P6G	4.0e-05	SabioRK
Michaelis constant	R01641	X5P	1.5e-04	SabioRK
Michaelis constant	R01641	R5P	0.0017	SabioRK

The second step of the approach is the calculation of thermodynamically meaningful sets of parameters via *parameter balancing*. Parameter balancing is a method that "exploits

the thermodynamic dependencies among different biochemical quantities to guess realistic model parameters from available kinetic data" (Lubitz et al., 2010). I used an implementation of this method provided as part of the semanticSBML platform[3]. Using the SBML file of the model and the SBTab file of the assembled data as input, the method produced a full set of parameters for all eight reactions.

To include this description of the PPP into my model, two additional steps were necessary.

Calculation of a steady state flux

To calculate a steady state flux, three additional reactions have been included in the model. First, to allow for regeneration of NADP, a simple conversion of NADPH to NADP was included. Second, to account for the removal of GAP from the pathway to as a result to the coupling to the glycolytic pathway, a reaction modelling a GAP sink was introduced. The third addition was the inclusion of a R5P sink to model its contribution to biosynthesis. In addition to these three new reactions, the concentration of G6P was fixed to its concentration in the model without the PPP branch. This was done to ensure that after coupling of both pathways the steady state concentration in the glycolytic pathway is not affected. The steady state was calculated using COPASI 4.16 with the default parameters of the algorithm as implemented in COPASI. The resulting fluxes are listed in Table 10.2.

Table 10.2.: Resulting fluxes for the PPP after parameter balancing and steady state calculation.

Reaction	Enzyme	Flux (mmol/ml)
G6P + NADP ⇔ G6L + NADPH	G6PDH	0.441237
G6L ⇔ P6G	6PGL	0.441237
P6G + NADP ⇔ Ru5P + NADPH	GND	0.441237
R5P ⇔ X5P	RPE	0.294158
R5P ⇔ Ru5P	RKI	0.147079
GAP + S7P ⇔ X5P + R5P	TKL-1	0.147079
GAP + S7P ⇔ F6P + E4P	TAL	0.147079
F6P + GAP ⇔ X5P + E4P	TKL-2	-0.147079

[3] https://semanticsbml.org

Enzyme rescaling

The amount of flux through the PPP in healthy steady state is assumed to be about 6 per cent of the total flux through the first reaction in glycolysis (taken from Holzhütter (2004)), which is close to experimental findings for the flux distribution in adult brain tissue (Wamelink et al., 2008). To integrate the pentose phosphate pathway in both astrocytes and neurons in the existing models, the fluxes needed to be adjusted so that the overall flux pattern follows these physiologically meaningful distribution. In addition, the reactions described by v_{PGI} and v_{PFK} and ATPase needed to be adjusted to obtain the same overall steady state flux in the model including the PPP and in the model without the PPP. To achieve this, I applied *enzyme rescaling*, a method developed for metabolic engineering (Kholodenko et al., 1998). The resulting fluxes for the relevant reactions in neurons and astrocytes are listed in Table 10.3. The scaled reactions of the PPP were

Table 10.3.: Resulting fluxes for the PPP in neurons and astrocytes after enzyme rescaling.

		Flux (mmol/ml)	
Reaction	Enzyme	Neurons	Astrocytes
G6P + NADP ⇔ G6L + NADPH	G6PDH	0.000186768	9.25373E-05
G6L ⇔ P6G	6PGL	0.000186768	9.25373E-05
P6G + NADP ⇔ Ru5P + NADPH	GND	0.000186768	9.25373E-05
R5P ⇔ X5P	RPE	0.000124512	6.16815E-05
R5P ⇔ Ru5P	RKI	6,2256E-05	3.08458E-05
GAP + S7P ⇔ X5P + R5P	TKL-1	6,2256E-05	3.08458E-05
GAP + S7P ⇔ F6P + E4P	TAL	6,2256E-05	3.08458E-05
F6P + GAP ⇔ X5P + E4P	TKL-2	-6,2256E-05	-3.08458E-05

then connected to the description of the glycolytic pathway. Figure 10.2 shows the final set of metabolic reactions considered in both astrocytes and neurons[4].

10.4. Neuronal stimulation and the BOLD response

Neuronal stimulation is described as a combination of (a) release of glutamate from neurons into the extracellular space, coupled with an influx of sodium from the extracellular space to the neurons, (b) an increase in the cerebral blood flow. These two concepts are modelled as follows:

[4] A map of the full model can be found on the inner back cover of this book.

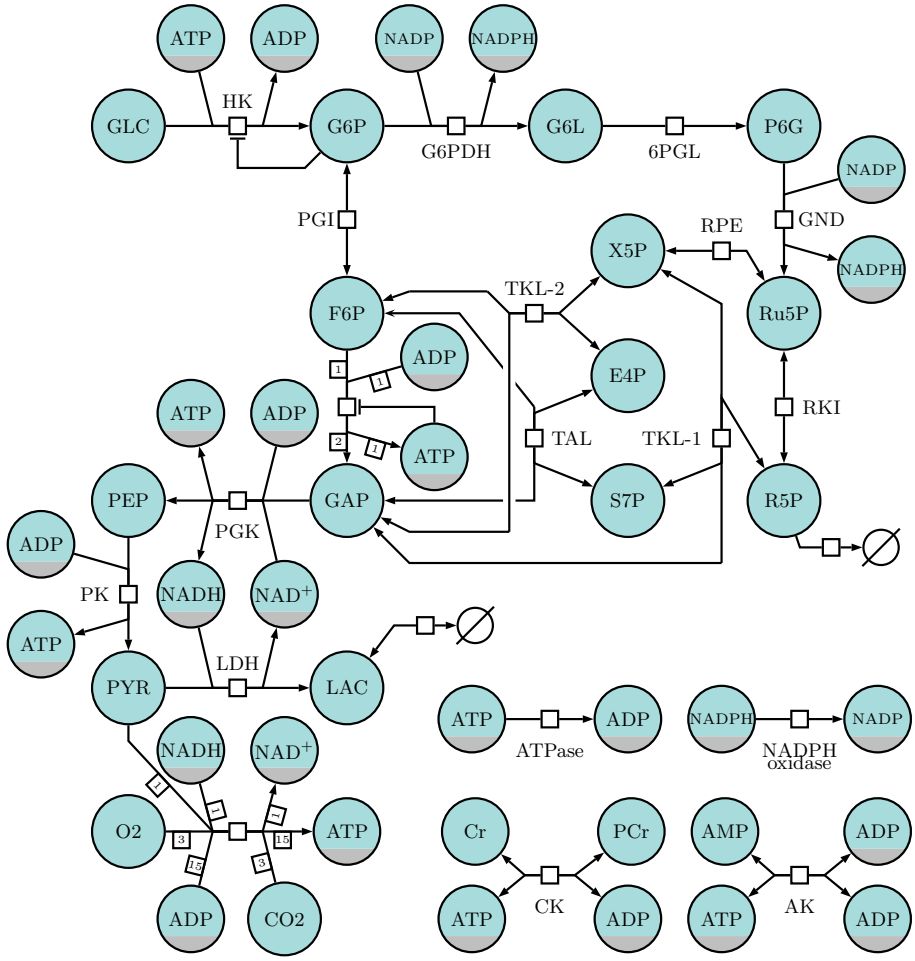

Figure 10.2.: Metabolic network considered in both neurons and astrocytes. Glycolysis and the pentose phosphate pathway are modelled in detail, whereas the TCA-cycle and oxidative phosporylation are described by a single process.

(a) The description of the increase in sodium influx follows an approach taken by Aubert and Costalat (2002). The stimulation is described as the sum of a constant term and a gamma function:

$$v_{\text{stim}}(t) = v_1 + v_2 \frac{(t - t_0)}{t_{\text{stim}}} e^{\frac{-(t-t_0)}{t_{\text{stim}}}} \tag{10.7}$$

with $v_1 = 0.041$, $v_2 = 1.44$, $t_0 = 200$ and $t_{\text{stim}} = 2$ (Cloutier et al., 2009). This setup is in line with the notion of habituation of neuronal activity and has be mapped to time courses of local field potential published by Logothetis et al. (2001). The increase in neuronal sodium is coupled to the increase in extracellular glutamate which initiates the neurotransmitter cycling.

(b) The increase in blood flow is described as a bistable switch:

$$f_{\mathrm{CBF}} = \Delta_F \cdot \left(\frac{1}{(1 + e^{\alpha(t-(t_0+t_1-\delta)))}} - \frac{1}{(1 + e^{\alpha(t-(t_0+t_1+t_{\mathrm{end}}+\delta))})} \right) \tag{10.8}$$

with $F = 0.42$, $\alpha = -4.59$, $t_0 = 200$, $t_1 = 2$, $t_{\mathrm{end}} = 40$ and $\delta = 3$, which is in line with the description in Cloutier et al. (2009). The increased blood flow influences the size of the venous compartment via $F_{in} = F_0 + f_{CBF}$ (cf. Equation 9.18). The resulting venous volume is depicted in Figure 10.3, panel B.

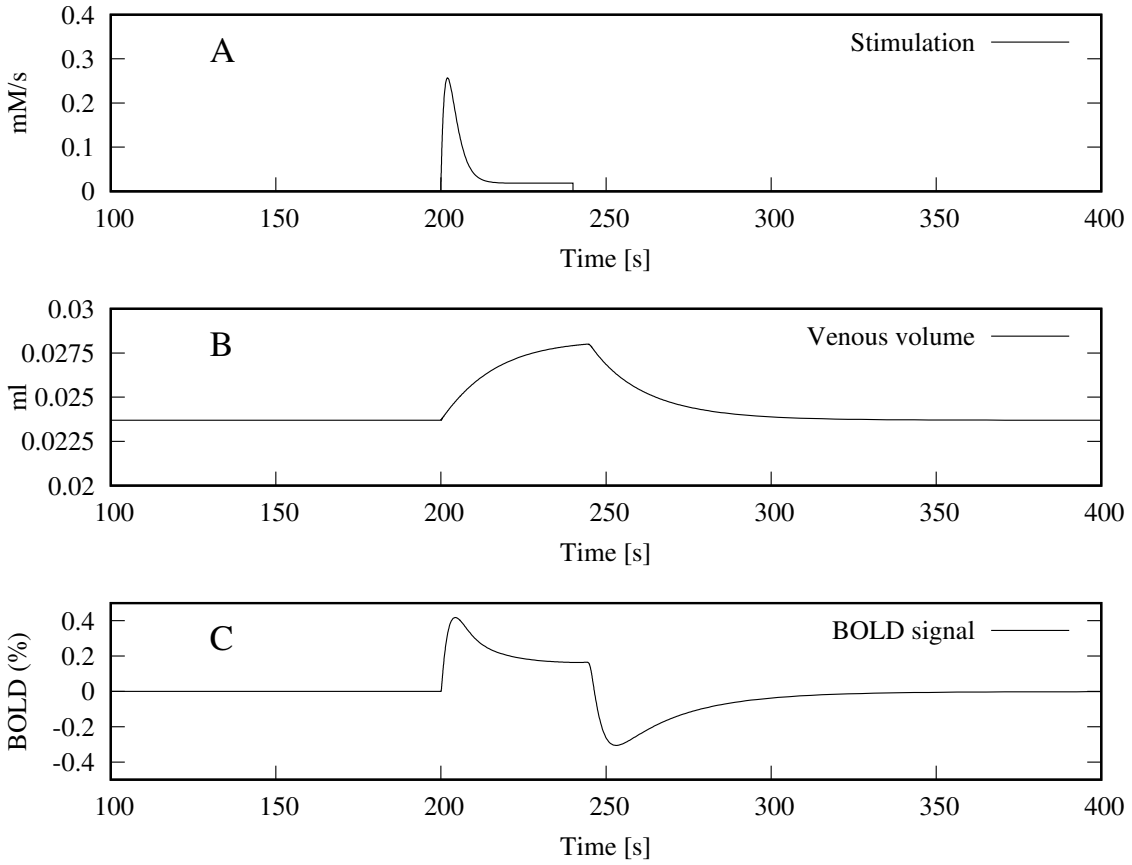

Figure 10.3.: Time course of dynamic input applied to metabolic model (Panel A), venous volume (Panel B) and the resulting BOLD signal (Panel C) at conditions modelling the healthy state.

The increase in neuronal sodium as a result of the stimulation and the increase in astrocytic sodium in response to glutamate uptake drive the sodium exchange system away from its steady state solution. This leads to an activation of the sodium pumps which transport sodium from neurons and astrocytes towards the extracellular space, thereby consuming ATP. The ATP pool is subsequently replenished by an increased activity of the metabolic network, which leads to concentration changes of capillary oxygen, visible in the dynamic profile of dHb. The time evolution of the dHb concentration is governed by the following

equation which describes its dependency on arterial and capillary oxygen concentration (O_2^a and O_2^c, respectively).

$$\frac{\mathrm{d}\,\mathrm{dHb}}{\mathrm{d}t} = F_{in}\left(O_2^a - (2 \cdot O_2^c - O_2^a)\right) - \frac{F_{out} \cdot \mathrm{dHb}}{V_v} \tag{10.9}$$

with F_{in} describing the flow into the venous compartment, F_{out} the outflow of the venous compartment and V_v the venous volume.

BOLD response

The BOLD response is calculated in dependence of the venous volume and the change in deoxygenated hemoglobin (dHb) with the following equation:

$$\mathrm{BOLD} = V_{v,o} \cdot 7 \cdot \left(1 - \frac{\mathrm{dHb}}{\mathrm{dHb}_0}\right) + 2 \cdot \left(1 - \frac{\mathrm{dHb}}{\mathrm{dHb}_0}\right) / \left(\frac{V_v}{V_{v,0}}\right) + (2 \cdot E_0 - 0.2) + \left(1 - \frac{V_v}{V_{v,0}}\right) \tag{10.10}$$

which is taken from Friston et al. (2000). This equation has been used by Aubert et al. (2001) before. The resulting shape (Figure 10.3, Panel C) compares well to the shape reported in other modelling studies (Aubert et al., 2001; Aubert and Costalat, 2005; Aubert et al., 2007).

10.5. Implementation of the model using COPASI

The model has been implemented by hand using different versions of COPASI (Hoops et al., 2006). COPASI is an open-source software for biochemical system simulation whose development is shared between the Biocomplexity Institute of Virginia Tech, the University of Heidelberg, and the University of Manchester. It is available free of charge from www.copasi.org. I chose to use it for the project for several reasons:

Due to its intended use as a simulator for biochemical systems, COPASI offers a straightforward way to encode compartments, species, and reactions. While the software provides several predefined rate-laws, such as simple mass-action kinetics, Michaelis-Menten kinetics or different types of allosteric regulations, it also allows to define custom rate laws. COPASI integrates a vast array of methods for model analysis, including the numerical calculation of steady states, Metabolic Control Analysis, Sensitivity Analysis, Time Series Analysis and several algorithms for optimization and parameter value estimation. In addition to a graphical user interface, COPASI also offers an API that allows to integrate its model construction and analysis features into other programs. I have used this facility for the implementation of the research pipeline described below.

Additional reasons for the choice of COPASI for the implementation of the model are its comprehensive support of community standards for model exchange (SBML) and simulation experiment description (SED-ML) and the helpful and friendly user community.

With the exception of transport reactions that connect different compartments, all model equations, as given in Appendix C, can be directly encoded in the default way in COPASI. For transport reactions, the rate laws need to be written using user-defined kinetics. The reason for this difference between metabolic and transport reactions is the way COPASI translates the entered reactions into differential equations. For reactions that occur in a single compartment, COPASI automatically creates rate laws that depend on the concentration of the species. For reactions that connect different compartments, COPASI creates rate laws that depend on the amount (i.e. particle numbers) of species and does not consider the volumes. A detailed description of the consequences and the required actions arising from this difference can be found in Appendix D.

While I started encoding with COPASI release 4.16 (Build 104) the complexity of the model as well as the discovery of several bugs in the software made it necessary to work with a development build made available by the COPASI developers. For a reproducible simulation of the final version of the model at least COPASI 4.19 (Build 140) is required.

Inclusion into a VPH-Share Workflow

Inside the "VPH DARE@IT" project, the model is part of a pipeline that uses patient-specific data to calculate personalized parameters for the canonical hemodynamic response function. The pipeline is described in Section 7.5. The last part of the pipeline consists of a workflow, that uses information about the disease-state of a patient as well as measurements of blood glucose and blood oxygen concentration to parameterize the kinetic model presented above. The workflow consists of several steps, that have been implemented as individual executables and are run successively. For the first step in the workflow, the calculation of a steady that based on the given patient data, a time-independent version of the model is needed as the calculation of steady states for time-dependent models is prohibited by COPASI. In a second step, the time-dependent parts of the model are added. The third step in the workflow is the simulation of the model and calculates the three shape characteristics of the resulting BOLD signal. The characteristics are compared to their respective value at healthy conditions the deviations are calculated. In a fourth step the parameters of the canonical HRF are optimized so that the resulting shape of the HRF shows the same deviation in the three shape parameters as calculated for the BOLD signal in step three. The last step in the workflow is the calculation of the shape of the hemodynamic response function with the new set of parameters and its comparison with

the canonical HRF. The result is presented to the user of the workflow as an image. An example is shown in Figure 10.4.

Table 10.4.: Name and purpose of the executables of the workflow

Name of the executable	Purpose
vph_ss	This executable loads a generic kinetic model in the COPASI data format (`generic.cps`) and substitutes the value of different metabolites with values taken from the command line (if any are present). It then calculates a steady state for this model and sets all values that are numerically close to zero to zero. The model in steady state is saved as `m_ss.cps`
vph_modComp	This executable loads the model from `m_ss.cps` and adds the time-dependent model components, i.e. the venous volume change, the change in cerebral blood flow and the stimulation. The complete model is saved as `m_kin.cps`.
vph_simulate	This executable loads the complete kinetic model and performs a time-series simulation from $t = 0s$ to $t = 250s$. The resulting shape of the BOLD signal is used to calculate its peak time, peak height and full width at half maximum (FWHM).
vph_optim	The three shape characteristics of the BOLD signal as calculated by vph_simulate are used by this program to calculate optimized parameters of the canonical HRF. For this purpose, the deviation of the three values of the simulated model from the values for the original model are computed. Subsequently, the parameters of the canonical HRF are optimized so that the peak height, peak time and FWHM of the calculated HRF have the same deviation with respect to its standard parametrization.
vph_hrf	The last executable in the workflow uses the optimized parameters calculated by vph_optim to simulate the patient-specific time course of the canonical HRF.

All executables have been implemented in C++ using the GNU toolchain and the COPASI C++ API. The model has been deployed together with the software needed to run the workflow on the VPH Share platform (Koehler et al., 2012). The workflow is available for partners of the "VPH DARE@IT" project and accessible via the Taverna workflow

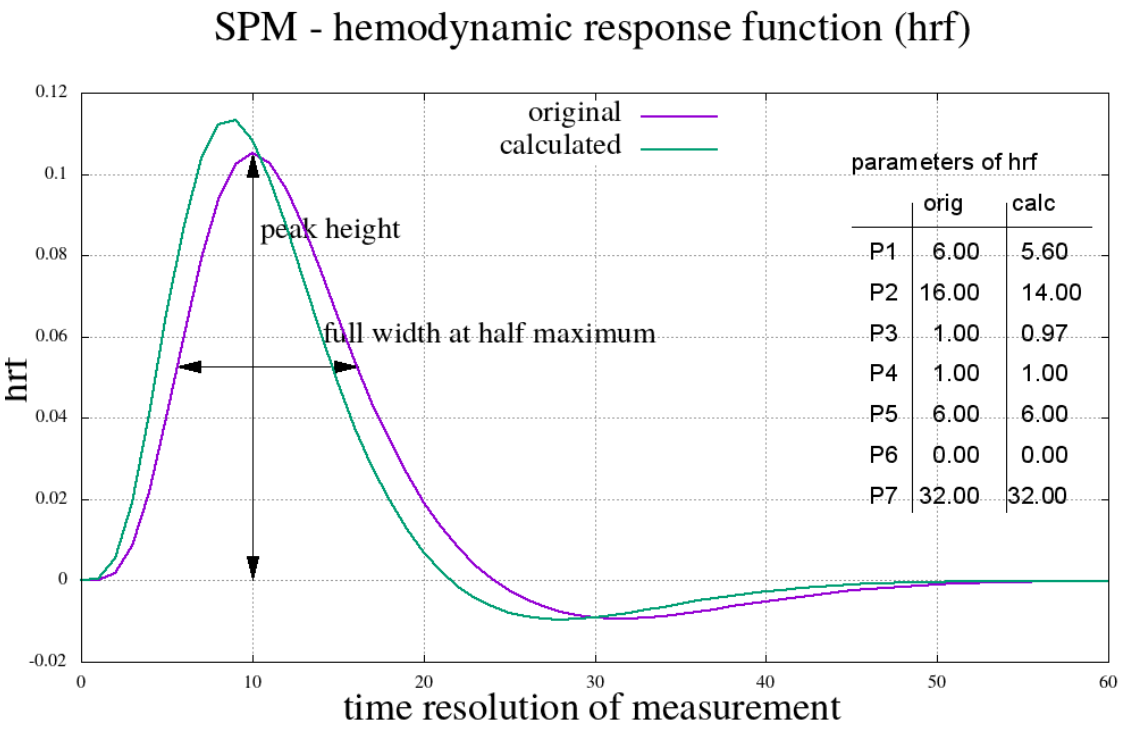

Figure 10.4.: Example output of the workflow. The figure shows a comparison of the calculated patient-specific parameters for the hemodynamic response function with the standard parameters used in SPM.

management system (Wolstencroft et al., 2013). Implementation of the workflow inside Taverna has been done by the team of Dr. Shusheel Varma (University of Sheffield).

10.6. Reproducibility and dissemination efforts

To guarantee that the model can be used outside the "VPH DARE@IT" consortium, the model has been uploaded to BioModels database (Chelliah et al., 2015). For this purpose, the model was exported as SBML V2L4 and all species and reactions have been annotated according to the MIRIAM guidelines (Novère et al., 2005). The model is available in the curated branch of the database as BIOMD0000000627[5]. A graphical representation of the full model using the Systems Biology Graphical Notation (SBGN) is also available from this database[6].

In addition to the SBML file, I have also a published a simulation experiment description in the SED-ML format. Running the encoded simulation reproduces the data necessary to create Figure 3 of the article in the Journal of Cerebral Blood Flow and Metabolism

[5]http://www.ebi.ac.uk/biomodels-main/BIOMD0000000627
[6]http://www.ebi.ac.uk/biomodels-main/download?mid=BIOMD0000000627&format=PNG

(Winter et al., 2017). The full list of equations and all parameter values are available as part of the supplementary material for this publication[7].

[7] http://journals.sagepub.com/doi/suppl/10.1177/0271678X17693024

11. Model analysis and results

Model construction, as described in the previous Chapter, was guided by the aim to answer the research questions defined in Section 7.4:

1. Is the shape of the BOLD signal sensitive to changes in the underlying metabolic network?

2. How far do known alterations in brain energy metabolism in AD affect the BOLD shape

To answer these questions, I undertook a two-step analysis of the kinetic model. In a first step, I used sensitivity analysis to quantify the effect of changes in the model parameters to the three main shape parameters of the BOLD response: time-of-peak, peak height and full width at half maximum. In a second step, I have created scenarios that model different situations observed in AD and analyse the impact of several simultaneous changes to the model parameters on the BOLD shape.

11.1. Sensitivity of the BOLD shape to changes in brain energy metabolism

Sensitivity analysis of the three shape parameters of the BOLD-response was performed using COPASI V4.18 for $t = 0$ to $t = 215s$ using 2150000 time steps (i.e. $\Delta t = 0.0001$). The chosen time frame guarantees that peak time, peak height and full width at half maximum can be calculated from the sample. For the calculation of peak time and FWHM, the default numerical precision of the ODE solver (relTol = 1e-06, absTol = 1e-12) was used, whereas for the calculation of peak time a precision of the chosen Δt was achieved. Scaled sensitivities were subsequently calculated with Matlab according to the following formula:

$$S(x) = \frac{\partial f(x)}{\partial x} \approx \frac{(f(x + \Delta x) - f(x))}{\Delta x} \cdot \frac{x}{f(x)} \tag{11.1}$$

where x is the cause (e.g. enzyme concentration) and f(x) is the effect (e.g. peak height). For Δx the default setting of COPASI V4.18 was used ($\Delta x = 0.001 \cdot x$). This formula pro-

vides a simple method for computing the finite difference approximation of the derivative and has been proven to yield robust results (Zi, 2011). Sensitivity analysis was performed in Matlab R2011b. This was necessary as there is no way to calculate the full width at half maximum in COPASI, as this would require postprocessing of the time-course data. The same is true for peak height and peak time. While they can in principle be tracked in COPASI using narrowly defined events, this approach is computationally very expensive and was therefore not used.

Sensitivity of the three shape parameters to changes in the metabolic reactions

Sensitivity analysis of the three main characteristics of the BOLD response was conducted for the model parameters which describe enzyme concentrations. The results, depicted in Figures 11.1 and 11.2, indicate that all three characteristics: peak height, full width at half maximum and peak timing are sensitive to changes in the reaction rate of reactions both from the glycolytic and the PPP branch. In the glycolytic branch (Figure 11.1), the three characteristics are most sensitive to changes in the reactions HK, PGI forward, PGI backward and PFK. The latter three are the glycolytic reactions with direct connections to the pentose phosphate pathway. Positive sensitivities in the neuronal reactions HK, PGI forward and PFK for peak height and FWHM correspond to negligible sensitivities of peak time in these reactions. In astrocytes, the positive sensitivity of the peak height in HK and PGI forward coincides with a negative sensitivity in full width at half maximum for these reactions. While for most reactions the effect of changes in neurons is more pronounced than in astrocytes, the opposite is true for LDH. Full width at half maximum is the parameter with the most pronounced sensitivity to changes in the glycolytic reactions overall.

In the pentose phosphate pathway, the sensitivities of peak height are quite small, but with the exception of TAL in astrocytes consistenly positive. With the exception of RKI in astrocytes and TKL-2 and TAL in neurons, positive sensitivities for peak height correspond to negative sensitivities in FWHM. For peak time, all non-negative sensitivities are identical, indicating that the difference is identical to the chosen Δt with which the peak timing was calculated.

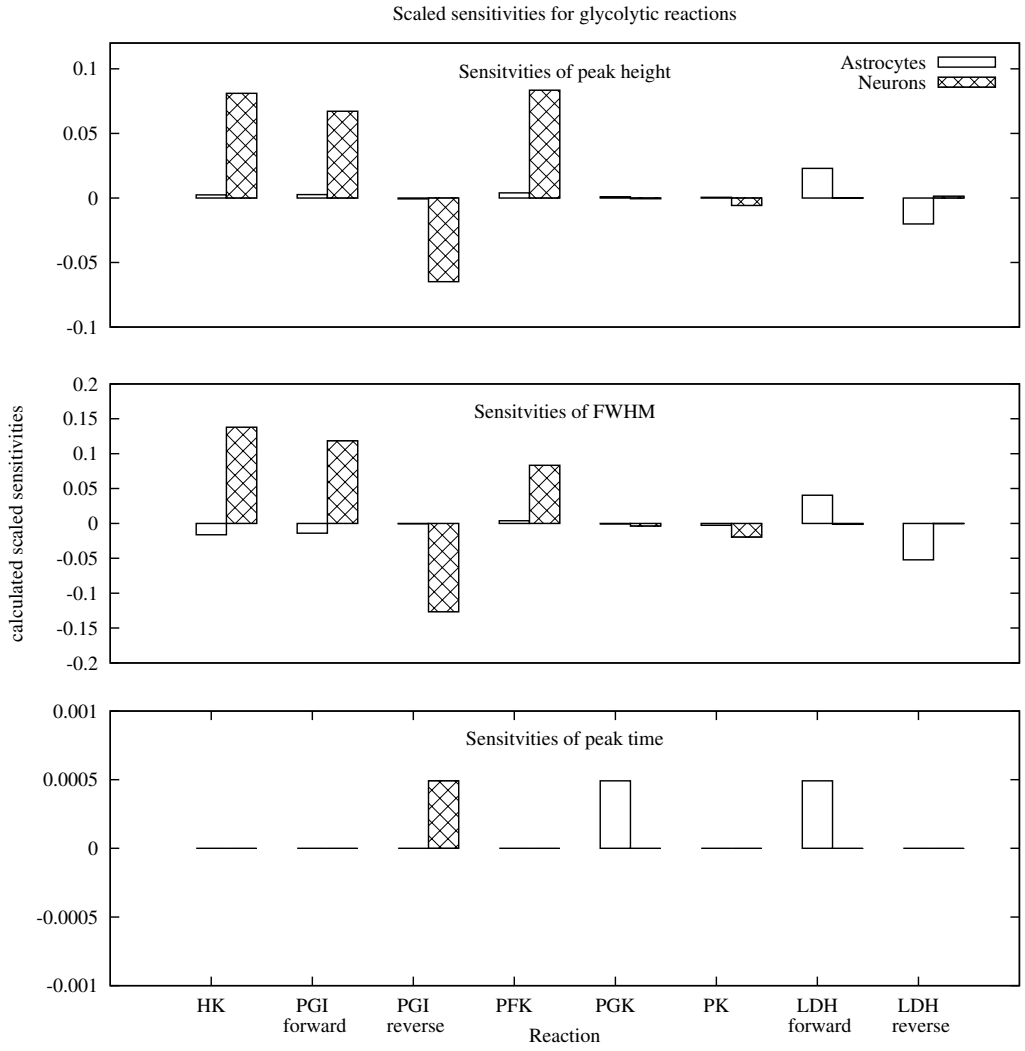

Figure 11.1.: Sensitivities of the shape parameters of the BOLD response with respect to glycolytic reactions.

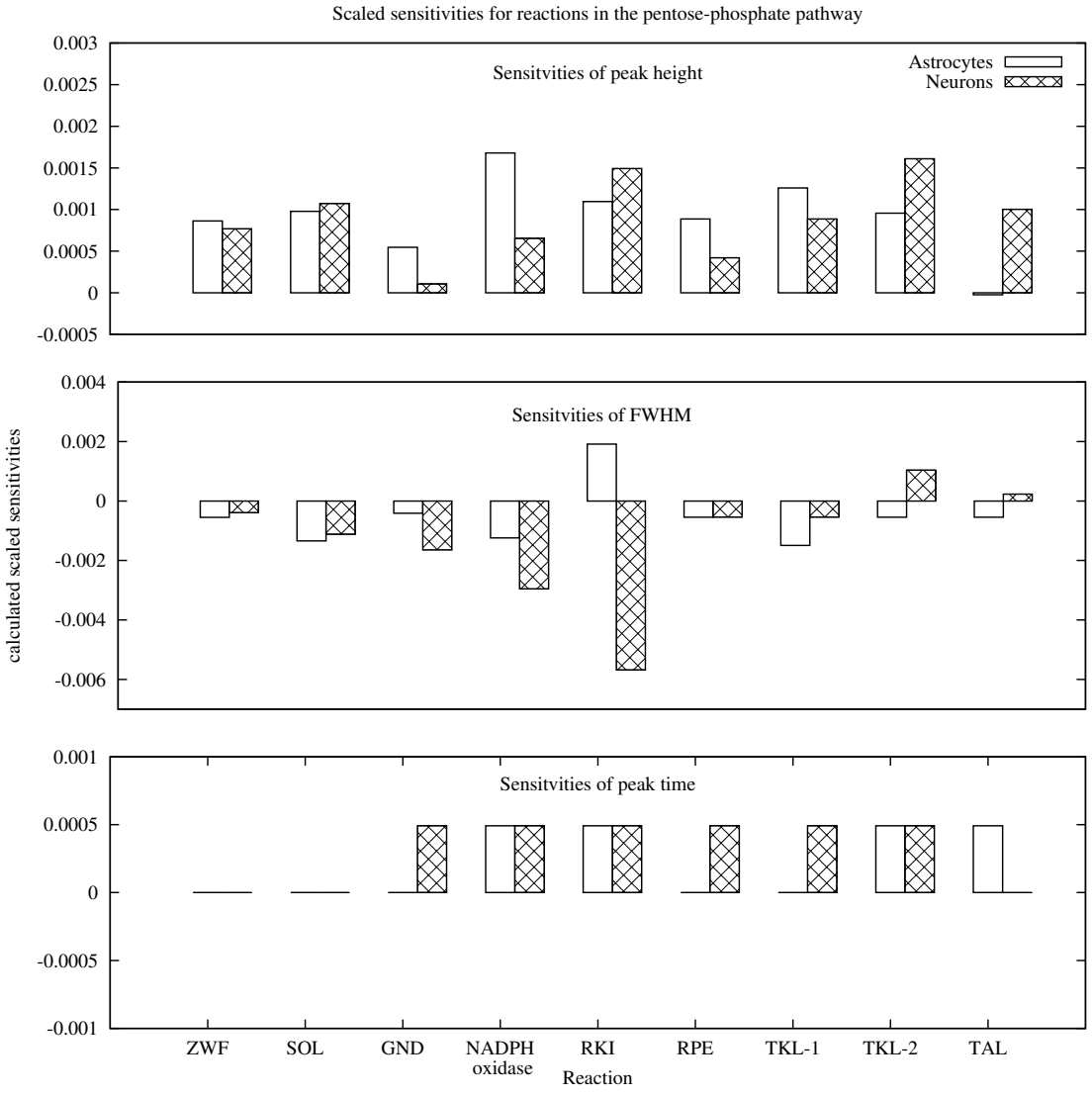

Figure 11.2.: Sensitivities of the shape parameters of the BOLD response with respect to the reactions of the pentose phosphate pathway.

11.2. Analysing the influence of metabolic alterations on the BOLD shape

To measure the influence of experimentally observed changes in AD patients as described in Section 8.6, I set the values for the enzyme concentration as reported in the specific publication. The following scenarios are considered:

Scenario definition

1. Healthy state: This is the model with all parameters unchanged
2. PPP activation: According to the experimental findings, the enzyme level for G6PDH was increased to 162 per cent and the enzyme level of GND to 126 per cent. The rate constant of the NADPH oxidase was also increased by 162 per cent to model the hypothesized increased demand for NADPH in the antioxidant defence system.
3. Glycolysis activation: The enzyme activity of lactate dehydrogenase (LDH), pyruvate kinase (PK) and phosphofructokinase (PFK) was increased to 120 per cent of its original value in neurons and astrocytes.
4. Increased astrocytic volume: To model the increase in the share of brain volume occupied by astrocytes, independently of the underlying mechanism, the relative amount of astrocytes in the model was increased from 0.25 to 0.3, while the relative amount of the extracellular space was reduced from 0.2 to 0.15 of the total volume, so that the total volume remains unchanged.

Each scenario was simulated and the resulting shift in the flux distribution and the value of the three characteristic shape parameters of the BOLD response were calculated.

Modelling results

Increased activity of G6PDH and GND – PPP activation scenario. Altering the enzyme concentration for the reactions G6PDH and GND according to the observations in Palmer (1999) led only to a slightly decreased BOLD peak height and full width at half maximum: less than 0.05 per cent in peak height and FWHM. This result was expected, as according to prior sensitivity analysis the sensitivities of the shape parameter to changes in the PPP are minute.

Increased activity of PFK, LDH and PK –Glycolysis activation scenario. Increasing the

concentration of phosphofructokinase, lactate dehydrogenase and pyruvate kinase by 20 per cent lead to an decrease in peak height by 0.84 per cent, an decrease in peak time by 0.07 per cent and an decrease in FWHM by 5.9 per cent. The alteration in the shape of the BOLD response in this scenario is more pronounced than the alteration in the PPP activation scenario, but the impact is still small, especially for peak height and peak time.

Astrocytic hypertrophy or hyperplasia – Increased astrocytic volume scenario. Increasing the astrocytic volume led to a decrease in the peak height by 2.38 per cent, a reduction in peak time by 0.1 per cent and a decrease in FWHM by 14 per cent (Figure 11.3).

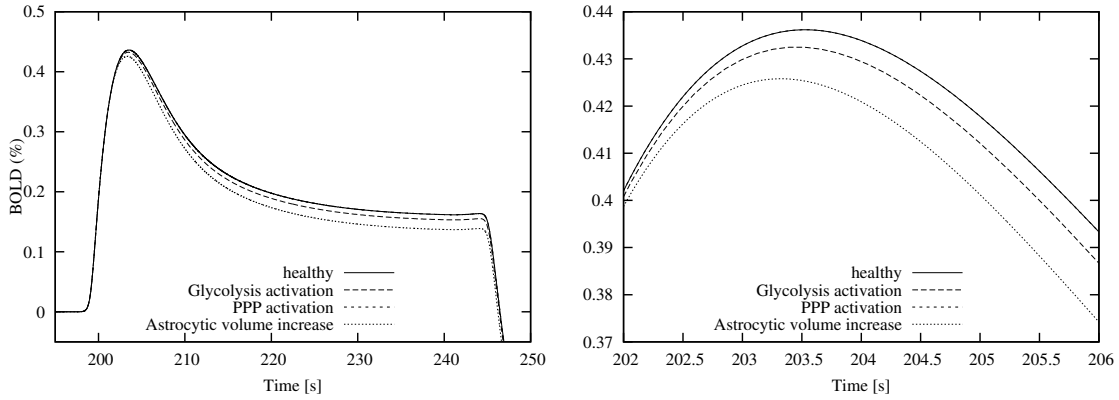

Figure 11.3.: Comparison of the BOLD shape resulting from the simulation of the four different scenarios.

11.3. Discussion

Summarizing the different results described above, I derive the following main conclusions:

1. *The new mathematical model allows an investigation of the effect of metabolic alterations reported in AD brains on the BOLD shape.* Blood oxygen level-dependent functional magnetic resonance imaging relies on a suitable model of the underlying hemodynamic response. Using a mathematical model of brain energy metabolism, neuronal stimulation and venous volume change, I am able to demonstrate how various reported changes in brain metabolism influence the three important parameters of the BOLD shape. In my model, the BOLD response is not calculated as the convolution of a hemodynamic response function with a fixed stimulus pattern, but instead directly calculated from a mathematical description of the underlying metabolic network and the hemodynamic response to a simulated stimulation. This allows relating the observed changes in the BOLD shape parameters to changes in the dynamics of the metabolic reaction network. An advantage of this approach is

that my model allows a simultaneous assessment of the influences on the shape of the BOLD response, such as changes in the flux distribution between the main glycolytic branch and the PPP, changes in expression of glycolytic enzymes and changes resulting from astrocytosis.

2. *The shape of the BOLD response is sensitive to changes in the metabolic network.* The sensitivity analysis revealed that the three characteristic properties of the BOLD signal, peak height, peak timing and full width at half maximum are sensitive to changes in the reaction rate of several reactions. While the calculated sensitivities are small, they are not negligible because they appear consistently. The classic view that changes in the BOLD shape are only attributed to changes in strength and duration of the stimulus does not hold. It is instead the FWHM which is most sensitive to these changes.

3. *Reported changes in enzyme activity have only small influence on the BOLD shape.* The analysis of the literature-derived scenarios revealed that the reported changes in enzyme activity have only a small influence on the simulated BOLD shape. The PPP activation scenario, which analysed the impact of an increase activity of the pentose phosphate pathway, resulted in a BOLD shape that can for practical purposes be considered identical to the healthy state. The glycolysis activation scenario, which assumes increased levels of phosphofructokinase, pyruvate kinase and lactate dehydrogenase, decreased the BOLD shape by less than one per cent and reduced the FWHM by about two per cent. While these changes seem negligible, one important aspect of these findings is that all changes in enzyme expression, which have been reported in the literature and are analysed here, resulted in lower values for peak height, peak time and FWHM. This is in line with the observation of a decrease in the BOLD response, reported for example in the cortex of a rat model of Alzheimer's disease (Sanganahalli et al., 2013). More importantly, is has been suggested that the increased enzyme levels observed in the glycolytic and the pentose phosphate pathway can be taken as a proxy for changes in the ratio of neurons and glia cells (Bigl et al., 1999). If this is the case, their impact on the BOLD shape may be much higher than this initial analysis suggests, as discussed below.

4. *Astrocytosis influences the BOLD shape.* The scenario with the most pronounced influence on the BOLD shape models the impact of astrocytic hypertrophy or hyperplasia, an important feature of AD neuropathology. The analysis presented above shows that such changes in the voxel composition exercise much more control on the resulting BOLD shape than changes in enzyme concentration alone. This result indicates that the close interaction between neurons and astrocytes in the regulation of brain energy metabolism might be a decisive factor for the shape of the BOLD

response. Given that the observed changes were reported for the hippocampus and the inferior temporal cortex, two regions affected early and extensively in AD, this might be the most relevant result of this study.

The results presented above have been obtained by *in silico* experiments, which allow to fix most of the observables and thereby focus on the contribution of individual changing parameters. The new model serves the particular purpose to quantify the contribution of individual metabolic reactions in an otherwise unchanged environment. The analysis therefore complements the clinical analysis of the BOLD response, in which many other aspects, such as stimulation-induced changes in ionic currents and vascular properties might be affected as well. Mathematical modelling, on the other hand, is a suitable tool to delineate the individual contributions and thereby increase the understanding of complex dynamic phenomena. While my model represents an important step towards a comprehensive model of brain energy metabolism and the vascular response, two important aspects, which have been also absent in previous models, are not included.

The neurovascular coupling in my model is currently realized via time-dependent changes in both metabolism and blood flow. While this is current practice, I expect that models that can include this connection might be able to shed more light on the connections between metabolic activity and the BOLD response. The second aspect, which has the potential to increase the accuracy of the results, is the mechanistic coupling of mitochondrial activity and the production of reactive oxygen species (ROS) with the demand of NADPH. While there exist several publications modelling the production of ROS in the mitochondria, the current state of the art does not allow an inclusion of these models into the model presented here. This is due to the complex nature of the electron transport chain, the main source of ROS, and the lack of time-series data of this process. The available models restrict their analysis to the steady state behaviour (Berndt et al., 2012; Guillaud et al., 2014) or use a rule-driven modelling approach to circumvent the difficulties associated with the complexity of kinetic models (Selivanov et al., 2011). I restricted the model therefore to mimicking the increase in NADPH demand by variations in the NADPH oxidase reaction.

Finally, a feature of the model that might need further attention in future studies is the glutamate-glutamine cycle. In the model presented here, I used the approach chosen by Cloutier et al. (2009), i.e. a simplified description of glutamate shuttling coupled to sodium exchange. Using this approach, it is possible to couple energy requirements in neurons and astrocytes and thereby analyse the close interaction of the different cell types. However, there is increasing evidence that the parameters chosen by Cloutier et al. (2009) need to be reconsidered. In particular, DiNuzzo et al. (2016) very recently reported a higher ratio of Na+/glutamate and argued that potassium instead of glutamate might be the decisive

factor of metabolic coupling of neurons and astrocytes.

To use this model in the clinical analysis of BOLD fMRI data, the differences in peak height, peak timing and FWHM need to be expressed in terms of parameter adjustments of the HRF supplied by the image analysis software. One way to do this is the integration into the research pipeline as described in Section 10.5.

Comprehensive mathematical models of brain energy metabolism such as the one presented here can play an important role in the creation of personalised and disease-specific HRFs. The current state of the art allows accounting for the individual variability of the concentration of blood metabolites such as glucose and oxygen. Future models, however, may also offer the possibility to include information about differences in vascular determinants of the HRF such as arterial compliance. While these results need clinical validation, they offer a potential path towards future disease-specific hemodynamic response functions.

Part III.

Conclusions

In this work, I described my contribution to two different projects that applied mathematical modelling to understand different aspects of Alzheimer's disease.

The first project deals with aggregation dynamics of β-amyloid, the main protagonist of the *amyloid hypothesis*. The extracellular plaques formed by the accumulation of this protein are today still the only feature that allows the diagnosis of pathophysiologically proved AD dementia, and are by some assumed to be the cause of AD, rather than a consequence. Aggregation of β-amyloid can be seen as a consequence of an imbalance between production an removal, and both processes have received considerable attention in the past.

The work presented here focuses on the role of Aβ removal and was guided by two main goals: Understanding the mechanisms necessary to model protein aggregation *in vivo* and quantifying the impact of ABC-transporter knockouts in two different mouse models. Given the multitude of mechanisms involved in the *in vivo* aggregation of Aβ, some of which certainly still unknown, I did not attempt a detailed mechanistic mathematical representation. Instead, I have developed a phenomenological model that describes Aβ production, Aβ aggregation via several intermediates as well as Aβ removal from the brain. The model distinguishes between nucleation, aggregation of soluble intermediates and aggregation of insoluble intermediates. The models parameters values have been calibrated using a subset of the available experimental data measured in $ABCC1^{-/-}$ mice.

Regarding the mechanisms necessary to model *in vivo* protein aggregation and removal, there are two important findings. First, Aβ aggregation can be assumed to occur by monomer addition to the nuclei. Second, removal of monomeric Aβ by ABC transporters is hampered by larger Aβ aggregates. Using these two main assumptions my model is able to capture the dynamics of the given dataset of protein aggregation in mice and the model simulations show excellent agreement with the experimental data. Using a second dataset that was not used to calibrate the models parameters for nucleation and aggregation, I was able to show that the difference in the aggregation dynamics observed between $ABCC1^{-/-}$ and $ABCB1^{-/-}$ mice can be explained by a difference in the transport capacity alone. A comparison of the predicted aggregation time course for both mouse models and the calculated effective Aβ inflow highlights the enormous effect a small difference in the onset of increased inflow of Aβ has on the aggregation profile

Improved understanding of the influence of larger aggregates on beta-amyloid on the removal of monomers might be a key step towards the development of interventions that keep its production and degradation in balance.

Understanding the importance of the metabolic influence on the BOLD shape is of special interest for Alzheimer's disease, where several metabolic alterations have been described to occur during disease progression. The purely phenomenological description of the hemodynamic response function, which is currently used in clinical practice, does, however, not relate the BOLD shape to the underlying biological processes. Using this function, it is therefore not possible to incorporate information about blood composition, vascular compliance or metabolic reaction dynamics in the clinical analysis of BOLD fMRI data. Instead, a mechanistic description of the hemodynamic response is required.

The work at hand describes the development and analysis of a mechanistic mathematical model for brain energy metabolism and the hemodynamic response. One important requirement of the model is that it should allow the analysis of several AD-related changes in glycolysis, the pentose-phosphate pathway and cerebral tissue composition. My model contains for the first time a description of the pentose phosphate pathway which has not been considered in earlier models. Its inclusion is one of the major contributions of the work presented here.

Critical aspects in the inclusion of pentose-phosphate pathway were the calculation of physiologically and thermodynamically meaningful parameter values, for which I collected data from several heterogeneous sources. The resulting parameterization successfully reflects experimental findings for the flux distribution in adult brain tissue. The resulting shape of the BOLD response compares well to the shape reported in other modelling studies. Sensitivity analysis of the three main characteristics of the BOLD response reveals that all three characteristics: peak height, full width at half maximum and peak timing are sensitive to changes in the reaction rate of reactions both from the glycolytic and the PPP branch.

The model therefore allows an investigation of the effect of metabolic alterations reported in AD brains on the BOLD shape. The results of this analysis show that the shape of the BOLD response is sensitive to changes in the metabolic network. In particular, I have analysed the influence of experimentally observed changes in enzyme expression using several literature derived scenarios. he reported changes in enzyme activity have only small influence on the BOLD shape. Nevertheless, the analysis of astrocytosis demonstrates a significant impact on the three characteristic properties of the BOLD shape. Inside the "VPH DARE@IT" project the model is used as part of a workflow that uses patient-specific data to calculate personalized parameters for the canonical hemodynamic response function.

The two models described in this thesis integrate and extend several other models and summarise more than six years of work. Besides the biomedical conclusions derived from the effort of model construction and analysis, the models themselves are a contribution to the current state of the art. It was therefore an important objective to make both models reproducible and publicly available. To guarantee that the model can be used outside of the respective project consortia they have been uploaded to BioModels database. For this purpose, the models were encoded in the Systems Biology Markup Language (SBML) V2L4 and annotated according to the MIRIAM guidelines. The models are available in the curated branch of the database as BIOMD0000000618 (Aβ aggregation model) and BIOMD0000000627 (brain energy metabolism model). A graphical representation of the latter model using the Systems Biology Graphical Notation is also available from this database.

12. Bibliography

Alzheimer, A. (1907). Über eine eigenartige Erkrankung der Hirnrinde. *Allgemeine Zeitschrift für Psychatrie und psychisch-Gerichtliche Medizin*, 46(146-148).

Alzheimer's Association (2014). 2014 Alzheimer's Disease Facts and Figures. *Alzheimer's & Dementia*, 10(2):e47–e92.

Aubert, A. and Costalat, R. (2002). A Model of the Coupling between Brain Electrical Activity, Metabolism, and Hemodynamics: Application to the Interpretation of Functional Neuroimaging. *NeuroImage*, 17(3):1162–1181.

Aubert, A. and Costalat, R. (2005). Interaction between astrocytes and neurons studied using a mathematical model of compartmentalized energy metabolism. *Journal of Cerebral Blood Flow & Metabolism*, 25(11):1476–1490.

Aubert, A., Costalat, R., and Valabrègue, R. (2001). Modelling of the Coupling between Brain Electrical Activity and Metabolism. *Acta Biotheoretica*, 49(4):p 301–326.

Aubert, A., Pellerin, L., Magistretti, P. J., and Costalat, R. (2007). A coherent neurobiological framework for functional neuroimaging provided by a model integrating compartmentalized energy metabolism. *Proceedings of the National Academy of Sciences*, 104(10):4188–4193.

Auer, S., Meersman, F., Dobson, C. M., and Vendruscolo, M. (2008). A Generic Mechanism of Emergence of Amyloid Protofilaments from Disordered Oligomeric Aggregates. *PLOS Comput Biol*, 4(11):e1000222.

Bakos, E. and Homolya, L. (2007). Portrait of multifaceted transporter, the multidrug resistance-associated protein 1 (MRP1/ABCC1). *Pflügers Archiv - European Journal of Physiology*, 453(5):621–641.

Bélanger, M., Allaman, I., and Magistretti, P. (2011). Brain Energy Metabolism: Focus on Astrocyte-Neuron Metabolic Cooperation. *Cell Metabolism*, 14(6):724–738.

Berg, J. M., Tymoczko, J. L., Stryer, L., Berg, J. M., Tymoczko, J. L., and Stryer, L. (2002). *Biochemistry*. W H Freeman, 5th edition.

Berndt, N., Bulik, S., and Holzhütter, H.-G. (2012). Kinetic Modeling of the Mitochondrial Energy Metabolism of Neuronal Cells: The Impact of Reduced α-Ketoglutarate Dehydrogenase Activities on ATP Production and Generation of Reactive Oxygen Species. *International Journal of Cell Biology*, 2012.

Bernstein, S. L., Dupuis, N. F., Lazo, N. D., Wyttenbach, T., Condron, M. M., Bitan, G., Teplow, D. B., Shea, J.-E., Ruotolo, B. T., Robinson, C. V., and Bowers, M. T. (2009). Amyloid-β protein oligomerization and the importance of tetramers and dodecamers in the aetiology of Alzheimer's disease. *Nature Chemistry*, 1(4):326–331.

Bertram, L., Lill, C. M., and Tanzi, R. E. (2010). The Genetics of Alzheimer Disease: Back to the Future. *Neuron*, 68(2):270–281.

Bickel, H. (2016). Die Häufigkeit von Demenzerkrankungen. *Deutsche Alzheimer Gesellschaft*, Informationsblatt 1.

Bigl, M., Bleyl, A.-D., Zedlick, D., Arendt, T., Bigl, V., and Eschrich, K. (1996). Changes of activity and isozyme pattern of phosphofructokinase in the brains of patients with Alzheimer's disease. *Journal of Neurochemistry*, 67(3):1164–1171.

Bigl, M., Brückner, M., Arendt, T., Bigl, V., and Eschrich, K. (1999). Activities of key glycolytic enzymes in the brains of patients with Alzheimer's disease. *Journal of Neural Transmission*, (106):499–511.

Braak, H. and Braak, E. (1991). Neuropathological stageing of Alzheimer-related changes. *Acta Neuropathologica*, 82(4):239–259.

Broersen, K., Rousseau, F., and Schymkowitz, J. (2010). The culprit behind amyloid beta peptide related neurotoxicity in Alzheimer's disease: oligomer size or conformation? *Alzheimer's Research & Therapy*, 2(4):12.

Brown, A. M. and Ransom, B. R. (2007). Astrocyte Glycogen and Brain Energy Metabolism. *Glia*, 55(12):1263–1271.

Bürklen, T. S., Schlattner, U., Homayouni, R., Gough, K., Rak, M., Szeghalmi, A., and Wallimann, T. (2006). The Creatine Kinase/Creatine Connection to Alzheimer's Disease: CK Inactivation, APP-CK Complexes and Focal Creatine Deposits. *BioMed Research International*, 2006:e35936.

Bussieck, M. R. and Pruessner, A. (2003). Mixed-Integer Nonlinear Programming. *SIAG/OPT Newsletter: Views & News*, 14(1):19–22.

Buxton, R. B. and Frank, L. R. (1997). A Model for the Coupling between Cerebral Blood Flow and Oxygen Metabolism during Neural Stimulation. *Journal of Cerebral Blood Flow & Metabolism*, 17(1):64–72.

Buxton, R. B., Miller, K. L., Frank, L. R., and Wong, E. C. (1998a). BOLD Signal Dynamics: The Balloon Model with Viscoelastic Effects. *Proc. Int. Mag Reson. Med.*, (6):1401.

Buxton, R. B., Wong, E. C., and Frank, L. R. (1998b). Dynamics of blood flow and oxygenation changes during brain activation: The balloon model. *Magnetic Resonance in Medicine*, 39(6):855–864.

Chelliah, V., Juty, N., Ajmera, I., Ali, R., Dumousseau, M., Glont, M., Hucka, M., Jalowicki, G., Keating, S., Knight-Schrijver, V., Lloret-Villas, A., Natarajan, K. N., Pettit, J.-B., Rodriguez, N., Schubert, M., Wimalaratne, S. M., Zhao, Y., Hermjakob, H., Le Novère, N., and Laibe, C. (2015). BioModels: ten-year anniversary. *Nucleic Acids Research*, 43(D1):D542–D548.

Claeysen, S., Cochet, M., Donneger, R., Dumuis, A., Bockaert, J., and Giannoni, P. (2012). Alzheimer culprits: Cellular crossroads and interplay. *Cellular Signalling*, 24(9):1831–1840.

Cloutier, M., Bolger, F. B., Lowry, J. P., and Wellstead, P. (2009). An integrative dynamic model of brain energy metabolism using in vivo neurochemical measurements. *Journal of Computational Neuroscience*, 27(3):391–414.

Craft, D. L., Wein, L. M., and Selkoe, D. J. (2002). A Mathematical Model of the Impact of Novel Treatments on the Aβ Burden in the Alzheimer's Brain, CSF and Plasma. *Bulletin of Mathematical Biology*, 64(5):1011–1031.

Cummings, J. L., Morstorf, T., and Zhong, K. (2014). Alzheimer's disease drug-development pipeline: few candidates, frequent failures. *Alzheimer's Research & Therapy*, 6:37.

Dean, M., Rzhetsky, A., and Allikmets, R. (2001). The Human ATP-Binding Cassette (ABC) Transporter Superfamily. *Genome Research*, 11(7):1156–1166.

Der-Sarkissian, A., Jao, C. C., Chen, J., and Langen, R. (2003). Structural organization of α-synuclein fibrils studied by site-directed spin labeling. *Journal of Biological Chemistry*, 278(39):37530–37535.

DiNuzzo, M., Giove, F., Maraviglia, B., and Mangia, S. (2016). Computational Flux Balance Analysis Predicts that Stimulation of Energy Metabolism in Astrocytes and their Metabolic Interactions with Neurons Depend on Uptake of K+ Rather than Glutamate. *Neurochemical Research*, pages 1–15.

ElAli, A. and Rivest, S. (2013). The role of ABCB1 and ABCA1 in beta-amyloid clearance at the neurovascular unit in Alzheimer's disease. *Frontiers in Physiology*, 4.

Finder, V. H. and Glockshuber, R. (2007). Amyloid-β Aggregation. *Neurodegenerative Diseases*, 4(1):13–27.

Flamholz, A., Noor, E., Bar-Even, A., and Milo, R. (2012). eQuilibrator—the biochemical thermodynamics calculator. *Nucleic Acids Research*, 40(D1):D770–D775.

Friston, K. J., editor (2007). *Statistical parametric mapping: the analysis of funtional brain images*. Elsevier/Academic Press, Amsterdam ; Boston, 1st ed edition.

Friston, K. J., Mechelli, A., Turner, R., and Price, C. J. (2000). Nonlinear Responses in fMRI: The Balloon Model, Volterra Kernels, and Other Hemodynamics. *NeuroImage*, 12(4):466–477.

Glover, G. H. (1999). Deconvolution of Impulse Response in Event-Related BOLD fMRI1. *NeuroImage*, 9(4):416–429.

Grubelnik, V., Zahle Larsen, A., Kummer, U., Folke Olsen, L., and Marhl, M. (2001). Mitochondria regulate the amplitude of simple and complex calcium oscillations. *Biophysical Chemistry*, 94(12):59–74.

Guillaud, F., Dröse, S., Kowald, A., Brandt, U., and Klipp, E. (2014). Superoxide production by cytochrome bc1 complex: A mathematical model. *Biochimica et Biophysica Acta (BBA) - Bioenergetics*, 1837(10):1643–1652.

Haass, C. and Selkoe, D. J. (2007). Soluble protein oligomers in neurodegeneration: lessons from the Alzheimer's amyloid β-peptide. *Nature Reviews Molecular Cell Biology*, 8(2):101–112.

Heinrich, R. and Schuster, S. (1996). *The Regulation of Cellular Systems*. Springer US, Boston, MA.

Herzig, M. C., Winkler, D. T., Burgermeister, P., Pfeifer, M., Kohler, E., Schmidt, S. D., Danner, S., Abramowski, D., Stürchler-Pierrat, C., Bürki, K., van Duinen, S. G., Maat-Schieman, M. L. C., Staufenbiel, M., Mathews, P. M., and Jucker, M. (2004). Aβ is targeted to the vasculature in a mouse model of hereditary cerebral hemorrhage with amyloidosis. *Nature Neuroscience*, 7(9):954–960.

Higgins, C. F. (2001). ABC transporters: physiology, structure and mechanism an overview. *Research in Microbiology*, 152(34):205–210.

Holzhütter, H.-G. (2004). The principle of flux minimization and its application to estimate stationary fluxes in metabolic networks. *European Journal of Biochemistry*, 271(14):2905–2922.

Hoops, S., Sahle, S., Gauges, R., Lee, C., Pahle, J., Simus, N., Singhal, M., Xu, L., Mendes, P., and Kummer, U. (2006). COPASI—a COmplex PAthway SImulator. *Bioinformatics*, 22(24):3067–3074.

Hucka, M., Finney, A., Sauro, H. M., Bolouri, H., Doyle, J. C., Kitano, H., Arkin, A. P., Bornstein, B. J., Bray, D., Cornish-Bowden, A., Cuellar, A. A., Dronov, S., Gilles, E. D., Ginkel, M., Gor, V., Goryanin, I. I., Hedley, W. J., Hodgman, T. C., Hofmeyr, J.-H., Hunter, P. J., Juty, N. S., Kasberger, J. L., Kremling, A., Kummer, U., Le Novère, N., Loew, L. M., Lucio, D., Mendes, P., Minch, E., Mjolsness, E. D., Nakayama, Y., Nelson, M. R., Nielsen, P. F., Sakurada, T., Schaff, J. C., Shapiro, B. E., Shimizu, T. S., Spence, H. D., Stelling, J., Takahashi, K., Tomita, M., Wagner, J., and Wang, J. (2003). The systems biology markup language (SBML): a medium for representation and exchange of biochemical network models. *Bioinformatics*, 19(4):524–531.

Jack Jr, C. R., Knopman, D. S., Jagust, W. J., Petersen, R. C., Weiner, M. W., Aisen, P. S., Shaw, L. M., Vemuri, P., Wiste, H. J., Weigand, S. D., Lesnick, T. G., Pankratz, V. S., Donohue, M. C., and Trojanowski, J. Q. (2013). Tracking pathophysiological processes in Alzheimer's disease: an updated hypothetical model of dynamic biomarkers. *The Lancet Neurology*, 12(2):207–216.

Joshi, A. and Palsson, B. O. (1989). Metabolic dynamics in the human red cell: Part IA comprehensive kinetic model. *Journal of Theoretical Biology*, 141(4):515–528.

Kholodenko, B. N., Cascante, M., Hoek, J. B., Westerhoff, H. V., and Schwaber, J. (1998). Metabolic design: How to engineer a living cell to desired metabolite concentrations and fluxes. *Biotechnology and Bioengineering*, 59(2):239–247.

Kivistö, J., Soininen, H., and Pihlajamaki, M. (2014). Functional MRI in Alzheimer's Disease. In Papageorgiou, T. D., Christopoulos, G. I., and Smirnakis, S. M., editors, *Advanced Brain Neuroimaging Topics in Health and Disease - Methods and Applications*. InTech.

Koehler, M., Knight, R., Benkner, S., Kaniovskyi, Y., and Wood, S. (2012). The VPH-Share Data Management Platform: Enabling Collaborative Data Management for the Virtual Physiological Human Community. In *2012 Eighth International Conference on Semantics, Knowledge and Grids*, pages 80–87.

Krohn, M., Lange, C., Hofrichter, J., Scheffler, K., Stenzel, J., Steffen, J., Schumacher, T., Brning, T., Plath, A.-S., Alfen, F., Schmidt, A., Winter, F., Rateitschak, K., Wree, A., Gsponer, J., Walker, L. C., and Pahnke, J. (2011). Cerebral amyloid-β proteostasis is regulated by the membrane transport protein ABCC1 in mice. *Journal of Clinical Investigation*, 121(10):3924–3931.

Kuhnke, D., Jedlitschky, G., Grube, M., Krohn, M., Jucker, M., Mosyagin, I., Cascorbi, I., Walker, L. C., Kroemer, H. K., Warzok, R. W., and Vogelgesang, S. (2007). MDR1-P-Glycoprotein (ABCB1) Mediates Transport of Alzheimers Amyloid- PeptidesImplications for the Mechanisms of A Clearance at the BloodBrain Barrier. *Brain Pathology*, 17(4):347–353.

LaFerla, F. M. and Green, K. N. (2012). Animal models of Alzheimer Disease. *Cold Spring Harbor Perspectives in Medicine*, 2(11):a006320.

Le Novère, N. (2015). Quantitative and logic modelling of molecular and gene networks. *Nature Reviews Genetics*, 16(3):146–158.

Lee, S., Fernandez, E. J., and Good, T. A. (2007). Role of aggregation conditions in structure, stability, and toxicity of intermediates in the A fibril formation pathway. *Protein Science*, 16(4):723–732.

Liebermeister, W., Uhlendorf, J., and Klipp, E. (2010). Modular rate laws for enzymatic reactions: thermodynamics, elasticities and implementation. *Bioinformatics*, 26(12):1528–1534.

Lilliefors, H. W. (1967). On the Komogorov-Smirnov test for normality with mean and variance unknown. *Americal Statistical Association Journal*.

Limpert, E., Stahel, W. A., and Abbt, M. (2001). Log-normal Distributions across the Sciences: Keys and Clues On the charms of statistics, and how mechanical models resembling gambling machines offer a link to a handy way to characterize log-normal distributions, which can provide deeper insight into variability and probabilitynormal or log-normal: That is the question. *BioScience*, 51(5):341–352.

Lindquist, M. A. (2008). The Statistical Analysis of fMRI Data. *Statistical Science*, 23(4):439–464.

Lindquist, M. A., Meng Loh, J., Atlas, L. Y., and Wager, T. D. (2009). Modeling the hemodynamic response function in fMRI: Efficiency, bias and mis-modeling. *NeuroImage*, 45(1):S187–S198.

Logothetis, N. K., Pauls, J., Augath, M., Trinath, T., and Oeltermann, A. (2001). Neurophysiological investigation of the basis of the fMRI signal. *Nature*, 412(6843):150–157.

Lomakin, A., Chung, D. S., Benedek, G. B., Kirschner, D. A., and Teplow, D. B. (1996). On the nucleation and growth of amyloid beta-protein fibrils: detection of nuclei and quantitation of rate constants. *Proceedings of the National Academy of Sciences*, 93(3):1125–1129.

Lubitz, T., Hahn, J., Bergmann, F. T., Noor, E., Klipp, E., and Liebermeister, W. (2016). SBtab: a flexible table format for data exchange in systems biology. *Bioinformatics*, 32(16):2559–2561.

Lubitz, T., Schulz, M., Klipp, E., and Liebermeister, W. (2010). Parameter Balancing in Kinetic Models of Cell Metabolism. *The Journal of Physical Chemistry B*, 114(49):16298–16303.

McKhann, G. M., Knopman, D. S., Chertkow, H., Hyman, B. T., Jack, C. R., Kawas, C. H., Klunk, W. E., Koroshetz, W. J., Manly, J. J., Mayeux, R., Mohs, R. C., Morris, J. C., Rossor, M. N., Scheltens, P., Carrillo, M. C., Thies, B., Weintraub, S., and Phelps, C. H. (2011). The diagnosis of dementia due to Alzheimer's disease: Recommendations from the National Institute on Aging-Alzheimer's association workgroups on diagnostic guidelines for Alzheimer's disease. *Alzheimer's & Dementia*, 7(3):263–269.

Messiha, H. L., Kent, E., Malys, N., Carroll, K. M., Swainston, N., Mendes, P., and Smallbone, K. (2014). Enzyme characterisation and kinetic modelling of the pentose phosphate pathway in yeast. Technical Report e146v4, PeerJ PrePrints.

Morris, A. M., Watzky, M. A., Agar, J. N., and Finke, R. G. (2008). Fitting Neurological Protein Aggregation Kinetic Data via a 2-Step, Minimal/Ockham's Razor Model: The FinkeWatzky Mechanism of Nucleation Followed by Autocatalytic Surface Growth . *Biochemistry*, 47(8):2413–2427.

Morris, A. M., Watzky, M. A., and Finke, R. G. (2009). Protein aggregation kinetics, mechanism, and curve-fitting: A review of the literature. *Biochimica et Biophysica Acta (BBA) - Proteins and Proteomics*, 1794(3):375–397.

Novère, N. L., Finney, A., Hucka, M., Bhalla, U. S., Campagne, F., Collado-Vides, J., Crampin, E. J., Halstead, M., Klipp, E., Mendes, P., Nielsen, P., Sauro, H., Shapiro, B., Snoep, J. L., Spence, H. D., and Wanner, B. L. (2005). Minimum information requested in the annotation of biochemical models (MIRIAM). *Nature Biotechnology*, 23(12):1509–1515.

Ogawa, S., Lee, T. M., Kay, A. R., and Tank, D. W. (1990). Brain magnetic resonance imaging with contrast dependent on blood oxygenation. *Proceedings of the National Academy of Sciences*, 87(24):9868–9872.

Oosawa, F., Asakura, S., Hotta, K., Imai, N., and Ooi, T. (1959). G-F transformation of actin as a fibrous condensation. *Journal of Polymer Science*, 37(132):323–336.

Orešič, M., Hyötyläinen, T., Herukka, S.-K., Sysi-Aho, M., Mattila, I., Seppnan-Laakso, T., Julkunen, V., Gopalacharyulu, P. V., Hallikainen, M., Koikkalainen, J., Kivipelto,

M., Helisalmi, S., Lötjönen, J., and Soininen, H. (2011). Metabolome in progression to Alzheimer's disease. *Translational Psychiatry*, 1(12):e57.

Pallitto, M. M. and Murphy, R. M. (2001). A Mathematical Model of the Kinetics of β-Amyloid Fibril Growth from the Denatured State. *Biophysical Journal*, 81(3):1805–1822.

Palmer, A. M. (1999). The activity of the pentose phosphate pathway is increased in response to oxidative stress in Alzheimer's disease. *Journal of Neural Transmission*, 106(3-4):317–328.

Pauling, L. and Coryell, C. D. (1936). The Magnetic Properties and Structure of Hemoglobin, Oxyhemoglobin and Carbonmonoxyhemoglobin. *Proceedings of the National Academy of Sciences of the United States of America*, 22(4):210–216.

Pflanzner, T., R. Kuhlmann, C., and U. Pietrzik, C. (2010). Blood-brain-barrier models for the investigation of transporter- and receptor-mediated amyloid-β clearance in Alzheimers disease. *Current Alzheimer Research*, 7(7):578–590.

Poirier, M. A., Jiang, H., and Ross, C. A. (2005). A structure-based analysis of huntingtin mutant polyglutamine aggregation and toxicity: evidence for a compact beta-sheet structure. *Human Molecular Genetics*, 14(6):765–774.

Prince, M. and Jackson, J. (2009). World Alzheimer Report.

Radde, R., Bolmont, T., Kaeser, S. A., Coomaraswamy, J., Lindau, D., Stoltze, L., Calhoun, M. E., Jäggi, F., Wolburg, H., Gengler, S., Haass, C., Ghetti, B., Czech, C., Hölscher, C., Mathews, P. M., and Jucker, M. (2006). Aβ42-driven cerebral amyloidosis in transgenic mice reveals early and robust pathology. *EMBO reports*, 7(9):940–946.

Raichle, M. E. and Mintun, M. A. (2006). Brain Work and Brain Imaging. *Annual Review of Neuroscience*, 29(1):449–476.

Riganti, C., Gazzano, E., Polimeni, M., Aldieri, E., and Ghigo, D. (2012). The pentose phosphate pathway: An antioxidant defense and a crossroad in tumor cell fate. *Free Radical Biology and Medicine*, 53(3):421–436.

Roberts, C. J. (2007). Non-native protein aggregation kinetics. *Biotechnology and Bioengineering*, 98(5):927–938.

Robinson, S. R. (2001). Changes in the cellular distribution of glutamine synthetase in Alzheimer's disease. *Journal of neuroscience research*, 66(5):972–980.

Rodríguez, J. J., Olabarria, M., Chvatal, A., and Verkhratsky, A. (2008). Astroglia in dementia and Alzheimer's disease. *Cell Death & Differentiation*, 16(3):378–385.

Rogeberg, M., Furlund, C. B., Moe, M. K., and Fladby, T. (2014). Identification of peptide products from enzymatic degradation of amyloid beta. *Biochimie*, 105:216–220.

Ross, C. A. and Poirier, M. A. (2004). Protein aggregation and neurodegenerative disease. *Published online: 01 July 2004; | doi:10.1038/nm1066*, 10:S10–S17.

Roychaudhuri, R., Yang, M., Hoshi, M. M., and Teplow, D. B. (2009). Amyloid β-Protein Assembly and Alzheimer Disease. *Journal of Biological Chemistry*, 284(8):4749–4753.

Russel, R. L., Siedlak, S. L., Raina, A. K., Bautista, J. M., Smith, M. A., and Perry, G. (1999). Increased Neuronal Glucose-6-phosphate Dehydrogenase and Sulfhydril Levls indicate reductive compensation to oxidative stress in Alzheimer Disease. *Archives of Biochemistry and Biophysics*, 370(2):236–239.

Saez, I., Duran, J., Sinadinos, C., Beltran, A., Yanes, O., Tevy, M. F., Martínez-Pons, C., Milán, M., and Guinovart, J. J. (2014). Neurons have an active glycogen metabolism that contributes to tolerance to hypoxia. *Journal of Cerebral Blood Flow & Metabolism*, 34(6):945–955.

Salminen, A., Haapasalo, A., Kauppinen, A., Kaarniranta, K., Soininen, H., and Hiltunen, M. (2015). Impaired mitochondrial energy metabolism in Alzheimer's disease: Impact on pathogenesis via disturbed epigenetic regulation of chromatin landscape. *Progress in Neurobiology*, 131:1–20.

Sanganahalli, B. G., Herman, P., Behar, K. L., Blumenfeld, H., Rothman, D. L., and Fahmeed Hyder (2013). Functional MRI and neural responses in a rat model of Alzheimer's disease. *NeuroImage*, 79:404–411.

Schlattner, U., Tokarska-Schlattner, M., and Wallimann, T. (2006). Mitochondrial creatine kinase in human health and disease. *Biochimica et Biophysica Acta (BBA) - Molecular Basis of Disease*, 1762(2):164–180.

Selivanov, V. A., Votyakova, T. V., Pivtoraiko, V. N., Zeak, J., Sukhomlin, T., Trucco, M., Roca, J., and Cascante, M. (2011). Reactive Oxygen Species Production by Forward and Reverse Electron Fluxes in the Mitochondrial Respiratory Chain. *PLoS Computational Biology*, 7(3):e1001115.

Selkoe, D. J. (2004). Cell biology of protein misfolding: The examples of Alzheimer's and Parkinson's diseases. *Nature Cell Biology*, 6(11):1054–1061.

Selkov, E. E. (1968). Self-Oscillations in Glycolysis. *European Journal of Biochemistry*, 4(1):79–86.

Selkov, E. E. (1975). Stabilization of Energy Charge, Generation of Oscillations and Multiple Steady States in Energy Metabolism as a Result of Purely Stoichiometric Regulation. *European Journal of Biochemistry*, 59(1):151–157.

Serrano-Pozo, A., Gómez-Isla, T., Growdon, J. H., Frosch, M. P., and Hyman, B. T. (2013). A Phenotypic Change But Not Proliferation Underlies Glial Responses in Alzheimer Disease. *The American Journal of Pathology*, 182(6):2332–2344.

Sertbaş, M., Ülgen, K., and Çakır, T. (2014). Systematic analysis of transcription-level effects of neurodegenerative diseases on human brain metabolism by a newly reconstructed brain-specific metabolic network. *FEBS Open Bio*, 4(1):542–553.

Sofroniew, M. V. and Vinters, H. V. (2010). Astrocytes: biology and pathology. *Acta Neuropathologica*, 119(1):7–35.

Stanford, N. J., Lubitz, T., Smallbone, K., Klipp, E., Mendes, P., and Liebermeister, W. (2013). Systematic Construction of Kinetic Models from Genome-Scale Metabolic Networks. *PLoS ONE*, 8(11):e79195.

Stincone, A., Prigione, A., Cramer, T., Wamelink, M. M. C., Campbell, K., Cheung, E., Olin-Sandoval, V., Grüning, N.-M., Krüger, A., Tauqeer Alam, M., Keller, M. A., Breitenbach, M., Brindle, K. M., Rabinowitz, J. D., and Ralser, M. (2015). The return of metabolism: biochemistry and physiology of the pentose phosphate pathway. *Biological Reviews*, 90(3):927–963.

Swerdlow, R. H., Burns, J. M., and Khan, S. M. (2014). The Alzheimer's disease mitochondrial cascade hypothesis: Progress and perspectives. *Biochimica et Biophysica Acta (BBA) - Molecular Basis of Disease*, 1842(8):1219–1231.

Tanzi, R. E. (2012). The genetics of Alzheimer Disease. *Cold Spring Harbor Perspectives in Medicine*, 2(10):a006296.

Tanzi, R. E., Moir, R. D., and Wagner, S. L. (2004). Clearance of Alzheimer's Abeta peptide: the many roads to perdition. *Neuron*, 43(5):605–608.

Tiveci, S., Akın, A., Çakır, T., Saybaşılı, H., and Ülgen, K. (2005). Modelling of calcium dynamics in brain energy metabolism and Alzheimer's disease. *Computational Biology and Chemistry*, 29(2):151–162.

Ulmer, S. and Jansen, O., editors (2010). *fMRI*. Springer Berlin Heidelberg, Berlin, Heidelberg.

Vafaee, M. S. and Gjedde, A. (2000). Model of BloodBrain Transfer of Oxygen Explains Nonlinear Flow-Metabolism Coupling During Stimulation of Visual Cortex. *Journal of Cerebral Blood Flow & Metabolism*, 20(4):747–754.

Vanzani, M. C., Iacono, R. F., Caccuri, R. L., and Berria, M. I. (2005). Immunochemical and morphometric features of astrocyte reactivity vs. plaque location in Alzheimer's disease. *MEDICINA-Buenos Aires*, 65(3):213.

Vaz, A. I. F. and Vicente, L. N. (2007). A particle swarm pattern search method for bound constrained global optimization. *Journal of Global Optimization*, 39(2):197–219.

Vijayan, V. K., Geddes, J. W., Anderson, K. J., Chang-Chui, H., Ellis, W. G., and Cotman, C. W. (1991). Astrocyte hypertrophy in the Alzheimer's disease hippocampal formation. *Experimental Neurology*, 112(1):72–78.

Voit, E. O., Martens, H. A., and Omholt, S. W. (2015). 150 Years of the Mass Action Law. *PLOS Comput Biol*, 11(1):e1004012.

Wallimann, T., Wyss, M., Brdiczka, D., Nicolay, K., and Eppenberger, H. M. (1992). Intracellular compartmentation, structure and function of creatine kinase isoenzymes in tissues with high and fluctuating energy demands: the 'phosphocreatine circuit' for cellular energy homeostasis. *Biochemical Journal*, 281(Pt 1):21–40.

Wamelink, M. M. C., Struys, E. A., and Jakobs, C. (2008). The biochemistry, metabolism and inherited defects of the pentose phosphate pathway: A review. *Journal of Inherited Metabolic Disease*, 31(6):703–717.

Wang, D.-S., Dickson, D. W., and Malter, J. S. (2006). beta-Amyloid Degradation and Alzheimer's Disease. *Journal of Biomedicine and Biotechnology*, 2006.

Wang, X., Wang, W., Li, L., Perry, G., Lee, H.-g., and Zhu, X. (2014). Oxidative stress and mitochondrial dysfunction in Alzheimer's disease. *Biochimica et Biophysica Acta (BBA) - Molecular Basis of Disease*, 1842(8):1240–1247.

Winter, F., Bludszuweit-Philipp, C., and Wolkenhauer, O. (2017). Mathematical analysis of the influence of brain metabolism on the BOLD signal in Alzheimer's disease. *Journal of Cerebral Blood Flow & Metabolism*, page 0271678X17693024.

Wittig, U., Kania, R., Golebiewski, M., Rey, M., Shi, L., Jong, L., Algaa, E., Weidemann, A., Sauer-Danzwith, H., Mir, S., Krebs, O., Bittkowski, M., Wetsch, E., Rojas, I., and Müller, W. (2012). SABIO-RK—database for biochemical reaction kinetics. *Nucleic Acids Research*, 40(D1):D790–D796.

Wolstencroft, K., Haines, R., Fellows, D., Williams, A., Withers, D., Owen, S., Soiland-Reyes, S., Dunlop, I., Nenadic, A., Fisher, P., Bhagat, J., Belhajjame, K., Bacall, F., Hardisty, A., Nieva de la Hidalga, A., Vargas, B., P, M., Sufi, S., and Goble, C. (2013). The Taverna workflow suite: designing and executing workflows of Web Services on the desktop, web or in the cloud. *Nucleic Acids Research*, 41(W1):W557–W561.

World Health Organization (1992). The ICD-10 classification of mental and behavioural disorders: clinical descriptions and diagnostic guidelines.

Zi, Z. (2011). Sensitivity analysis approaches applied to systems biology models. *IET Systems Biology*, 5:336–346.

Ziegler, U. and Doblhammer, G. (2009). Prävalenz und Inzidenz von Demenz in Deutschland - Eine Studie auf Basis von Daten der gesetzlichen Krankenversicherungen von 2002. *Gesundheitswesen*, 71(5):281–290.

Zlokovic, B. V. (2008). The Blood-Brain Barrier in Health and Chronic Neurodegenerative Disorders. *Neuron*, 57(2):178–201.

Appendix A.

Derivation of equation for capillary concentrations of glucose, oxygen and lactate in the model by Aubert et al. (2001)

Capillary glucose

The concentration of capillary glucose (GLC_c) is assumed to the equal to average of the arterial concentration (GLC_a) and the venous concentration (GLC_v):

$$GLC_c = \frac{GLC_a + GLC_v}{2} \tag{A.1}$$

The time derivative of capillary glucose depends on the cerebral blood flow (CBF), the capillary volume (V_c), the amount of glucose transported from the blood to the brain (v_{GLCm}) times the neuronal volume (V), and the concentrations introduced above:

$$\frac{\mathrm{d}GLC_c}{\mathrm{d}t} = \frac{CBF \cdot GLC_a}{V_c} - \frac{CBF \cdot GLC_v}{V_c} - \frac{V}{V_c} \cdot v_{GLCm}$$

Using Equation A.1 this can be rewritten as

$$\begin{aligned} \frac{\mathrm{d}GLC_c}{\mathrm{d}t} &= \frac{CBF}{V_c}\left(GLC_a - (2 \cdot GLC_c - GLC_a)\right) - \frac{V}{V_c} \cdot v_{GLCm} \\ \frac{\mathrm{d}GLC_c}{\mathrm{d}t} &= \frac{2 \cdot CBF}{V_c}\left(GLC_a - GLC_c\right) - \frac{V}{V_c} \cdot v_{GLCm} \end{aligned}$$

and after defining $r_c = V_c/V$ and $v_{GLC_c} = \frac{2 \cdot CBF}{V_c}\left(GLC_a - GLC_c\right)$, we get

$$\frac{\mathrm{d}GLC_c}{\mathrm{d}t} = v_{GLC_c} - \frac{1}{r_c} v_{GLCm}$$

Capillary lactate and oxygen

The same argument leads to

$$\begin{aligned} \frac{\mathrm{d}LAC_c}{\mathrm{d}t} &= v_{LAC_c} + \frac{1}{r_c} v_{LACm} \\ \frac{\mathrm{d}O2_c}{\mathrm{d}t} &= v_{O2_c} - \frac{1}{r_c} v_{O2m} \end{aligned}$$

Appendix B.

Conversion between two notations of the common modular rate law

For the special case of a reversible reaction with two reactants $A + B \Leftrightarrow 2C$ the common modular rate law is given in Liebermeister et al. (2010) as:

$$v = u \cdot \frac{k^+ \cdot \frac{a}{k_A^M} \cdot \frac{b}{k_B^M} - k^- \cdot (\frac{c}{k_C^M})^2}{(1 + \frac{a}{k_A^M})(1 + \frac{b}{k_B^M}) + (1 + \frac{c}{k_C^M})^2 - 1} \tag{B.1}$$

In (Stanford et al., 2013) the following notation is used:

$$v = V_m \frac{1}{k_A^M k_B^M} \frac{ab - \frac{c^2}{K_{eq}}}{(1 + \frac{a}{k_A^M})(1 + \frac{b}{k_B^M}) + (1 + \frac{c}{k_C^M})^2 - 1} \tag{B.2}$$

The first equation can be transformed into the second by the following steps:

$$\begin{aligned}
v &= u \cdot \frac{k^+ \cdot (\frac{a}{k_A^M} \frac{b}{k_B^M} - \frac{k^-}{k^+} \cdot (\frac{c}{k_C^M})^2)}{(1 + \frac{a}{k_A^M})(1 + \frac{b}{k_B^M}) + (1 + \frac{c}{k_C^M})^2 - 1} \\
&= k^+ u \cdot \frac{\frac{1}{k_A^M k_B^M}(ab - \frac{k^-}{k^+} \cdot \frac{k_A^M k_B^M}{(k_C^M)^2} c^2)}{(1 + \frac{a}{k_A^M})(1 + \frac{b}{k_B^M}) + (1 + \frac{c}{k_C^M})^2 - 1} \\
&= k^+ u \cdot \frac{1}{k_A^M k_B^M} \frac{ab - \frac{k^-}{k^+} \cdot \frac{k_A^M k_B^M}{(k_C^M)^2} c^2}{(1 + \frac{a}{k_A^M})(1 + \frac{b}{k_B^M}) + (1 + \frac{c}{k_C^M})^2 - 1} \\
&= V_m \frac{1}{k_A^M k_B^M} \frac{ab - \frac{c^2}{K_{eq}}}{(1 + \frac{a}{k_A^M})(1 + \frac{b}{k_B^M}) + (1 + \frac{c}{k_C^M})^2 - 1}
\end{aligned}$$

for $V_m = k^+ u$ and $K_{eq} = \frac{k^+}{k^-} \frac{k_A^M k_B^M}{(k_C^M)^2}$.

Appendix C.

Full set of equations for metabolic network model

Table C.1.: Metabolic reactions and parameter values for astrocytes.

Glycolysis and mitochondrial respiration		
Equation	Parameter	Value
Hexokinase		
$v^g_{\mathrm{HK}} = k_{\mathrm{HK}} \cdot \mathrm{ATP}^g \left(1 + \frac{\mathrm{G6P}^g}{K_{I,G6P}}\right)^{-1}$	k_{HK}	0.01
	$K_{I,\mathrm{GLC}}$	0.02
PGI		
$v^g_{\mathrm{PGI}} = k_1 \cdot \mathrm{G6P}^g - k_2 \cdot \mathrm{F6P}^g$	k_1	931.69
	k_2	2273.32
PFK		
$v^g_{\mathrm{PFK}} = k_{\mathrm{PFK}} \cdot \mathrm{ATP}^g \cdot \left(1 + \left(\frac{\mathrm{ATP}^g}{K_{I,\mathrm{ATP}}}\right)^{nH}\right)^{-1} \cdot \frac{\mathrm{F6P}^g}{\mathrm{F6P}^g + K_{m,\mathrm{F6P}}}$	k_{PFK}	0.2
	$K_{I,\mathrm{ATP}}$	1.0
	nH	4
	$K_{m,\mathrm{F6P}}$	0.18
PGK		
$v^g_{\mathrm{PGK}} = k_{\mathrm{PGK}} \cdot \mathrm{GAP}^g \cdot \mathrm{ADP}^g \cdot \frac{\mathrm{NAD}^g}{\mathrm{NADH}^g}$	k_{PGK}	3.0
PK		
$v^g_{\mathrm{PK}} = k_{\mathrm{PK}} \cdot \mathrm{PEP}^g \cdot \mathrm{ADP}^g$	k_{PK}	20
LDH		
$v^g_{LDH} = k_1 \cdot \mathrm{PYR}^g \cdot \mathrm{NADH}^g - k_2 \cdot \mathrm{LAC}^g \cdot \mathrm{NAD}^g$	k_1	780
	k_2	32
mitochondrial respiration		
$v^g_{\mathrm{Mito}} = V_{\max} \cdot \frac{\mathrm{PYR}^g}{\mathrm{PYR}^g + K_{m,\mathrm{PYR}}} \cdot \frac{\mathrm{ADP}^g}{\mathrm{ADP}^g + K_{m,\mathrm{ADP}}} \cdot \frac{{\mathrm{O_2}}^g}{{\mathrm{O_2}}^g + K_{m,\mathrm{O_2}}} \cdot \left(1 - \frac{1}{1 + e^{-5 \cdot \left(\frac{\mathrm{ATP}^g}{\mathrm{ADP}^g} - 20\right)}}\right)$	$V_{\max}$	0.01
	$K_{m,\mathrm{PYR}}$	0.0632
	$K_{m,\mathrm{ADP}}$	0.00107
	$K_{m,\mathrm{O_2}}$	0.0029658
Pentose-phosphate pathway		
R02736: ZWF		
$v^g_{ZWF} = V_{\max} \cdot \frac{1}{K_{\mathrm{G6P}} \cdot K_{\mathrm{NADP}}} \cdot \frac{\mathrm{G6P}^g \cdot \mathrm{NADP}^g - \frac{\mathrm{G6L}^g \cdot \mathrm{NADPH}^g}{K_{\mathrm{eq}}}}{\left(1 + \frac{\mathrm{G6P}^g}{K_{\mathrm{G6P}}}\right) \cdot \left(1 + \frac{\mathrm{NADP}^g}{K_{\mathrm{NADP}}}\right) + \left(1 + \frac{\mathrm{G6L}^g}{K_{\mathrm{G6L}}}\right) \cdot \left(1 + \frac{\mathrm{NADPH}^g}{K_{\mathrm{NADPH}}}\right) - 1}$	$V_{\max}$	0.29057
	K_{eq}	22906
	K_{G6P}	6.91392e-05
	K_{NADP}	1.31616e-05
	K_{G6L}	0.0180932
	K_{NADPH}	0.00050314
R02035: SOL		
$v^g_{SOL} = V_{\max} \cdot \frac{1}{K_{\mathrm{G6L}}} \cdot \frac{\mathrm{G6L}^g - \frac{\mathrm{P6G}^g}{K_{\mathrm{eq}}}}{\left(1 + \frac{\mathrm{G6L}^g}{K_{\mathrm{G6L}}}\right) + \left(1 + \frac{\mathrm{P6G}^g}{K_{\mathrm{P6G}}}\right) - 1}$	$V_{\max}$	0.184701

Table C.1.: continued

Equation	Parameter	Value
	K_{eq}	531174
	K_{G6L}	0.0180932
	K_{P6G}	2.28618
R01528: GND		
	$V_{\max}$	1.31377
$v^g_{GND} = V_{\max} \cdot \frac{1}{K_{\mathrm{P6G}} \cdot K_{\mathrm{NADP}}} \cdot \frac{\mathrm{P6G}^g \cdot \mathrm{NADP}^g - \frac{\mathrm{Ru5P}^g \cdot \mathrm{NADPH}^g}{K_{\mathrm{eq}}}}{\left(1+\frac{\mathrm{P6G}^g}{K_{\mathrm{P6G}}}\right)\cdot\left(1+\frac{\mathrm{NADP}^g}{K_{\mathrm{NADP}}}\right)+\left(1+\frac{\mathrm{Ru5P}^g}{K_{\mathrm{Ru5P}}}\right)\cdot\left(1+\frac{\mathrm{NADPH}^g}{K_{\mathrm{NADPH}}}\right)-1}$	K_{eq}	4.0852e+07
	K_{P6G}	3.23421e-05
	K_{NADP}	3.11043e-06
	K_{Ru5P}	0.0537179
	K_{NADPH}	0.00050314
R01056: RKI		
	$V_{\max}$	0.000821984
$v^g_{RKI} = V_{\max} \cdot \frac{1}{K_{\mathrm{Ru5P}}} \cdot \frac{\mathrm{Ru5P}^g - \frac{\mathrm{R5P}^g}{K_{\mathrm{eq}}}}{\left(1+\frac{\mathrm{Ru5P}^g}{K_{\mathrm{Ru5P}}}\right)+\left(1+\frac{\mathrm{R5P}^g}{K_{\mathrm{R5P}}}\right)-1}$	K_{eq}	0.0282061
	K_{Ru5P}	0.0537179
	K_{R5P}	0.778461
R01529: RPE		
	$V_{\max}$	0.00775925
$v^g_{RPE} = V_{\max} \cdot \frac{1}{K_{\mathrm{Ru5P}}} \cdot \frac{\mathrm{Ru5P}^g - \frac{\mathrm{X5P}^g}{K_{\mathrm{eq}}}}{\left(1+\frac{\mathrm{Ru5P}^g}{K_{\mathrm{Ru5P}}}\right)+\left(1+\frac{\mathrm{X5P}^g}{K_{\mathrm{X5P}}}\right)-1}$	K_{eq}	39.2574
	K_{Ru5P}	0.0537179
	K_{X5P}	0.603002
R5P sink		
$v^g_{R5P} = k \cdot \mathrm{R5P}^g$	k	0
R01641: TKL-1		
	$V_{\max}$	0.000244278
$v^g_{TKL-1} = V_{\max} \cdot \frac{1}{K_{\mathrm{X5P}} \cdot K_{\mathrm{R5P}}} \cdot \frac{\mathrm{X5P}^g \cdot \mathrm{R5P}^g - \frac{\mathrm{GAP}^g \cdot \mathrm{S7P}^g}{K_{\mathrm{eq}}}}{\left(1+\frac{\mathrm{X5P}^g}{K_{\mathrm{X5P}}}\right)\cdot\left(1+\frac{\mathrm{R5P}^g}{K_{\mathrm{R5P}}}\right)+\left(1+\frac{\mathrm{GAP}^g}{K_{\mathrm{GAP}}}\right)\cdot\left(1+\frac{\mathrm{S7P}^g}{K_{\mathrm{S7P}}}\right)-1}$	K_{eq}	1.65287e+06
	K_{X5P}	0.000173625
	K_{R5P}	0.000585387
	K_{GAP}	0.168333
	K_{S7P}	0.192807
R01830: TKL-2		
	$V_{\max}$	0.000137124
$v^g_{TKL-2} = V_{\max} \cdot \frac{1}{K_{\mathrm{F6P}} \cdot K_{\mathrm{GAP}}} \cdot \frac{\mathrm{F6P}^g \cdot \mathrm{GAP}^g - \frac{\mathrm{X5P}^g \cdot \mathrm{E4P}^g}{K_{\mathrm{eq}}}}{\left(1+\frac{\mathrm{F6P}^g}{K_{\mathrm{F6P}}}\right)\cdot\left(1+\frac{\mathrm{GAP}^g}{K_{\mathrm{GAP}}}\right)+\left(1+\frac{\mathrm{X5P}^g}{K_{\mathrm{X5P}}}\right)\cdot\left(1+\frac{\mathrm{E4P}^g}{K_{\mathrm{E4P}}}\right)-1}$	K_{eq}	0.0777764
	K_{F6P}	0.0799745
	K_{GAP}	0.168333
	K_{X5P}	0.603002
	K_{E4P}	0.109681
R01827: TAL		
	$V_{\max}$	0.0080394
$v^g_{TAL} = V_{\max} \cdot \frac{1}{K_{\mathrm{GAP}} \cdot K_{\mathrm{S7P}}} \cdot \frac{\mathrm{GAP}^g \cdot \mathrm{S7P}^g - \frac{\mathrm{F6P}^g \cdot \mathrm{E4P}^g}{K_{\mathrm{eq}}}}{\left(1+\frac{\mathrm{GAP}^g}{K_{\mathrm{GAP}}}\right)\cdot\left(1+\frac{\mathrm{S7P}^g}{K_{\mathrm{S7P}}}\right)+\left(1+\frac{\mathrm{F6P}^g}{K_{\mathrm{F6P}}}\right)\cdot\left(1+\frac{\mathrm{E4P}^g}{K_{\mathrm{E4P}}}\right)-1}$	K_{eq}	0.323922
	K_{GAP}	0.168333
	K_{S7P}	0.192807
	K_{F6P}	0.0799745
	K_{E4P}	0.109681
Housekeeping reactions astrocytes		
AK		
$v^g_{AK} = k_1 \cdot ADP^g \cdot ADP^g - k_2 \cdot ATP^g \cdot AMP^g$	k_1	1000
	k_2	920
ATPase		
$v^g_{ATPase} = V_{\max,ATPase} \cdot \frac{\mathrm{ATP}}{\mathrm{ATP}+K_{m,\mathrm{ATP}}}$	$V_{\max,ATPase}$	0.035
	$K_{m,\mathrm{ATP}}$	0.001
Creatine kinase		

Table C.1.: continued

Equation	Parameter	Value
$v^g_{CK,f} = k_{CK,f} \cdot \mathrm{ADP}^g \cdot \mathrm{PCr}^g - k_{CK,r} \cdot \mathrm{ATP}^g \cdot \mathrm{Cr}^g$	$k_{CK,f}$	0.5
	$k_{CK,r}$	0.01
NADPH oxidase astrocytes		
$v^g_{NADPH} = k_1 \cdot \mathrm{NADPH}^g$	k_1	0.000209722

Table C.2.: Metabolic reactions and parameter values for neurons.

Equation	Parameter	Value
Glycolysis and mitochondrial respiration		
Hexokinase		
$v^n_{\mathrm{HK}} = k_{\mathrm{HK}} \cdot \mathrm{ATP}^n \left(1 + \frac{\mathrm{G6P}^n}{K_{I,G6P}}\right)^{-1}$	k_{HK}	0.022
	$K_{I,\mathrm{GLC}}$	0.02
PGI		
$v^g_{\mathrm{PGI}} = k_1 \cdot \mathrm{G6P}^n - k_2 \cdot \mathrm{F6P}^n$	k_1	931.69
	k_2	2273.32
PFK		
$v^n_{\mathrm{PFK}} = k_{\mathrm{PFK}} \cdot \mathrm{ATP}^n \cdot \left(1 + \left(\frac{\mathrm{ATP}^n}{K_{I,\mathrm{ATP}}}\right)^{nH}\right)^{-1} \cdot \frac{\mathrm{F6P}^n}{\mathrm{F6P}^n + K_{m,\mathrm{F6P}}}$	k_{PFK}	0.44
	$K_{I,\mathrm{ATP}}$	1.0
	nH	4
	$K_{m,\mathrm{F6P}}$	0.18
PGK		
$v^n_{\mathrm{PGK}} = k_{\mathrm{PGK}} \cdot \mathrm{GAP}^n \cdot \mathrm{ADP}^n \cdot \frac{\mathrm{NAD}^n}{\mathrm{NADH}^n}$	k_{PGK}	10
PK		
$v^n_{\mathrm{PK}} = k_{\mathrm{PK}} \cdot \mathrm{PEP}^n \cdot \mathrm{ADP}^n$	k_{PK}	44
LDH		
$v^n_{LDH} = k_1 \cdot \mathrm{PYR}^n \cdot \mathrm{NADH}^n - k_2 \cdot \mathrm{LAC}^n \cdot \mathrm{NAD}^n$	k_1	2000
	k_2	15
mitochondrial respiration		
$v^n_{MITO} = V_{\max} \cdot \frac{\mathrm{PYR}^n}{\mathrm{PYR}^n + K_{m,\mathrm{PYR}}} \cdot \frac{\mathrm{ADP}^n}{\mathrm{ADP}^n + K_{m,\mathrm{ADP}}} \cdot \frac{{\mathrm{O_2}}^n}{{\mathrm{O_2}}^n + K_{m,\mathrm{O_2}}}$	$V_{\max}$	0.1
$\cdot \left(1 - \frac{1}{1 + e^{-5 \cdot \left(\frac{\mathrm{ATP}^n}{\mathrm{ADP}^n} - 20\right)}}\right)$	$K_{m,\mathrm{PYR}}$	0.0632
	$K_{m,\mathrm{ADP}}$	0.00107
	$K_{m,\mathrm{O_2}}$	0.0029658
Pentose-phosphate pathway		
ZWF		
$v^n_{ZWF} = V_{\max} \cdot \frac{1}{K_{\mathrm{G6P}} \cdot K_{\mathrm{NADP}}} \cdot \frac{\mathrm{G6P}^n \cdot \mathrm{NADP}^n - \frac{\mathrm{G6L}^n \cdot \mathrm{NADPH}^n}{K_{\mathrm{eq}}}}{\left(1 + \frac{\mathrm{G6P}^n}{K_{\mathrm{G6P}}}\right) \cdot \left(1 + \frac{\mathrm{NADP}^n}{K_{\mathrm{NADP}}}\right) + \left(1 + \frac{\mathrm{G6L}^n}{K_{\mathrm{G6L}}}\right) \cdot \left(1 + \frac{\mathrm{NADPH}^n}{K_{\mathrm{NADPH}}}\right) - 1}$	$V_{\max}$	0.586458
	K_{eq}	22906
	K_{G6P}	6.91392e-05
	K_{NADP}	1.31616e-05
	K_{G6L}	0.0180932
	K_{NADPH}	0.00050314
SOL		
$v^n_{SOL} = V_{\max} \cdot \frac{1}{K_{\mathrm{G6L}}} \cdot \frac{\mathrm{G6L}^n - \frac{\mathrm{P6G}^n}{K_{\mathrm{eq}}}}{\left(1 + \frac{\mathrm{G6L}^n}{K_{\mathrm{G6L}}}\right) + \left(1 + \frac{\mathrm{P6G}^n}{K_{\mathrm{P6G}}}\right) - 1}$	$V_{\max}$	0.373782
	K_{eq}	531174
	K_{G6L}	0.0180932
	K_{P6G}	2.28618
GND		
$v^n_{GND} = V_{\max} \cdot \frac{1}{K_{\mathrm{P6G}} \cdot K_{\mathrm{NADP}}} \cdot \frac{\mathrm{P6G}^n \cdot \mathrm{NADP}^n - \frac{\mathrm{Ru5P}^n \cdot \mathrm{NADPH}^n}{K_{\mathrm{eq}}}}{\left(1 + \frac{\mathrm{P6G}^n}{K_{\mathrm{P6G}}}\right) \cdot \left(1 + \frac{\mathrm{NADP}^n}{K_{\mathrm{NADP}}}\right) + \left(1 + \frac{\mathrm{Ru5P}^n}{K_{\mathrm{Ru5P}}}\right) \cdot \left(1 + \frac{\mathrm{NADPH}^n}{K_{\mathrm{NADPH}}}\right) - 1}$	$V_{\max}$	2.6574
	K_{eq}	4.0852e+07
	K_{P6G}	3.23421e-05

Table C.2.: continued

Equation	Parameter	Value
	K_{NADP}	3.11043e-06
	K_{Ru5P}	0.0537179
	K_{NADPH}	0.00050314
RKI		
$v^n_{RKI} = V_{\max} \cdot \frac{1}{K_{\mathrm{Ru5P}}} \cdot \frac{\mathrm{Ru5P}^n - \frac{\mathrm{R5P}^n}{K_{\mathrm{eq}}}}{\left(1+\frac{\mathrm{Ru5P}^n}{K_{\mathrm{Ru5P}}}\right)+\left(1+\frac{\mathrm{R5P}^n}{K_{\mathrm{R5P}}}\right)-1}$	$V_{\max}$	0.00165901
	K_{eq}	0.0282061
	K_{Ru5P}	0.0537179
	K_{R5P}	0.778461
RPE		
$v^n_{RPE} = V_{\max} \cdot \frac{1}{K_{\mathrm{Ru5P}}} \cdot \frac{\mathrm{Ru5P}^n - \frac{\mathrm{X5P}^n}{K_{\mathrm{eq}}}}{\left(1+\frac{\mathrm{Ru5P}^n}{K_{\mathrm{Ru5P}}}\right)+\left(1+\frac{\mathrm{X5P}^n}{K_{\mathrm{X5P}}}\right)-1}$	$V_{\max}$	0.0156605
	K_{eq}	39.2574
	K_{Ru5P}	0.0537179
	K_{X5P}	0.603002
R5P sink		
$v^n_{R5P} = k \cdot \mathrm{R5P}^n$	k	0
TKL-1		
$v^n_{TKL-1} = V_{\max} \cdot \frac{1}{K_{\mathrm{X5P}} \cdot K_{\mathrm{R5P}}} \cdot \frac{\mathrm{X5P}^n \cdot \mathrm{R5P}^n - \frac{\mathrm{GAP}^n \cdot \mathrm{S7P}^n}{K_{\mathrm{eq}}}}{\left(1+\frac{\mathrm{X5P}^n}{K_{\mathrm{X5P}}}\right)\cdot\left(1+\frac{\mathrm{R5P}^n}{K_{\mathrm{R5P}}}\right)+\left(1+\frac{\mathrm{GAP}^n}{K_{\mathrm{GAP}}}\right)\cdot\left(1+\frac{\mathrm{S7P}^n}{K_{\mathrm{S7P}}}\right)-1}$	$V_{\max}$	0.000493027
	K_{eq}	1.65287e+06
	K_{X5P}	0.000173625
	K_{R5P}	0.000585387
	K_{GAP}	0.168333
	K_{S7P}	0.192807
TKL-2		
$v^n_{TKL-2} = V_{\max} \cdot \frac{1}{K_{\mathrm{F6P}} \cdot K_{\mathrm{GAP}}} \cdot \frac{\mathrm{F6P}^n \cdot \mathrm{GAP}^n - \frac{\mathrm{X5P}^n \cdot \mathrm{E4P}^n}{K_{\mathrm{eq}}}}{\left(1+\frac{\mathrm{F6P}^n}{K_{\mathrm{F6P}}}\right)\cdot\left(1+\frac{\mathrm{GAP}^n}{K_{\mathrm{GAP}}}\right)+\left(1+\frac{\mathrm{X5P}^n}{K_{\mathrm{X5P}}}\right)\cdot\left(1+\frac{\mathrm{E4P}^n}{K_{\mathrm{E4P}}}\right)-1}$	$V_{\max}$	0.000276758
	K_{eq}	0.0777764
	K_{F6P}	0.0799745
	K_{GAP}	0.168333
	K_{X5P}	0.603002
	K_{E4P}	0.109681
TAL		
$v^n_{TAL} = V_{\max} \cdot \frac{1}{K_{\mathrm{GAP}} \cdot K_{\mathrm{S7P}}} \cdot \frac{\mathrm{GAP}^n \cdot \mathrm{S7P}^n - \frac{\mathrm{F6P}^n \cdot \mathrm{E4P}^n}{K_{\mathrm{eq}}}}{\left(1+\frac{\mathrm{GAP}^n}{K_{\mathrm{GAP}}}\right)\cdot\left(1+\frac{\mathrm{S7P}^n}{K_{\mathrm{S7P}}}\right)+\left(1+\frac{\mathrm{F6P}^n}{K_{\mathrm{F6P}}}\right)\cdot\left(1+\frac{\mathrm{E4P}^n}{K_{\mathrm{E4P}}}\right)-1}$	$V_{\max}$	0.0162259
	K_{eq}	0.323922
	K_{GAP}	0.168333
	K_{S7P}	0.192807
	K_{F6P}	0.0799745
	K_{E4P}	0.109681
Housekeeping reactions neurons		
AK		
$v^n_{AK} = k_1 \cdot ADP^n \cdot ADP^n - k_2 \cdot ATP^n \cdot AMP^n$	k_1	1000
	k_2	920
ATPase		
$v^n_{ATPase} = V_{\max,ATPase} \cdot \frac{\mathrm{ATP}^n}{\mathrm{ATP}^n + K_{m,\mathrm{ATP}}}$	$V_{\max,ATPase}$	0.07
	$K_{m,\mathrm{ATP}}$	0.001
Creatine kinase		
$v^n_{CK,f} = k_{CK,f} \cdot \mathrm{ADP}^n \cdot \mathrm{PCr}^n - k_{CK,r} \cdot \mathrm{ATP}^n \cdot \mathrm{Cr}^n$	$k_{CK,f}$	0.5
	$k_{CK,r}$	0.01
NADPH oxidase astrocytes		
$v^n_{NADPH} = k_1 \cdot \mathrm{NADPH}^n$	k_1	0.00281384

Table C.3.: Exchange reactions used in the model. Superscripts indicate the location of the species (a = arteries, c = capillaries, e = extracellular space, g = astrocytes (glia cells), n = neurons).

Glucose and lactate exchange:		
$\mathrm{Glc}^a \leftrightarrow \mathrm{Glc}^c$	$\frac{2 \cdot F_{in}}{V_c} (\mathrm{Glc}^a - \mathrm{Glc}^c)$	
$\mathrm{Glc}^c \leftrightarrow \mathrm{Glc}^e$	$V_{max} \cdot \left(\frac{\mathrm{Glc}^c}{\mathrm{Glc}^c + K} - \frac{\mathrm{Glc}^e}{\mathrm{Glc}^e + K} \right)$	$V_{max} = 3.22$ $K = 9$
$\mathrm{Glc}^c \leftrightarrow \mathrm{Glc}^g$	$V_{max} \cdot \left(\frac{\mathrm{Glc}^c}{\mathrm{Glc}^c + K} - \frac{\mathrm{Glc}^g}{\mathrm{Glc}^g + K} \right)$	$V_{max} = 0.32$ $K = 9$
$\mathrm{Glc}^e \leftrightarrow \mathrm{Glc}^n$	$V_{max} \cdot \left(\frac{\mathrm{Glc}^e}{\mathrm{Glc}^e + K} - \frac{\mathrm{Glc}^n}{\mathrm{Glc}^n + K} \right)$	$V_{max} = 8826$ $K = 9$
$\mathrm{Glc}^e \leftrightarrow \mathrm{Glc}^g$	$V_{max} \cdot \left(\frac{\mathrm{Glc}^e}{\mathrm{Glc}^e + K} - \frac{\mathrm{Glc}^c}{\mathrm{Glc}^c + K} \right)$	$V_{max} = 956$ $K = 9$
$\mathrm{Lac}^c \leftrightarrow \mathrm{Lac}^a$	$\frac{2 \cdot F_{in}}{V_c} (\mathrm{Lac}^a - \mathrm{Lac}^c)$	
$\mathrm{Lac}^e \leftrightarrow \mathrm{Lac}^c$	$V_{max} \cdot \left(\frac{\mathrm{Lac}^e}{\mathrm{Lac}^e + K} - \frac{\mathrm{Lac}^c}{\mathrm{Lac}^c + K} \right)$	$V_{max} = 0.00587$ $K = 0.5$
$\mathrm{Lac}^g \leftrightarrow \mathrm{Lac}^c$	$V_{max} \cdot \left(\frac{\mathrm{Lac}^g}{\mathrm{Lac}^g + K} - \frac{\mathrm{Lac}^c}{\mathrm{Lac}^c + K} \right)$	$V_{max} = 0.00435$ $K = 0.5$
$\mathrm{Lac}^n \leftrightarrow \mathrm{Lac}^e$	$V_{max} \cdot \left(\frac{\mathrm{Lac}^n}{\mathrm{Lac}^n + K} - \frac{\mathrm{Lac}^e}{\mathrm{Lac}^e + K} \right)$	$V_{max} = 0.2175$ $K = 0.5$
$\mathrm{Lac}^g \leftrightarrow \mathrm{Lac}^e$	$V_{max} \cdot \left(\frac{\mathrm{Lac}^g}{\mathrm{Lac}^g + K} - \frac{\mathrm{Lac}^e}{\mathrm{Lac}^e + K} \right)$	$V_{max} = 0.057$ $K = 0.5$
Oxygen and carbon-dioxide exchange reactions:		
$\mathrm{O2}^a \leftrightarrow \mathrm{O2}^c$	$\frac{2 \cdot F_{in}}{V_c} (\mathrm{O2}^a - \mathrm{O2}^c)$	
$\mathrm{O2}^c \rightarrow \mathrm{O2}^g$	$\frac{PS_{cap}}{V_g} \cdot \left(K_{O2} \left(\frac{HbOP}{\mathrm{O2}^c} - 1 \right)^{\frac{-1}{nh}} - \mathrm{O2}^g \right)$	$PS_{cap} = 10.0$ $K_{O2} = 0.0361$ $HbOP = 8.6$ $nh = 2.73$
$\mathrm{O2}^c \rightarrow \mathrm{O2}^n$	$\frac{PS_{cap}}{V_n} \cdot \left(K_{O2} \left(\frac{HbOP}{\mathrm{O2}^c} - 1 \right)^{\frac{-1}{nh}} - \mathrm{O2}^n \right)$	$PS_{cap} = 40.5$ $K_{O2} = 0.0361$ $HbOP = 8.6$ $nh = 2.73$
$\mathrm{CO2}^c \leftrightarrow \mathrm{CO2}^a$	$\frac{2 \cdot F_{in}}{V_c} (\mathrm{CO2}^a - \mathrm{CO2}^c)$	
Neurotransmitter cycling:		
$\mathrm{GLU}^g \rightarrow \mathrm{GLU}^n$	$v_{GLU}^{gn} = V_{max} \cdot \frac{\mathrm{GLU}^g}{\mathrm{GLU}^g + K_{GLU}} \cdot \frac{\mathrm{ATP}^g}{\mathrm{ATP}^g + K_{ATP}}$	$V_{max} = 0.3$ $K_{GLU} = 0.05$ $K_{ATP} = 0.01532$
$\mathrm{GLU}^e \rightarrow \mathrm{GLU}^g$	$v_{GLU}^{eg} = V_{max} \frac{\mathrm{GLU}^e}{\mathrm{GLU}^e + K_{GLU}}$	$V_{max} = 0.026$ $K_{GLU} = 0.05$
$\mathrm{GLU}^n \rightarrow \mathrm{GLU}^e$	$v_{GLU}^{ne} = v_{stim} \cdot r_{Na,GLU} \cdot \frac{\mathrm{GLU}^n}{\mathrm{GLU}^n + K_{GLU}}$	$r_{Na,GLU} = 0.075$

$K_{GLU} = 0.05$

Table C.4.: Rate laws, algebraic equations and values at rest for species with a variable concentration in the model. Arterial concentration is fix for glucose (Glu^a) at 4.8 mmol/ml, carbon dioxide ($CO2^a$) at 1.2 mmol/ml, oxygen ($O2^a$) at 8.34 mmol/ml and lactate (LAC^a) at 0.313 mmol/ml.

Species	Value at rest	Equation	
		Astrocytes	
ATP	2.26	$\frac{\mathrm{dATP}^g}{\mathrm{dt}}$	$= -v^g_{HK} - v^g_{\mathrm{PFK}} + v^g_{\mathrm{PGK}} + v^g_{\mathrm{PK}} + 15 \cdot v^g_{\mathrm{Mito}} + v^g_{CK} - v^{gn}_{\mathrm{GLU}} - v^g_{pump} + v^g_{AK} - v^g_{ATPase}$
ADP	0.12	$\frac{\mathrm{dADP}^g}{\mathrm{dt}}$	$= v^g_{HK} + v^g_{\mathrm{PFK}} - v^g_{\mathrm{PGK}} - v^g_{\mathrm{PK}} - 15 \cdot v^g_{\mathrm{Mito}} - v^g_{CK} + v^{gn}_{\mathrm{GLU}} + v^g_{pump} - 2 \cdot v^g_{AK} + v^g_{ATPase}$
AMP	0.006	AMP^g	$= \mathrm{ANP}^g - \mathrm{ADP}^g - \mathrm{ATP}^g$ ($\mathrm{ANP}^g = 2.379$)
GLC	1.14	$\frac{\mathrm{dGLC}^g}{dt}$	$= v^{eg}_{\mathrm{GLC}} + v^{cg}_{\mathrm{GLC}} - v^g_{\mathrm{HK}}$
G6P	0.07	$\frac{\mathrm{dG6P}^g}{\mathrm{dt}}$	$= v^g_{\mathrm{HK}} - v^g_{\mathrm{PGI}} - v^g_{ZWF}$
F6P	0.0.046	$\frac{\mathrm{dF6P}^g}{\mathrm{dt}}$	$= v^g_{\mathrm{PGI}} - v^g_{\mathrm{PFK}} - v^g_{TKL-2} + v^g_{TAL}$
GAP	0.0.002	$\frac{\mathrm{dGAP}^g}{\mathrm{dt}}$	$= 2 \cdot v^g_{\mathrm{PFK}} - v^g_{PGK} + v^g_{TKL-1} - v^g_{TKL-2} - v^g_{TAL}$
G6L	2.9e-06	$\frac{\mathrm{dG6L}^g}{\mathrm{dt}}$	$= v^g_{ZWF} - v^g_{SOL}$
P6G	0.0018	$\frac{\mathrm{dP6G}^g}{\mathrm{dt}}$	$= v^g_{SOL} - v^g_{GND}$
Ru5P	0.0006	$\frac{\mathrm{dRu5P}^g}{\mathrm{dt}}$	$= v^g_{GND} - v^g_{RPE} - v^g_{RKI}$
R5P	2.6e-05	$\frac{\mathrm{dR5P}^g}{\mathrm{dt}}$	$= v^g_{RKI} - v^g_{TKL-1} - v^g_{R5P}$
X5P	0.02	$\frac{\mathrm{dX5P}^g}{\mathrm{dt}}$	$= v^g_{RPE} - v^g_{TKL-1} + v^g_{TKL-2}$
S7P	0.277	$\frac{\mathrm{dS7P}^g}{\mathrm{dt}}$	$= v^g_{TKL-1} - v^g_{TAL}$
E4P	0.0056	$\frac{\mathrm{dE4P}^g}{\mathrm{dt}}$	$= v^g_{TAL} + v^g_{TKL-2}$
PEP	0.03	$\frac{\mathrm{dPEP}^g}{\mathrm{dt}}$	$= v^g_{\mathrm{PGK}} - v^g_{\mathrm{PK}}$
PYR	0.16	$\frac{\mathrm{dPYR}^g}{\mathrm{dt}}$	$= v^g_{\mathrm{PK}} - v^g_{\mathrm{Mito}} - v^g_{LDH}$
LAC	1.36	$\frac{\mathrm{dLAC}^g}{\mathrm{dt}}$	$= v^g_{LDH} - v^{ge}_{LAC} - v^{gc}_{LAC}$
O2	0.04	$\frac{\mathrm{dO2}^g}{\mathrm{dt}}$	$= v^{cg}_{O2} - 3 \cdot v^g_{\mathrm{Mito}}$
Cr	4.6	$\frac{\mathrm{dCr}^g}{\mathrm{dt}}$	$= v^g_{CK}$
PCr	0.4	$\frac{\mathrm{dPCr}^g}{\mathrm{dt}}$	$= -v^g_{CK}$
NADH	0.057	$\frac{\mathrm{dNADH}^g}{\mathrm{dt}}$	$= v^g_{PGK} - v^g_{\mathrm{Mito}} - v^g_{LDH}$
NAD	0.163	$\frac{\mathrm{dNAD}^g}{\mathrm{dt}}$	$= - v^g_{PGK} + v^g_{\mathrm{Mito}} + v^g_{LDH}$
NADPH	0.29123	$\frac{\mathrm{dNADPH}^g}{\mathrm{dt}}$	$= v^g_{ZWF} + v^g_{GND} - v^g_{NADPH}$
NADP	1.5e-09	$\frac{\mathrm{dNADP}^g}{\mathrm{dt}}$	$= v^g_{NADPH} - v^g_{ZWF} - v^g_{GND}$
Na+	15.5	$\frac{\mathrm{dNa+}^g}{\mathrm{dt}}$	$= v^g_{Leak} + v^{eg}_{GLU} - 3 \cdot v^g_{pump}$
GLU	0	$\frac{\mathrm{dGLU}^g}{\mathrm{dt}}$	$= v^{eg}_{GLU} - v^{gn}_{GLU}$
		Neurons	
ATP	2.26	$\frac{\mathrm{dATP}^n}{\mathrm{dt}}$	$= -v^n_{HK} - v^n_{\mathrm{PFK}} + v^n_{PGK} + v^n_{\mathrm{PK}} + 15 \cdot v^n_{\mathrm{Mito}} + v^n_{CK} - v^{nn}_{\mathrm{GLU}} - v^n_{pump} + v^n_{AK} - v^n_{ATPase}$
ADP	0.12	$\frac{\mathrm{dADP}^n}{\mathrm{dt}}$	$= v^n_{HK} + v^n_{\mathrm{PFK}} - v^n_{PGK} - v^n_{\mathrm{PK}} - 15 \cdot v^n_{\mathrm{Mito}} - v^n_{CK} + v^{nn}_{\mathrm{GLU}} + v^n_{pump} - 2 \cdot v^n_{AK} + v^n_{ATPase}$
AMP	0.006	AMP^n	$= \mathrm{ANP}^n - \mathrm{ADP}^n - \mathrm{ATP}^n$ ($\mathrm{ANP}^n = 2.379$)
GLC	1.14	$\frac{\mathrm{dGLC}^n}{dt}$	$= v^{en}_{\mathrm{GLC}} + v^{cn}_{\mathrm{GLC}} - v^n_{\mathrm{HK}}$
G6P	0.11	$\frac{\mathrm{dG6P}^n}{\mathrm{dt}}$	$= v^n_{\mathrm{HK}} - v^n_{\mathrm{PGI}} - v^n_{ZWF}$

F6P	0.45	$\frac{\mathrm{dF6P}^n}{\mathrm{dt}}$	$= v^n_{\mathrm{PGI}} - v^n_{\mathrm{PFK}} - v^n_{TKL-2} + v^n_{TAL}$
GAP	0.001	$\frac{\mathrm{dGAP}^n}{\mathrm{dt}}$	$= 2 \cdot v^n_{\mathrm{PFK}} - v^n_{PGK} + v^n_{TKL-1} - v^n_{TKL-2} - v^n_{TAL}$
G6L	3.0e-06	$\frac{\mathrm{dG6L}^n}{\mathrm{dt}}$	$= v^n_{ZWF} - v^n_{SOL}$
P6G	0.0029	$\frac{\mathrm{dP6G}^n}{\mathrm{dt}}$	$= v^n_{SOL} - v^n_{GND}$
Ru5P	0.00067	$\frac{\mathrm{dRu5P}^n}{\mathrm{dt}}$	$= v^n_{GND} - v^n_{RPE} - v^n_{RKI}$
R5P	2.7e-05	$\frac{\mathrm{dR5P}^n}{\mathrm{dt}}$	$= v^n_{RKI} - v^n_{TKL-1} - v^n_{R5P}$
X5P	0.02	$\frac{\mathrm{dX5P}^n}{\mathrm{dt}}$	$= v^n_{RPE} - v^n_{TKL-1} + v^n_{TKL-2}$
S7P	0.2	$\frac{\mathrm{dS7P}^n}{\mathrm{dt}}$	$= v^n_{TKL-1} - v^n_{TAL}$
E4P	0.006	$\frac{\mathrm{dE4P}^n}{\mathrm{dt}}$	$= v^n_{TAL} + v^n_{TKL-2}$
PEP	0.003	$\frac{\mathrm{dPEP}^n}{\mathrm{dt}}$	$= v^n_{\mathrm{PGK}} - v^n_{\mathrm{PK}}$
PYR	0.13	$\frac{\mathrm{dPYR}^n}{\mathrm{dt}}$	$= v^n_{\mathrm{PK}} - v^n_{\mathrm{Mito}} - v^n_{LDH}$
LAC	1.36	$\frac{\mathrm{dLAC}^n}{\mathrm{dt}}$	$= v^n_{LDH} - v^{ne}_{LAC} - v^{nc}_{LAC}$
O2	0.03	$\frac{\mathrm{dO2}^n}{\mathrm{dt}}$	$= v^{cn}_{O2} - 3 \cdot v^n_{\mathrm{Mito}}$
Cr	3.5	$\frac{\mathrm{dCr}^n}{\mathrm{dt}}$	$= -v^n_{CK}$
PCr	1.5	$\frac{\mathrm{dPCr}^n}{\mathrm{dt}}$	$= v^n_{CK}$
NADH	0.016	$\frac{\mathrm{dNADH}^n}{\mathrm{dt}}$	$= v^n_{PGK} - v^n_{\mathrm{Mito}} - v^n_{LDH}$
NAD	0.204	$\frac{\mathrm{dNAD}^n}{\mathrm{dt}}$	$=$ - $v^n_{PGK} + v^n_{\mathrm{Mito}} + v^n_{LDH}$
NADPH	0.29123	$\frac{\mathrm{dNADPH}^n}{\mathrm{dt}}$	$= v^n_{ZWF} + v^n_{GND} - v^n_{NADPH}$
NADP	2.2e-09	$\frac{\mathrm{dNADP}^n}{\mathrm{dt}}$	$= v^n_{NADPH} - v^n_{ZWF} - v^n_{GND}$
Na+	15.53	$\frac{\mathrm{dNa+}^n}{\mathrm{dt}}$	$= v^n_{Leak} + v^{en}_{GLU} - 3 \cdot v^n_{pump}$
GLU	3	$\frac{\mathrm{dGLU}^n}{\mathrm{dt}}$	$= v^{en}_{GLU} - v^{nn}_{GLU}$
		extracellular space	
GLC	1.14	$\frac{\mathrm{dGLC}^e}{\mathrm{dt}}$	$= v^{ce}_{GLC} - v^{en}_{GLC} - v^{eg}_{GLC}$
LAC	1.3	$\frac{\mathrm{dLAC}^e}{\mathrm{dt}}$	$= v^{ge}_{LAC} - v^{ec}_{LAC} - v^{en}_{LAC}$
GLU	0	$\frac{\mathrm{dGLU}^e}{\mathrm{dt}}$	$= v^{ne}_{GLU} - v^{eg}_{GLU}$
Na+	150 (fixed)		
		capillaries	
GLC	4.6	$\frac{\mathrm{dGLC}^c}{\mathrm{dt}}$	$= v^{ac}_{GLC} - v^{ce}_{GLC} - v^{cg}_{GLC}$
O2	7.3	$\frac{\mathrm{dO2}^c}{\mathrm{dt}}$	$= v^{ac}_{O2} - v^{cn}_{O2} - v^{cg}_{O2}$
LAC	0.34	$\frac{\mathrm{dLAC}^c}{\mathrm{dt}}$	$= v^{gc}_{LAC} - v^{ca}_{LAC} + v^{ec}_{LAC}$
CO2	2.2	$\frac{\mathrm{dCO2}^c}{\mathrm{dt}}$	$= 3 \cdot v^n_{\mathrm{Mito}} + 3 \cdot v^g_{\mathrm{Mito}} - v^{ca}_{CO2}$
dHb	0.047	$\frac{\mathrm{dHb}^c}{\mathrm{dt}}$	$= v_{dHb,in} - v_{dHb,out}$

Appendix D.

Correction of rate law for facilitated diffusion in COPASI

The flux of a transport-mediated facilitated diffusion reaction can be assumed to be proportional to the fraction of occupied transporters multiplied with the maximal achievable flux v_{max}:

$$V = v_{max} \cdot \frac{[TL]}{[TL] + [T]}$$

where $[L]$ is the ligand concentration, $[T]$ is the concentration of the transporters to which L binds, and [TL] is the concentration of the transporter-ligand complex. Using the association constant $K_a = \frac{[TL]}{[T] \cdot [L]}$ we can rewrite this equation to:

$$\begin{aligned} v &= v_{max} \cdot \frac{K_a \cdot [T] \cdot [L]}{K_a \cdot [T] \cdot [L] + [T]} \\ v &= v_{max} \cdot \frac{K_a \cdot [L]}{K_a \cdot [L] + 1} \\ v &= v_{max} \cdot \frac{[L]}{[L] + K_d} \end{aligned}$$

with $K_d = \frac{[T] \cdot [L]}{[TL]}$. For the reversible transport between compartment C1 and compartment C2, the rate law can be written as

$$v = v_{max} \cdot \left(\frac{[L\{C1\}]}{[L\{C1\}] + K_d} - \frac{[L\{C2\}]}{[L\{C2\}] + K_d} \right)$$

Curly braces indicate the location of the species, i.e. $[L\{C1\}]$ is the concentration of the ligand in the compartment $C1$. This equation given above is used in the model Cloutier et al. (2009) to describe the reversible exchange of glucose and lactate beween the different compartments.

Using the rate law for the unidirectional case allows to derive the differential equation for the following simple system:

- Species A is produced in compartment C1 at a constant rate k_1 (measured in mmol/(l*s))
- A is then transported via facilitated diffusion from compartment C1 to compartment C2
- In compartment C2 the species A is degraded according to simple mass action kinetics.

The resulting differential equations are:

$$\begin{aligned}\frac{\mathrm{d}[A\{C1\}]}{\mathrm{d}t} &= k_1 - v_{max} \cdot \frac{[A\{C1\}]}{[A\{C1\}] + K_d} \\ \frac{\mathrm{d}[A\{C2\}]}{\mathrm{d}t} &= v_{max} \cdot \frac{[A\{C1\}]}{[A\{C1\}] + K_d} \cdot \frac{V(C1)}{V(C2)} - k_2 \cdot [A\{C2\}]\end{aligned}$$

with k_1 given in $mmol/(ml * s)$, v_{max} given in $mmol/s$, K_d given in $mmol/ml$ and k_2 given in $1/s$. The factor $V(C1)/V(C2)$ accounts for the ratio of the volumes of the different compartments. If $V(C1)$ is for example two times $V(C2)$, a decrease in the concentrations of $A\{C1\}$ by 1 due to the facilitated transport would lead to an increase in the concentration of $A\{C2\}$ by 2. For values of $v_{max} = 1, K_d = 0.1, k_1 = k_2 = 0.5$ and identical compartment sizes $V(C1) = V(C2)$ the resulting equilibrium concentration of $A_{eq}\{C1\}$ and $A_{eq}\{C2\}$ are 0.1 and 1, respectively.

Surprisingly, in COPASI this is only true for compartment sizes of $1ml$ for both C1 and C2. As the only influence of the compartment sizes is the fraction $V(C1)/V(C2)$, the steady state solution of the system given above should be identical for compartment sizes resulting in the same fraction. (E.g. for every ratio $V(C1)/V(C2) = x$, the steady state solution should be identical.)

To understand why this does not hold in COPASI it is necessary to have a look at the ODEs produced by COPASI for the simple system described above.

$$\begin{aligned}\frac{\mathrm{d}\left([\mathrm{A\{C1\}}] \cdot V_{\mathrm{C1}}\right)}{\mathrm{d}t} &= \overbrace{V_{\mathrm{C1}} \cdot k_1}^{production} - \overbrace{v_{max} \cdot \frac{[\mathrm{A\{C1\}}]}{[\mathrm{A\{C1\}}] + K_d}}^{transport} \\ \frac{\mathrm{d}\left([\mathrm{A\{C2\}}] \cdot V_{\mathrm{C2}}\right)}{\mathrm{d}t} &= \underbrace{v_{max} \cdot \frac{[\mathrm{A\{C1\}}]}{[\mathrm{A\{C1\}}] + K_d}}_{transport} - \underbrace{V_{\mathrm{C2}} \cdot \left(k_2 \cdot [\mathrm{A\{C2\}}]\right)}_{degradation}\end{aligned}$$

The main difference of this set of ODEs is that the left hand side of each equation does not describe a change in the concentration of A{C1} and A{C2}, but instead a change in the amount of the species, i.e. the concentration multiplied with the respective volume. However, this multiplication is not done consistently. In particular, for reactions which occur between two compartments, such as the facilitated diffusion (labelled transport above), no multiplication is done.

This leads to different results as soon as the volume of the compartments changes. If both are multiplied by a common factor while keeping the concentration constant, the left hand side of the equation as well as the production and degradation term will be changed according to the new amount of the species. The transport part of the ODE instead will not change, as the concentration itself has not been altered.

Using the parameter values given above, it is easy to calculate the steady-state values for this system of ODEs for different values of compartment sizes. For the simple case of $V\{C1\} = V\{C2\} = 1$, the solution is identical to the one calculated before ($A_{eq}\{C1\} = 0.1, A_{eq}\{C2\} = 1$). For $V\{C1\} = V\{C2\} = 2$ no steady-state solution exists.

The solution to this problem is to adjust the rate laws for transport reactions by hand, so that they are calculated with respect to the amount of species. In the example given above this can be done by changing the rate law for the facilitated diffusion to incorporate the information about the source volume:

$$v = v_{max} \cdot \frac{[L]}{[L] + K_d}$$

needs to be written as

$$v = v_{max} \cdot \frac{[L]}{[L] + K_d} \cdot V_{compartment}$$

which would result in the following equations being used by COPASI:

$$\frac{\mathrm{d}\left([\mathrm{A\{C1\}}] \cdot V_{\mathrm{C1}}\right)}{\mathrm{d}t} = \overbrace{V_{\mathrm{C1}} \cdot k_1}^{production} - \overbrace{v_{max} \cdot \frac{[\mathrm{A\{C1\}}]}{[\mathrm{A\{C1\}}] + K_d} \cdot V_{C1}}^{transport} \tag{D.1}$$

$$\frac{\mathrm{d}\left([\mathrm{A\{C2\}}] \cdot V_{\mathrm{C2}}\right)}{\mathrm{d}t} = \underbrace{v_{max} \cdot \frac{[\mathrm{A\{C1\}}]}{[\mathrm{A\{C1\}}] + K_d} \cdot V_{C1}}_{transport} - \underbrace{V_{\mathrm{C2}} \cdot \left(k_2 \cdot [\mathrm{A\{C2\}}]\right)}_{degradation} \tag{D.2}$$

While these equations still calculate the change with respect to the species amount, they correctly incorporate the influence of changes in the volume assuming constant concentrations.

If the goal is to recreate a model from literature which used ODEs for the concentrations instead of the particle numbers, particular caution is required. For the example ODE defined above,

$$\begin{aligned} \frac{\mathrm{d}[A\{C1\}]}{\mathrm{d}t} &= k_1 - \overbrace{v_{max} \cdot \frac{[A\{C1\}]}{[A\{C1\}] + K_d}}^{r_1} \\ \frac{\mathrm{d}[A\{C2\}]}{\mathrm{d}t} &= \underbrace{v_{max} \cdot \frac{[A\{C1\}]}{[A\{C1\}] + K_d} \cdot \frac{V(C1)}{V(C2)}}_{r_1^*} - k_2 \cdot [A\{C2\}] \end{aligned}$$

COPASI cannot create the required two different rate laws (i.e. the term for the source volume without the volume scaling (r_1) and the term for the sink volume with the volume fraction (r_1^*)). In the case that r_1 is expressed in terms of the source volume, a simple multiplication with the respective volumes will result in the rate laws used by COPASI:

$$\begin{aligned} \frac{\mathrm{d}[A\{C1\}] \cdot V_{\mathrm{C1}}}{\mathrm{d}t} &= V_{\mathrm{C1}} \cdot k_1 - \overbrace{v_{max} \cdot \frac{[A\{C1\}]}{[A\{C1\}] + K_d}}^{r_1} \cdot V_{\mathrm{C1}} \\ \frac{\mathrm{d}[A\{C2\}] \cdot V_{\mathrm{C2}}}{\mathrm{d}t} &= \underbrace{v_{max} \cdot \frac{[A\{C1\}]}{[A\{C1\}] + K_d}}_{r_1} \cdot V_{\mathrm{C1}} - k_2 \cdot [A\{C2\}] \cdot V_{\mathrm{C2}} \end{aligned}$$

In the case that r_1 is expressed in terms of the source volume, the following rate law is initially used:

$$\begin{aligned} \frac{\mathrm{d}[A\{C1\}]}{\mathrm{d}t} &= k_1 - \overbrace{v_{max} \cdot \frac{[A\{C1\}]}{[A\{C1\}] + K_d} \cdot \frac{V(C2)}{V(C1)}}^{r_1^*} \\ \frac{\mathrm{d}[A\{C2\}]}{\mathrm{d}t} &= \underbrace{v_{max} \cdot \frac{[A\{C1\}]}{[A\{C1\}] + K_d}}_{r_1} - k_2 \cdot [A\{C2\}] \end{aligned}$$

A simple multiplication of each reaction with the respective volume yields:

$$\frac{\mathrm{d}[A\{C1\}] \cdot V_{\mathrm{C1}}}{\mathrm{d}t} = k_1 \cdot V_{\mathrm{C1}} - \overbrace{v_{max} \cdot \frac{[A\{C1\}]}{[A\{C1\}] + K_d}}^{r_1} \cdot V_{\mathrm{C2}} \tag{D.3}$$

$$\frac{\mathrm{d}[A\{C2\}] \cdot V_{\mathrm{C2}}}{\mathrm{d}t} = \underbrace{v_{max} \cdot \frac{[A\{C1\}]}{[A\{C1\}] + K_d}}_{r_1} \cdot V_{\mathrm{C2}} - k_2 \cdot [A\{C2\}] \cdot V_{\mathrm{C2}} \tag{D.4}$$

The difference to the first case is that here r_1 is multiplied with the volume of the sink compartment (V_{C2}) instead of the volume of the source compartment (V_{C1}).

To keep the implementation in COPASI consistent, the rate laws used by COPASI expressed with respect to the sink compartment (Eqns. D.1,D.2) need to be multiplied with $\frac{V_{\mathrm{C2}}}{V_{\mathrm{C1}}}$. After this multiplication Equation D.1 is equivalent to Equation D.3 and Equation D.2 is equivalent to D.4.

The exchange reactions for which the rate law is given with respect to the sink compartment are

- GLC exchange capillary extracellular space $GLC^c \rightarrow GLC^e$ (v^{ce}_{GLC})
- GLC exchange extracellular space astrocytes $GLC^e \rightarrow GLC^g$ (v^{eg}_{GLC})
- GLC exchange extracelluar space neurons $GLC^e \rightarrow GLC^n$ (v^{en}_{GLC})
- GLC exchange capillary astrocytes $GLC^c \rightarrow GLC^g$ (v^{cg}_{GLC})
- O2 exchange capillary astrocytes $O_2^c \rightarrow O_2^g$ ($v^{cg}_{O_2}$)
- O2 exchange capillary neurons $O_2^c \rightarrow O_2^n$ ($v^{cn}_{O_2}$)

In addition, the transport of glutamate from the extracellular space to astrocytes which occurs after stimulation is also given with respect to its sink, i.e. to the astrocytic volume.

- GLU exchange extracellular space astrocytes $GLU^e \rightarrow GLU^g$ (v^{eg}_{GLU})

Theses

Part I

Aggregation of amyloid beta is a major hallmark of Alzheimer's disease. Its concentration in the brain is influenced by different members of the ABC transporter superfamily, especially ABCC1 and ABCB1.

1. The experimental data samples measured using an enzyme linked immuno sorbent assay (ELISA) is best described by assuming an underlying lognormal distribution.

2. The key assumptions to model amyloid beta aggregation *in vivo* are: (I) a mechanism consisting of initial nucleation and subsequent monomer addition, (II) removal of monomeric Aβ by ABC transporters, (III) no breakage of aggregates and (IV) the impediment of Aβ removal by larger aggregates.

3. The difference in the Aβ aggregation profiles between ABCC1$^{-/-}$ and ABCB1$^{-/-}$ mice can be explained by the higher transport capacity of ABCC1 compared to the transport capacity of ABCB1 alone.

Part II

Blood oxygen level-dependent functional magnetic resonance imaging (BOLD fMRI) is an important clinical imaging modality in Alzheimer's disease. The shape of the BOLD signal depends on the metabolic processes that underly the increased oxygen consumption following neuronal stimulation.

4. A mechanistic model of the metabolic pathways that links stimulation and oxygen consumption allows analysing the influence of changes in the enzyme expression and tissue composition observed in AD patients on the BOLD shape,

5. To adequately describe the brain energy metabolism in AD patients, a detailed description of the pentose phosphate pathway is necessary.

6. The three characteristics of the BOLD shape: peak height, peak time and full width at half maximum are sensitive to changes in the metabolic pathways of energy metabolism in the brain.

7. The new model developed in this work can be used to integrate knowledge about the influence of disease-specific alterations on BOLD fMRI into the clinical practice.